Mass transport deposits in deep-water minibasins: Outcropping examples from the minibasins adjacent to the Bakio salt wall (Basque Country, Northern Spain)

Y. Poprawski, C. Basile, Z. Cumberpatch, A. Eude

Mass transport deposits in deep-water minibasins : outcropping examples from the minibasins adjacent to the Bakio salt wall (Basque Country, Northern Spain).

Y.Poprawski[1,4], C. Basile[2], Z. Cumberpatch[3], A. Eude[4].

1: LPG-BIAF UMR-CNRS 6112, UNIV Angers, CNRS, UFR Sciences, 2 bd Lavoisier 49045, Angers CEDEX 01, France

2: Univ. Grenoble Alpes, Univ. Savoie Mont Blanc, CNRS, IRD, IFSTTAR, ISTerre, 38000 Grenoble, France

3: SedRESQ, Department of Earth and Environmental Sciences, University of Manchester, Oxford Road, Manchester M13 9PL, UK.

4: LPG UMR-CNRS 6112, UNIV Nantes, 2 rue de la Houssinière - BP 92208, 44322 Nantes Cedex 03 France.

Abstract

Recent subsurface studies show that mass-transport deposits (MTDs) in salt-controlled basins may correspond to local or regional bodies induced by either regional tectonics, or diapir growth. These MTDs are commonly considered as muddy bodies but they may alternatively incorporate a high amount of clasts and reworked beds with good reservoir properties and thus they are often challenging deposits in oil and gas exploration. The minibasins adjacent to the Bakio salt diapir, in northern Spain, provide a unique opportunity to study up to seven outcropping MTDs comparable in size to subsurface examples. Detailed structural analysis was used to reconstruct the transport direction for each MTD and to infer their source locations. In addition, facies analyses enabled the estimation of their percent of mud or matrix, allowing for a discussion on their potential reservoir and seal properties. At least six of the studied MTDs correspond to locally-derived MTDs sourced from the Bakio diapir or from the footwall of the adjacent sub-salt extensional faults. The primary trigger for these MTDs may be

halokinesis, probably with contributions from other secondary processes, such as carbonate platform aggradation, high sedimentation rates and regional extension. Transport directions together with palaeoflow analysis suggests that regionally-derived turbidites flowed along the minibasin axis, while MTDs were transported laterally from the minibasin margins at high angle with the turbidity flows. We identified three types of MTDs: muddy siliciclastic-dominated MTDs, sandstone clast-rich siliciclastic-dominated MTDs and carbonate-dominated MTDs. Using this classification and subsurface analogues we propose a model of locally-derived MTDs according to the nature of the source area and the sedimentary facies reworked along the MTD downslope trajectories. This model suggests that reservoir and seal properties could be suggested for MTDs in subsurface studies by characterizing the nature of the diapir roof and the facies at the seafloor found along the MTDs trajectories.

I Introduction

Mass-transport deposits (MTDs) are common gravity-induced units in deep-water environments triggered by slope failure, that include a range of facies from slides, slumps and debris flows (Ogata et al., 2014 ; Festa et al. 2016). MTDs linked with growing salt structures were previously documented by seismic surveys in: the Central Graben of the UK North Sea (Davison et al., 2000; Back et al., 2011; Arfai et al., 2016), the Gulf of Mexico (Tripsanas et al. 2004 ; Madof et al., 2009; Prather et al. 2012; Wu et al., 2020), Offshore Brazil (Gamboa et al., 2011; Jackson, 2012; Omosanya and Alves, 2013; Gamboa and Alves, 2016; Ward et al., 2018) and Offshore Angola (Gee and Gawthorpe, 2006; Doughty-Jones et al., 2019). Two type of MTDs are usually described

in salt-controlled basins: regionally-derived or extra-basinal MTDs and locally-derived or intrabasinal MTDs (e.g. Madoff et al., 2009; Doughty-Jones et al., 2019; Wu et al., 2020). Following the classification of Moscardelli and Wood (2008, 2016), regionally-derived MTDs, usually reach thousands of square kilometers in area and hundreds of meters in thickness, and are sourced from up-dip basin shelves or deltas. Failures of these up-dip locations, may be triggered by sea level variations, regional tectonics, or high sedimentation rates, causing the mass failure which results in the MTD (Moscardelli and Wood, 2016). Locally-derived MTDs correspond to more limited units, only reaching tens of square kilometers in area and are often sourced from margins of minibasins or localized bathymetric highs (Moscardelli and Wood, 2008, 2016). In salt controlled basins, these MTDs are assumed to be triggered by flank steepening during diapir growth (e.g. Madoff et al., 2009).

Facies variability in MTDs is a key uncertainty in subsurface studies for oil and gas exploration in deep-water settings, in part because MTDs can be good seals or good reservoirs dependent on primary lithology. For example, MTDs made of reworked chalk derived from the roof of diapirs in the Central Graben, UK North Sea, can form producing reservoirs (Davison et al., 2000; Arfai et al., 2016), while MTDs in a minibasin in the Mexico Gulf are assumed to have a high content of mud and thus to have preferential sealing properties (Madof et al., 2009). Subsurface data are useful for the characterization of the length and width of MTDs and of their lateral and vertical distribution inside minibasins. However, seismic datasets fails to assess the sub-seismic scale facies heterogeneity within the remobilized deposits. These elements may affect the sealing potential of MTDs. Therefore, integrating field-analogs and subsurface data

is vital for de-risking seal potential.

This study presents field-based structural and sedimentological analysis of seven MTDs exposed around the Bakio salt wall, which was growing during the Albian (Rowan et al., 2012; Ferrer et al., 2014; Poprawski et al., 2014, 2016; Roca et al. 2020), in the Basque-Cantabrian basin, northern Spain. The aims of this study are to assess the seal potential of MTDs in salt-controlled deep-water basins and to identify the genetic relationship between MTDs and coeval growing salt structures. These aims will be achieved by addressing the following objectives: (i) documenting the transport direction for each MTD exposed around Bakio, (ii) describing the nature of the clasts and folded beds, (iii) identifying their source areas and discussing their triggering mechanisms. The main findings of this study are then compared with other MTDs from salt-controlled basins worldwide.

II Geological setting

The Basque-Cantabrian basin (fig. 1) consists of an ENE-WSW trending aborted rift, developed along the Iberian and European plates boundary during the Mesozoic and inverted during the Cenozoic (e.g. Roca et al., 2011; Tugend et al., 2014; Pedrera et al., 2017; Ducoux et al. 2019). At present, this inverted basin belongs to the Pyrenean orogen and its inversion is related with the northward motion of the Iberian micro-plate toward the Eurasian plate (e.g. Vergés et al., 2002).

During the Late Triassic, a relatively thick succession of evaporites and red clays interbedded with dolerites were deposited (The Keuper Group), in depocenters associated with the aborted Permo-Triassic rift that developed in response to the break-up of Pangea (Ortí et al., 2017; McKie, 2017). The subsequent Jurassic to Berriasian

shallow-water epeiric carbonate platforms developed during a relative tectonic quiescence stage (Aurell et al., 2003 & 2010). During the Tithonian to Barremian, shallow-water siliciclastic units and carbonate platform deposits (Purbeck and Weald Complex equivalents) developed.

During the Aptian to Early-Middle Albian, strong subsidence (Gómez et al., 2002) preceding Albian extension caused the individualization of several depocenters, where carbonate platforms and marly lateral equivalent were deposited (Rat, 1988; García-Mondéjar et al., 1996; Martín-Chivelet et al., 2002). From the Albian to Cenomanian (Ducoux et al. 2019) extensional tectonics, salt withdrawal and diapir growth occurred (Pedrera et al., 2017; Roca et al., 2020). From the Middle Albian to Early Cenomanian, the individualization of the Basque Trough (Martín-Chivelet et al., 2002; García-Mondéjar et al., 2004) along the axis of the current Biscay Synclinorium and Anticlinorium (fig. 2), was coeval with the opening of the Bay of Biscay and the maximum subsidence in the Parentis basin (García-Mondéjar, 1996; Roca et al., 2011). During this stage, the increasing subsidence in the Basque Trough was associated with the deposition of Late Albian to Early Cenomanian siliciclastic deep-water deposits of the Black Flysch Group, which are locally up to 7000 m thick. These deep-water deposits were sourced from the Landes Massif basement block, presently located offshore (fig. 2) (Voort, 1963; Rat, 1988; Robles et al., 1988; García-Mondéjar et al., 1996; Agirrezabala, 1996; Martín-Chivelet et al., 2002; Puelles et al., 2014), that was uplifting during Cretaceous (Gómez et al., 2002). Pebbles from the coarse-grained facies of the Black Flysch Group commonly include metasandstones, foliated quartzites, recrystallized vein quartz and cherts derived from a Proterozoic and Palaeozoic source, likely the granitic

Landes Massif (Puelles et al., 2014). The culmination of extension is marked by the emplacement of alkaline volcanic rocks interbedded in the Black Flysch Group along the main faults of the Basque Trough (e.g. Montigny et al. 1986; Castañares et al., 2001; Ubide et al., 2014) and by Cretaceous high-temperature metamorphism (Cuevas and Tubía, 1999; Larrasoaña et al., 2003.b; Agirrezabala et al., 2014; Ducoux et al. 2019).

During the third stage of evolution, several diapirs in the Basque-Cantabrian basin grew in response to regional extension (e.g. Brinkmann and Lögters, 1967; Serrano and Martínez del Olmo, 1990; Cámara, 2017) (figs 1 and 2). One of these structures, the "Bakio diapir", is an elongated NE-SW trending salt wall (fig. 3), that was growing from the Neocomian or Aptian (Roca et al. 2020) to the Albian (Rowan et al., 2012; Ferrer et al., 2014; Poprawski et al., 2014; Roca et al., 2020). Field observations (Rowan et al., 2012; Ferrer et al., 2014; Poprawski et al., 2014), subsurface and high resolution bathymetric data (Roca et al., 2020) clearly document a strong thinning of the Albian units toward the diapir. Roca et al. (2020) proposed that the diapir started to grow within a relay zone between two roughly E-W trending basement faults, associated with sub-salt extensional faults: the Armintza and the Bermeo faults.

Slumps derived from the roof were described in diapir flanks (Poprawski et al., 2014) and the seafloor topography created by these slumps controlled deep-water system routing in the adjacent minibasins (Poprawski et al., 2014; Cumberpatch et al., 2021). An isolated carbonate platform was possibly growing on top of the salt wall, in the photic zone, while the adjacent basin remained in deeper settings (Poprawski et al., 2016; Roca et al., 2020) (fig. 3). The current offshore lateral extension of the carbonate platform above the salt, mapped using high resolution bathymetry (Bilbao-Lasa et al.,

2020; Roca et al., 2020) suggests that the salt body may be considered as an elongated salt wall rather than a rounded diapir.

During the post-rift stage, from the Late Cenomanian to Maastrichtian (e.g. Cámara, 2017; Pedrera et al., 2017) the Basque Trough remained under relatively deep-water conditions and was filled by calcareous deep-water deposits (Mathey 1987).

The onset of the Cenozoic shortening caused the inversion of the Basque-Cantabrian basin (fig. 2). Inversion possibly started from the Late Cretaceous (Campanian), and cumulated in the Eocene (Gómez et al., 2002; Payros et al., 2006; Pujalte et al., 2015). During inversion, the Landes Massif located in the northern foreland basin, subsided (fig. 2), as demonstrated by the thickness of Cenozoic sediments deposited top of this basement block (Ferrer et al., 2008). The study area including the Bakio diapir was transported northward on a decollement level in the Triassic salt (fig. 2) above the Landes Massif (Gómez et al., 2002; Ábalos, 2016; Pedrera et al. 2017; Cámara, 2017; Roca et al., 2020).

III Stratigraphy

The oldest rocks in the study area are the Triassic red clays and gypsum with embedded mafic rocks exposed in the Bakio salt wall (Poprawski et al., 2014) (fig. 3). Similar Triassic red clays and gypsum were found in the offshore Vizkaya B3 well (fig. 3) and in the Gernika – 1 well located outside of our study area, near Gernika (fig. 1), where the salt reaches up to 1480 m in thickness.

The overlying unit consists of shallow-water carbonate platform limestones (Castillo limestones Fm.) exposed northwest of the Gorliz town (figs. 3 and 4). This unit is composed of massive limestones with corals and rudists and is bound by an

upper erosive surface (S1, fig. 4) marked by karst cavities filled by sandstones of the overlying Monte Grande Fm. (Pujalte et al., 1987; Robles et al., 1988). The Monte Grande Fm. is about 360 m thick near Gorliz and is formed of a lower shallow-water siliciclastic interval (interpreted as a fan-delta by Robles et al., 1988) and an upper carbonate platform limestone (Pujalte et al., 1987; Robles et al., 1988) (fig. 4). Orbitolinids yielded a Lower Albian age for the limestones below and at the top of the Monte Grande Fm. (Pujalte et al., 1987; Robles et al., 1988) and thus it belongs to biostratigraphic sequence 1 of Agirrezabala and López-Horgue (2017). On the eastern flank of the Bakio salt wall, possible time-equivalent marls interbedded with thin-bedded packstones are exposed (figs 3 and 4) (the Bakio marls unit in Poprawski et al., 2014, 2016). This unit has a minimum thickness of 60 m, as its base is not exposed, and it is interpreted as deposited in an outer shelf setting (García-Mondéjar and Robador 1987; Robles et al., 1988) (fig. 4). This unit remains undated but the age of the overlying Bakio breccias Fm. suggests a Lower Albian age (fig. 4), however a younger age cannot be excluded.

The overlying Middle Albian to Lower Cenomanian succession corresponds to the Bakio breccias Fm., its equivalent the Bermeo breccias, and the overlying Black Flysch Group. The Bakio breccias Fm. is exposed around the Bakio salt wall (García-Mondéjar and Robador, 1987; Robles et al., 1988; Poprawski et al. 2016; Roca et al., 2020) (figs. 3 and 4). At the eastern flank of the Bakio salt wall, the Bakio breccias Fm. is 550 m thick (fig. 4) and unconformably overlies the Bakio marls (S2, fig. 4). It is composed of clast- and mud-supported breccias with limestone blocks, fine- and coarse-grained calcarenites and marls (García-Mondéjar and Robador, 1987; Robles

et al., 1988; Poprawski et al. 2016). The upper part of this unit onlaps a steep scarp exposed at Gaztelugatxe island (Poprawski et al., 2016) and developed in limestone breccias (Roca et al., 2020). The Bakio breccias Fm. were sourced from a carbonate platform that developed on the top of the Bakio salt wall (Poprawski et al., 2016) and exposed only at the Aketx island (fig. 3) and offshore (Roca et al., 2020). The carbonate platform was growing during the deposition of the Bakio breccias Fm., evidenced by individual unlithified fossils found in redeposited carbonates (Poprawski et al., 2016). On the western flank of the diapir, the Bakio breccias Fm. is dominated by matrix-supported breccias and marls. This unit at the western flank has a minimal thickness of 205 m, as its base is not exposed (fig. 4). These breccias thin toward the Bakio salt wall and show an upward decrease of their bedding dips and low-angle unconformities indicating that the growth of the diapir was coeval with deposition (Poprawski et al., 2014, 2016), in agreement with halokinetic sequence models (e.g. Giles and Rowan 2012). At Bermeo, matrix-supported breccias with limestone blocks interbedded with marls and fine- and coarse-grained calcarenites are interpreted as a lateral equivalent of the Bakio breccias Fm. (García-Mondéjar and Robador, 1987) (figs. 3 and 4). At present, the redeposited carbonates at Bermeo are dipping from 45° to 75° northward with relatively parallel bedding attitudes. These deposits have a minimal thickness of 100 m, although the thickness remains poorly constrained because the boundary with underlying marls is relatively progressive and because of poor-quality outcrops at the upper boundary. The Bakio breccias Fm. and its equivalent at Bermeo are interpreted as deposited on a carbonate slope and slope apron (Robles et al., 1988 ; Poprawski et al., 2016 ; Cumberpatch et al., 2021). According to orbitolinids reworked in breccias described by Robles et al. (1988), the

Bakio breccias Fm. and its lateral equivalent are probably Middle Albian in age.

The Black Flysch Group consist in deep-water siliciclastics deposits and its stratigraphy is relatively complex because of strong thickness and facies variations associated with relatively poorly constrained biostratigraphic data. The Black Flysch Group in the area can be divided into three different lithostratigraphic units: a lower coarse-grained siliciclastic unit (unit 1), a upper fine-grained unit (unit 2) and an uppermost sand-dominated unit (unit 3). In this paper, the previous local names used for example in Poprawski et al. (2014) have been abandoned (e.g. Punta de Bakio, Jata, Sollube, Matxitxako units) as these previous names are suggested to correspond to informal diachronic lithostratigraphic units following the recent biostratigraphic work of Agirrezabala and López-Horgue (2017).

Unit 1 (the Punta de Bakio and Jata units in Poprawski et al., 2014, 2016) is only exposed west of the diapir and is characterized by fine to coarse-grained siliciclastic turbidites, mud- and clast-supported conglomerates and breccias interbedded with shales (fig. 4). The first 60 m of this unit includes mixed sediments with a progressive decease of carbonate breccias interbedded with siliciclastic deposits. The depositional environments for this unit are interpreted to progress from channel, to channel-lobe transition zone to lobe sub-environments (Robles et al., 1988 ; Vicente-Bravo and Robles, 1991a; López-Horgue et al., 2009). Unit 2 is exposed on both flanks of the diapir and is characterized by thin-bedded, fine-sandstone-grained siliciclastic turbidites interbedded with shales and siderite beds (Robles et al., 1988; Vicente-Bravo and Robles, 1991b) (fig. 4). This unit is assumed to be deposited on the lower slope in a deep-water environments or on a marly prograding slope (Robles et

al., 1988 ; López-Horgue et al., 2009 ; Cumberpatch et al., 2021). East of the Bakio diapir, unit 2 (Sollube unit in Poprawski et al., 2014, 2016) is directly overlying the Bakio breccias Fm., while it is overlying the unit 1, west of the diapir. Unit 3 includes amalgamated, medium-bedded, coarse-grained siliciclastic turbidites, exposed at Matxitxako Cape (the Cabo Matxitxako unit in Poprawski et al., 2014, 2016) (fig. 3) and at Villano Cape. This unit is assumed to be deposited in channel to channel-lobe transition zone sub-environments (Robles et al., 1988). Although the sandy deposits exposed at Matxitxako Cape are relatively thin (about 100 m thick, fig. 4), the offshore map of Roca et al. (2020), based on high-resolution bathymetric data, suggests that unit 3 may have an significant northward offshore extension. The vertical succession which shows a fining upward sequence from unit 1 to unit 2 of the Black Flysch Group, is coeval with a global sea-level rise (De Graciansky et al., 1998; Haq, 2014). The abundance of mass-transport deposits in units 1 and at the base of unit 3 suggests a local halokinetic control (Poprawski et al., 2014, 2016; Cumberpatch et al., 2021). The coarse-grained facies in unit 3 suggests progradation driven by increases in sediment supply, linked with the uplift of the Landes Massif (García-Mondéjar et al. 1996; Martín-Chivelet et al. 2002; Puelles et al. 2014).

West of Bakio, the total thickness of the Black Flysch Group reaches up to 2000 m, while it is less than 200 m west of Armintza (fig. 4), where it is unconformably covering the Early Albian carbonate platform intervals (S2, fig. 4) (Agirrezabala, 2015; Agirrezabala et al., 2017). East of Bakio, the total thickness of the Black Flysch Group cannot be estimated as the roof has been eroded, but the absence of unit 1 suggests that the Black Flysch Group is relatively thinner compared to the western flank of the

diapir.

Biostratigraphic data gives some local constrains about the ages of the Black Flysch Group. The boundary between the Middle and Late Albian may be traced from Gorliz at about 200 m above the base of the Black Flysch Group (Agirrezabala, 2015) (stratigraphic section a, fig. 4), to Armintza just below the pillow lava and the MTD7 (López-Horgue et al., 2009) (stratigraphic section c, fig 4). In addition, the pillow lava and the MTD7 from Armintza (stratigraphic section c, fig. 4) can be traced west of Bakio (stratigraphic section d, fig. 4) following the bed traces on the high-resolution bathymetric data of Roca et al. (2020) (fig. 3). This suggests that the Middle Albian-Late Albian boundary lies within unit 1 west of Bakio, previously dated as a Late Albian unit (Jata unit in Poprawski et al., 2014). Orbitolinids found 45 m above the underlying Bermeo breccias give an Late Albian age for unit 2 (García-Mondéjar and Robador, 1987; Robles et al., 1988). This suggests that the Middle Albian-Late Albian boundary can be extended east of Bakio, at 45 m above the base of unit 2. Following these biostratigraphic data, the first 300 m of unit 1 (the Punta de Bakio and Jata units) belongs to the Middle Albian, while its upper part corresponds to the Late Albian. The Bakio breccias Fm. and the first 300 m of unit 1 may correspond with sequence 2 of Agirrezabala and López-Horgue (2017). The upper part of unit 1 and unit 2 may belong to sequence 3, and unit 3 possibly corresponds to sequence 4 of Agirrezabala and López-Horgue (2017). Although, the sandy amalgamated facies of the Matxitxako and Villano Cape could be grouped within the same unit (unit 3) based on similar facies and on their stratigraphic location above unit 2. Biostratigraphic arguments are lacking to decipher whether these facies are time-equivalent or not. Consequently, their

inferred Late Albian-Early Cenomanian age should be treated with caution.

The youngest unit in the study area, to the west of the Bakio salt wall is the Middle Cenomanian to Santonian Calcareous Flysch (Mathey, 1987; Castañares et al., 2001) (figs. 3 and 4). It is composed of thin-bedded fine-grained calcarenites interbedded with marls. In the westernmost part of our study area, the Calcareous Flysch unconformably overlies the Black Flysch Group units (S3, fig. 4) (Agirrezabala et al., 2017).

IV MTDs distribution within stratigraphy

Although the Black Flysch Group is dominated by shales, marls and wide range of turbiditic facies, it displays several slides, slumps and debrites, described in Robles et al. (1988, 1989), Poprawski et al. (2014, 2016) and Cumberpatch et al. (2021). These MTDs are concentrated in the lower part of the Black Flysch Group (fig. 4) and represent only a limited portion of the total thickness of the Black Flysch Group. For example, MTDs account for 31% of the total thickness of the measured sections in unit 1 in Cumberpatch et al. (2021) and for 22% in unit 2. The MTDs thickness usually ranges from to 50 cm to 10 m (Robles et al., 1988, 1989). In this paper, the thickest MTD is estimated to reach up to 20 m in thickness but its upper boundary is not clear and it may correspond to multiple stacked MTDs.

In unit 1, Robles et al. (1989) described up to six major MTDs with thickness exceeding 1 m and five other thinner MTDs. These MTDs are described as complete or incomplete successions including a basal debrite (thickness ranging from 0,5 to 7 m) or a basal slumpled interval (thickness ranging from 0,5 to 15 m) overlain by mega-

turbidites beds (thicknesses ranging from 2 to 10 m). Debrites are usually mud-rich and contain quartz pebbles and diagenetic siderite (Robles et al., 1989). These successions are interpreted to be the result of mass-failure followed by turbidity currents triggered by the same tectonic events (Robles et al., 1989). In unit 3 and 4, Cumberpatch et al. (2021) described several MTDs with thickness ranging from 0,5 to 3 m representing up to 22% of the total thickness of the measured stratigraphic-sections. These MTDs are described as poorly sorted deposits with mud-rich or sand-rich matrix containing sandstones rafts, siderite nodules, limestones clasts or mud-clast. In Cumberpatch et al. (2021) these MTDs are interpreted to correspond to mass-failure related to slope steepening on the flanks of the Bakio diapir.

In this study, only seven MTDs have been studied (fig. 4) among the large number of examples described in Robles et al. (1989) and Cumberpatch et al. (2021). Since the current work focuses on slope reconstructions using detailed measurements of slump folds axes and axial planes on the outcrop (see method section), MTDs which only contain debrite facies cannot be studied, because they lack structures to take measurements off. In addition, some of the MTDs described by previous authors in the study area, are exposed along steep coastal cliffs and their outcrops are usually hard to access. Thus all the MTDs that do not allow statistically relevant structural measurements have been also excluded.

The thicknesses of the studied MTDs range from 2 to 20 m suggesting that they correspond to major MTDs of the area and thus that they may be considered as representative of the local slope directions. The MTDs are exposed along tens of meter long outcrops and are usually cut along strike making it difficult to observe their

along slope lateral variations, that therefore remain interpretative.

V Methods

a. Palaeoflow and slumping sense reconstruction

We reconstructed palaeoflow orientations using sole marks and scours orientations from the basal surface of turbidites in the Black Flysch Group. Up to 89 sole marks and scours were measured on the field. Sole marks often give palaeoflow directions but palaeoflow sense often remains ambiguous. In this case, turbidity flows were assumed to come from local and regional palaeohighs; the Bakio salt wall (e.g. Poprawski et al., 2014) and the Landes Massif (Puelles et al., 2014) respectively. Up to 117 additional published palaeoflow measurements in the area East of the Matxitxako Cape (Cumberpatch et al., 2021) and up to 37 in the western part of the study area (Robles et al., 1989; Agirrezabala, 2015) were also used (fig. 3). Sole marks and scour surfaces are restored by rotating the host bed to a horizontal attitude as turbidites are commonly deposit on low-angle slopes (<1°) (e.g. Mulder and Cochonat, 1996).

We used a combination of methods to reconstruct the slumping direction and sense for each MTD. Up to four methods were used, dependent on the deformation style and measurements of orientation of folds axes and axial planes (fig. 5a, b). When possible, two other additional method based on faults orientations were also carried out. In all cases, the various results obtained are compared and discussed in order to find the most reliable slope direction.

The three methods described in this paragraph only provide robust results for simple cylindrical slump folds dominated by layer parallel shear (fig. 5a), that are roughly

normal to the downslope direction (Alsop and Holdsworth, 2007; Alsop and Marco, 2012; Sharman et al., 2015). The mean axis method (MAM) originally used by Jones (1939) is based on the assumption that the transport direction is perpendicular to the mean fold axis (fig. 5a) and the transport sense is given by the asymmetric structures found in the field (e.g. Alsop and Holdsworth, 2007). The mean axial plane strike method (MAPS) relies on the hypothesis that the transport direction corresponds to a horizontal line normal to the strike of the mean axial plane (fig. 5a) and the transport sense is given by the vergence of the folds, that verge upslope (e.g. Alsop and Marco, 2012). The mean fault orientation method (MFOM) presumes that transport direction is parallel to the dip of the mean fault trend and that reverse faults dip upslope and normal faults downslope (Farrell, 1984; Martinsen and Bakken, 1990; Debacker et al., 2009) (fig. 5a).

Alternatively, the three other methods described in this paragraph only provide robust results for sheath slump folds dominated by layer normal shear (fig. 5b). The downslope average axis method (DAM) is based on the assumption that the mean fold axis may have been reoriented, parallel to the transport direction (fig. 5b) in sheath slump folds (Woodcock, 1979b). The axial intersection method (AIM) presumes that axial planes radiate and dip in the downslope direction and thus the flow direction is inferred to be parallel with the strike of the radiating axial planes (fig. 5b) in slumps dominated by layer normal shear (e.g. Strachan and Alsop, 2006; Alsop and Holdsworth, 2007). The transport direction is calculated using the great circle including the poles of the radiating axial planes. In slumps dominated by layer normal shear, the transport direction is assumed to be perpendicular to the strike of the great circle of the radiating axial planes (fig. 5b). The best-fit girdle to fault plane method (GFPM) is based on the

analysis of the faults orientations, similarly to the MFOM but taking into account faults rotation and faults formed at low angle with the transport direction in layer normal shear (Debacker et al., 2009; Sharman et al., 2015). With this method, the transport direction is inferred to be parallel to the strike of the radiating faults (fig. 5b). It can be calculated, using the great circle by including the poles of the radial faults. In layer normal shear, the transport direction corresponds to the horizontal line normal to the strike of the great circle of the radial faults and the transport sense is given by the dip direction of the great circle.

Slumped horizons are also restored to a horizontal attitude, as recent studies also demonstrated that slumps may develop on low-angle slopes in sub-aqueous conditions (<1°) (e.g. García-Tortosa et al., 2011 ; Alsop and Marco, 2012; 2013). However, an error of few degrees in the dip of the initial slope may reverse the inferred slumping sense for recumbent folds in axial planes with a low-angle relative to bedding. When this is the case, it is noted and discussed herein.

b. Estimation of the percent of matrix in MTDs

To estimate the percent of mud or matrix in MTDs, we used a simple 2D methodology. Polygons for clasts and reworked beds and for matrix were drawn over field photographs using a vectorial drawing software (fig. 5c, d). Percentage of matrix versus clasts and reworked beds were calculated for each MTD using the number of pixels representing the matrix and the clasts and reworked beds. Even though MTDs are highly anisotropic in 3D, this method gives a simple estimation of the amount of matrix versus clasts and reworked beds in 2D and is a suitable method for the

comparison of MTDs in the study area. Where individual clasts are under the resolution of the image, the percentage of matrix may be overestimated.

VI. Mass-transport deposits description

Below we describe each MTD in detail, focusing on its location, stratigraphic position, thickness, internal facies and on the facies of its hosting succession before analyzing its direction of movement, using the methods described above. Using the direction of movement we infer the source (the active area where the evacuation was located and where mass-failure started) in alignment with Moscardelli and Wood (2008, 2016). The run-out distance, that corresponds to transport distance for each particle within a MTD, (Moscardelli and Wood, 2008, 2016) is qualitatively approached by comparing the reworked facies within MTDs with the in situ facies from the hosting succession.

a. The Bermeo MTD (MTD1)

The Bermeo MTD (fig. 6) is exposed north of the Bermeo town, in the Aritxatxu beach (figs. 3 and 4). It is located in a marly succession interbedded with mud- and clast-supported breccias with limestone blocks of the Bermeo breccias, interpreted to be deposited on a carbonate slope or slope apron (Robles et al., 1988). The hosting succession shows evidence of repeated mass failure that possibly result in stacked deposits, thus it is difficult at the outcrop to place the vertical boundaries of the MTD1. However, there is a clear 20 m thick interval, considered as MTD1, where syn-sedimentary deformation is concentrated. This MTD includes slide beds of matrix- and

clast-supported breccias with limestones blocks (up to 2 m in diameter), and thrust-imbricated calcarenites (fig. 6a, b, c). Beds inside the deformed horizons remain apparently parallel, because of the relatively low angle between bedding and imbricate thrusts (fig. 6a). MTD1 comprises up to 75% of matrix. Some scattered, refolded conical recumbent and rootless folds (fig. 6e) are found within muddy debrite intervals. This MTD can be interpreted as resulting from a series of carbonate debrites alternating with marl deposition followed by sliding of the previous succession. Since different deformed intervals with relatively diffuse boundaries are found within the MTD1, it is difficult to decipher whether this MTD results from one single event or of multiple stacked events.

After restoration to horizontal, the folds axes show a strong spatial dispersion and the mean axis is plunging toward the northeast (30°/18°NE) (fig. 6f). The mean axial plane is striking WNW-ESE and dipping northward (112°/20°N) (fig. 6f). Most of the syn-sedimentary thrusts (13 planes among 16) are striking E-W and dipping northward (fig. 6g). The MAM and MAPS suggest two inconsistent transport directions, as they indicate an ESE-directed (toward 120°) and SSW-directed transport (toward 202°), respectively (fig. 6f). In addition, the syn-sedimentary thrusts orientation suggests another S-directed transport direction (toward 173°) using the MFOM (fig. 6g). This demonstrates that folds in MTD1 are not cylindrical and instead formed in layer parallel shear, as suggested by the refolded conical recumbent rootless folds (fig. 6e). Therefore, methods for MTDs dominated by layer normal shear should be used preferentially. The DAM, AIM and GFPM provide similar and consistent results with an NNE-directed transport (toward 30°, 24° and 31°, respectively) (fig. 6f, g). All these elements suggest that the MTD1 formed in layer normal shear conditions and that it was transported toward the NNE. Even if this

MTD may result of multiple stacked events the similar results of the DAM, AIM and GFPM suggests that the slope direction remained the same for all the possible events.

The NNE-directed MTD1 (fig. 6) includes redeposited carbonates with limestones blocks (fig. 6b, c), suggesting a southerly carbonate platform source. The nearest carbonate platform is located in Mundaka, south-east of the MTD1 (fig. 3). This suggests that the MTD1 may be sourced from a lateral equivalent of the Mundaka carbonate platform possibly in Bermeo and presently covered by marls or removed by erosion (fig. 3). The MTD and its hosting succession display relatively similar facies suggesting a short run-out distance.

b. The Gaztelugatxe MTD (MTD2)

The Gaztelugatxe mass-transport deposit is exposed in the eastern flank of the Bakio salt wall (figs. 3 and 4) at the boundary between units 1 and 2 of the Black Flysch Group. It is pinching out onto the Gaztelugatxe escarpment and is interbedded with redeposited carbonates, thin-bedded fine-grained turbidite sandstones and marls. These facies are interpreted carbonate slope- slope apron deposits (Poprawski et al., 2016) related to the carbonate platform growing on top of the Bakio diapir. These deposits progressively pass into deposits of a proximal lobe fringe environment (Cumberpatch et al., 2021). This MTD is 4 m thick and shows two distinct internal facies. The base consists in a 0,5 m thick clast-supported breccia with angular remobilized limestones blocks (fig. 7a). The upper part of the MTD is dominated by slumped siliciclastic thin-bedded fine-grained turbidite sandstones, deposited in proximal lobe fringe environment (Cumberpatch et al., 2021) and embedded in a marly

matrix with decimetre-scale angular blocks of limestones and siderite nodules (fig. 7a, d). MTD2 is dominated by clasts and slumped beds as it comprises only 35% of matrix, the lowest proportion in any MTD in the study area. The basal part of this MTD is interpreted as a carbonate debrite, similar to the carbonate 'lentils' described by Giles and Rowan (2012). The upper part is interpreted as a siliciclastic dominated slump that possibly reworked turbidites from the diapirs roof or flanks, interbedded with carbonate-dominated muddy debrites. The vertical succession within this MTD suggests flow transformation from debris flow to slump or two separated distinct events, related to two periods of failure. Slump folds are dominated by sheath and recumbent folds with low interlimb angles showing small lateral continuity due to clockwise and anticlockwise fold terminations (fig. 7a, b), suggesting layer normal shear. Fold axes have a strong spatial dispersion with common orthogonal trends (fig. 7c). Folds verge in opposite directions and display opposite asymmetry suggesting an apparent E-directed transport, locally (fig. 7c) and an apparent W-directed transport in other areas of the MTD.

Following rotation to horizontal, the mean axis plunges northward (348°/7°) and the mean axial plane is striking NNE-SSW and dipping westward (28°/25°W) (fig. 7e). The MAM and MAPS give two inconsistent transport directions, as they indicate an E-directed (toward 78°) and SE-directed transport (toward 118°), respectively (fig. 7e). This shows that the MTD2 did not form under layer parallel shear. This is verified by the presence of sheath folds, the absence of clear vergence and asymmetry and by the significant fold axes dispersion (fig. 7a, b, c). By contrast, the DAM and the AIM methods provide similar and consistent results with a N-directed (toward 348° and

toward 354°, respectively) or a S-directed transport (toward 168° and 174° respectively) (fig. 7e) suggesting layer normal shear.

MTD2 contains limestone clasts (fig. 7d) thought to be derived from the roof of the Bakio salt wall located north (Poprawski et al., 2016) (fig. 3) and thus the N-directed transport obtained with the DAM and the AIM can be excluded. In addition, local palaeoflows to the SSE favors the S-directed transport mass-transport hypothesis. Consequently, the S-directed transport (from 168° to 174°) inferred for MTD2 (fig. 7e) indicate that the likely source area is related to slope collapse during diapir flank rotation. The MTD and its hosting succession display relatively similar facies suggesting a relatively short transport and run-out distance. These results slightly contrast with previous interpretation, as this MTD was previously interpreted to develop under layer parallel shear in Poprawski et al. (2014), who used the apparent eastward asymmetry to assume an east-directed transport.

c. The Arribolas MTD (MTD3)

The Arribolas mass-transport deposit is exposed between Bermeo and the Matxitxako Cape, 114 m above the base of unit 2 of the Black Flysch Group (figs. 3 and 4). It is 5 m thick. This MTD is observed between medium-bedded, coarse-grained, amalgamated sandstones and thin-medium bedded sandstones interbedded with mudstones. The underlying coarse-grained, amalgamated sandstones that thin out westward (fig. 8a) are interpreted as high-density turbidites deposited in lobe axis environment (Cumberpatch et al., 2021), and the overlying succession is interpreted to represent low-medium density turbidite deposition in a proximal lobe fringe environment (Cumberpatch et al., 2021). MTD3 is composed of two distinct parts. The lower part

consists of folded, thin- and medium-bedded sandstones, which range from fine-coarse grained, and rarer discontinuous siderite beds and nodules, embedded in a muddy matrix (fig. 8a, b). The upper part is composed of folded mudstones including thin-bedded fine-grained sandstones and isolated pillows of sandstones. MTD3 contains 64% of matrix. In the lower part, slump folds are open to tight conical folds with no apparent vergence and with limited spatial dispersion of their axes (fig. 8d). The folded beds are detached from each other and some folds are thrusted with a southward apparent transport sense (fig. 8c). In the upper part, folded layers and laminae have rootless fold geometries as described in Ogata et al. (2014) and Festa et al. (2016). The lower part of the MTD3 can be interpreted as a slump, while the upper part can be interpreted either as a slump developed in mudstone facies or as a muddy debrite carrying small detached slump folds. The vertical succession within this MTD suggests flow transformation from slump to debris flow.

After removal of tectonic tilt, the mean axis is trending NE-SW (58°/1°) and the mean axial plane is striking NE-SW and dipping toward the NNW (57°/10°NW) (fig. 8d). The MAM and the MAPS indicate similar SSE-directed transport (toward 148° and 147°, respectively) (fig. 8d). Here the similar results yielded by mean fold axis and the mean axial plane suggest that the MTD moved toward the SSE (toward 148°) assuming cylindrical structures. However, the rootless folded beds and conical folds suggest that the MTD3 formed in layer normal shear conditions. The DAM suggests a WSW- or a ENE- directed transport (toward 58° or 238°), as the mean fold axis is almost horizontal (fig. 8d). The AIM also provides a WSW- or an ENE-directed transport (toward 63° or 243°) consistent with the results of the DAM (fig. 8d).

MTD3 displays relatively muddier facies compared to the underlying deposits,

suggesting slope failure from an uplifting palaeohigh draped by fine-grained turbidites and mud (e.g. Madof et al., 2009; Mayall et al., 2010; Cumberpatch et al., 2021) and is transported to more basinal areas over deposits of the lobe axis environment. This suggests a relatively significant run-out distance, consistent with the disorganized upper muddy debrite.

d. The Matxitxako MTD (MTD4)

The Matxitxako MTD is exposed in the western cliff of the Matxitxako Cape, at the base of unit 3 of the Black Flysch Group (figs. 3 and 4), and is 2.5 m thick. This MTD is located in an interval composed of thin- to medium bedded fine-to coarse-grained sandy turbidites interbedded with mudstones interpreted as deposited in proximal fringe – lobe-off axis environment (Cumberpatch et al., 2021). The folded beds in MTD4 display relatively homogeneous facies with mainly fine-grained thin-bedded sandstones beds embedded in a muddy matrix (fig. 9a). The lateral bed continuity is partially preserved but intense deformation makes it difficult to follow a single bed laterally (fig. 9a, b). Matrix represent 59% of the deposit. Slump folds are tight, recumbent and sheath folds (fig. 9b). The folds vergence varies locally from SW-verging to NE-verging folds. Imbricate thrusts with opposite vergence suggest a local apparent SW-directed transport that changes laterally to the opposite, NE-direction (fig. 9b). Some faulted and disconnected beds have sigmoidal or C-S structures geometries as described in Ogata et al. (2014) and Festa et al. (2016), also showing apparent SW-directed transport (fig. 9c). This MTD can be regarded as a slump and it has been interpreted as linked with local diapir growth (Cumberpatch et al., 2021).

Following removal of tectonic tilt, the mean axis is plunging toward the SSE

(143°/7°) and the mean axial plane is striking N-S and dipping eastward (11°/18°E) (fig. 9e). The results of the MAM and MAPS differ from about 48°, since the MAM suggests a SW-directed transport (toward 234°) and the MAPS a W-directed transport (toward 281°) (fig. 9e). This difference between the two methods suggests that the MTD4 does not include cylindrical structures. This hypothesis is supported by the changes of the fold vergence, the presence of sheath folds, folded beds and by the significant fold axes dispersion (fig. 9e) that suggests that the MTD4 may be dominated by layer normal shear. DAM and the AIM give consistent results with an SSE-directed transport (toward 143° and toward 154°, respectively). Consequently, MTD4 is interpreted as
being dominated by layer normal shear, with reorientation of fold axes parallel to the transport direction. The results given by the DAM and the AIM are only separated by 11° and thus an SSE-directed transport (from 143° to 154°) is assumed for the MTD4 (fig. 9e).

The SSE-directed transport inferred for MTD4 (from 143° to 154°) (fig. 9e) indicates that it was sourced from an area located offshore at present, north of the Matxitxako Cape. This transport direction is supported by local palaeoflow directions measured in the outcrops of the Matxitxako Cape (fig. 3). Following the inferred SSE-directed transport, the current location of the outcrop and the possible extension of the carbonate platform (Bilbao-Lasa et al., 2020; Roca et al., 2020) along the strike of the Bakio salt wall (fig. 3), it is suggested that MTD4 may be derived from the roof of the Bakio salt wall. The MTD4 displays finer and thinner turbidites facies compared to the underlying deposits, suggesting slope failure from the uplifting roof draped by fine-grained turbidites and mud (e.g. Madof et al., 2009; Mayall et al., 2010; Cumberpatch et al., 2021) and transport into more basinal areas over the deposits of the proximal fringe

– lobe-off axis environment. This suggests a significant run-out distance. This is confirmed by the presence of limestone blocks, possibly derived from the diapir roof in the coarse-grained turbidites located above MTD4 (fig. 9d). This suggests that the Bakio salt wall was still growing and that its carbonate roof was probably exposed at the seafloor during the deposition of the turbidite units located at the Matxitxako Cape. This is verified by the high resolution bathymetric data of Roca et (2020) since the bed traces of these units are thinning toward the carbonate platform, currently offshore (fig. 3).

e. The lower Jata MTD (MTD5)

The lower Jata MTD is exposed in the western flank of the Bakio salt wall, at 1.5 km from the structure, in unit 1 of the Black Flsych Group (figs. 3 and 4). This MTD is about 10 m thick and occurs at the top of a 110 m thick finning-upward interval, comprising amalgamated pebbly medium-bedded turbidites below thinner-bedded, and finer- grained turbidites interbedded with mudstones. This interval is interpreted as a major channel fill sequence (Robles et al., 1988) or as a sinuous channel (Cumberpatch et al., 2021). MTD5 comprises a 2 m thick lower interval dominated by disorganized mudstone including pebbles and centimeter-scale rootless folded muddy sandstones, an intermediate interval with meter-scale rootless folds of fine-grained thin-bedded sandstones and mudstones, and an upper interval dominated by mudstones. Slump folds consists of folded beds with heterogeneous facies including thin-bedded fine-grained turbidites disconnected from each other and siderite beds embedded within a muddy matrix with nodules, quartz gravels and pebbles (fig. 10a, b, c, d). The matrix percentage of this MTD is 81%. Folds are recumbent to sheath folds with refolded geometries (fig. 10b). The complete disconnection of the folded beds with rootless fold

geometries (fig. 10c, d), the refolded geometries, and the amount of mud favors an interpretation of transport and rotation of the elements inside the slumps and suggest that this MTD was dominated by layer normal shear. This MTD could be classified as a transformational flow deposit as it can be described as a muddy debrite carrying detached slump folds that remain preserved. This transformational flow deposit was interpreted by Robles et al. (1989) to be triggered by seismic activity.

After restoration to horizontal, the mean axis trends ESE-WNW (106°/1°) and the mean axial plane is striking ESE-WNW and dipping toward the SSW (108°/7°S) (fig. 10e). Following the MAM and the MAPS, the mean fold axis and the mean axial plane indicate a possible transport direction toward the NNE (toward 16° and 18°, respectively) (fig. 10e). However, the fold axes dispersion suggests that the associated folds may not be cylindrical. This supports the hypothesis of an MTD dominated by layer normal shear and thus the results of the MAM and MAPS can be discarded. Assuming layer normal shear, the DAM gives an ESE-WNW transport direction (toward 106° or 286°, as the mean axis is roughly horizontal). The AIM gives similar results (toward 112° or 292°) (fig. 10e). In layer normal shear, most of the axial planes are assumed to dip downslope but here the axial plane distribution does not allow for the deciphering between an ESE-directed transport or a WNW-directed transport. Consequently, two opposite sources are possible for MTD5.

Following the WNW-directed transport (from 286° to 292°), this MTD may be sourced from the Bakio salt wall, located 1,5 km east of the outcrop where MTD5 is exposed. The opposite ESE-directed transport (from 106° to 112°) suggests another source area, possibly an uplifting palaeohigh located offshore, northwest of the present-day coastline. Since debrites and slumps derived from the Bakio salt wall usually

comprise limestone clasts reworked from the roof (Poprawski et al., 2016; Cumberpatch et al., 2021), the absence of such clast in the MTD5 favors a source from the northwest and not from the Bakio diapir. In addition, the quartz pebbles within the matrix of this MTD (fig. 10c, d) may be initially derived from the Landes Massif or incorporated from reworked coarse-grained turbidites facies during downslope transport, suggesting a significant run-out distance. The diapir roof is interpreted to be covered mainly by fine-grained turbidites and mudstones, and not coarse-grained turbidite facies (Cumberpatch et al., 2021), which supports a source from the north, independent from the Bakio diapir, for MTD5.

f. The upper Jata MTD (MTD6)

The upper Jata mass-transport deposit is exposed between Bakio and Armintza (3.5 km from Bakio), in unit 1 of the Black Flysch Group (figs. 3 and 4). This MTD is interbedded with thin- and medium bedded fine- to coarse-grained turbidite sandstones and mudstones interpreted to be deposited in a channel-lobe transition zone environment (Robles et al., 1988), or lobe axis sub-environment following Cumberpatch et al. (2021). The MTD is about 8 m thick and has a relatively complex internal organization because of lateral variations. The eastern part of the outcrop is dominated by disorganized mudstone including rare meter-scale rootless fold of thin- and medium-bedded sandstones. The western part of the outcrop shows a 3 m thick lower interval with tabular medium-bedded coarse-grained sandstones and an upper interval dominated by folded beds with heterogeneous facies including thin- and medium bedded fine- and coarse-grained sandstones and siderite beds within in a muddy matrix (fig. 11a, b, c, d). The lower interval with tabular sandstones beds displays a clear fold

hinge laterally toward the east and thus can be interpreted as a recumbent and refolded fold with its overturned flank stacked with the normal flank (fig. 11a). The proportion of matrix is 77%. Folds are tight, recumbent and sheath folds with refolded geometries. Some hinges were intensely refolded (fig. 11a) and resemble the spiral recumbent folds described in Alsop and Marco (2013). The recumbent basal fold may correspond to downward facing folds (here, antiformal synclines) that were rotated during a slumping event with multiple failures (fig. 11a). Folds are associated with normal faults that do not affect the roof of the slumped horizon (fig. 11a). The rotation of the hinge of the antiformal synclines together with the normal faults suggests an apparent W-directed transport for the MTD6 (fig. 11a). The rootless folded beds (fig. 11b, c) and the number of marls suggests a significant transport and rotation of the elements inside the slumps suggest that this MTD was dominated by layer normal shear. The lower part of the MTD6 can be interpreted as a slump as bed continuity is preserved, while the upper part can be interpreted as a muddy debrite carrying small detached slump folds. The vertical succession within this MTD suggests flow transformation from slump to debris flow. This MTD was interpreted by Robles et al. (1989) to be triggered by seismic activity.

The mean axis, after rotation to horizontal, trends NNW-SSE (152°/2°) and the mean axial plane stikes ESE-WNW and dips toward the SSW (106°/9°S) (fig. 11e). The MAM and MAPS suggest an NE-directed (toward 62°) and NNE-directed transport (toward 16°), respectively (fig. 11e). The significant fold axes dispersion and the angle of 46° for the transport sense yielded by the MAM and MAPS (fig. 11e) suggests that the MTD6 is not characterized by cylindrical structures formed in layer parallel shear. Assuming layer normal shear, the DAM and the AIM give a S-directed transport (toward 152° and toward 168°, respectively) (fig. 11e). Similar results given by DAM and the AIM

suggest that MTD6 was transported southward (from 152° to 168°) and that it was dominated by layer normal shear.

MTD6 displays muddier facies compared to the underlying deposits, suggesting slope failure from an uplifting palaeohigh draped by fine-grained turbidites and mud (e.g. Madof et al., 2009; Mayall et al., 2010; Cumberpatch et al., 2021) and transport in more basinal areas over deposits of a channel-lobe transition environment. This suggests an significant run-out distance. Following the S-directed transport (from 152° to 168) assumed for the MTD 6, this MTD was sourced from an area, north of the present-day coastline, possibly an uplifting palaeohigh located offshore.

g. The Armintza MTD (MTD7)

The Armintza mass-transport deposit is exposed in the Armintza harbor (stratigraphic section c, fig. 4) and it can be traced to the west of Bakio (stratigraphic section d, fig. 4) following the bed traces on the bathymetric data of Roca et al. (2020) (fig. 3). This MTD is located at the top of unit 1 of the Black Flysch Group (figs. 3 and 4).

In the Armintza harbor, MTD7 is also about 10 m thick and is located above a thick basaltic lava flow (e.g. López-Horgue et al., 2009; Ábalos and Elorza, 2012) in the central cliff of the harbor (fig. 12a). In the eastern cliff of the Armintza harbor, the MTD are located above medium-bedded coarse-grained turbidite sandstones interbedded with mudstones (fig. 12b), as the lava flow wedges out to the East (Ábalos and Elorza, 2012). The lower turbidite sandstones are interpreted as deposited in lobe to channel-lobe transition zone environment (Robles et al., 1988). The MTD is overlain by a 10 m thick interval with similar medium-bedded coarse-grained turbidites interbedded with

mudstones. This coarse-grained interval including MTD7 is overlain by thin-bedded, fine-grained siliciclastic turbidites interbedded with mudstones and siderite beds overlying the medium-bedded coarse-grained turbidites (e.g. Ábalos and Elorza, 2012), interpreted as deposited in a lower slope or basin plain environment (Robles et al., 1988). MTD7 is composed of reworked medium-bedded coarse-grained turbidites and mudstones with facies similar to the underlying interval (fig. 12b). The muddy matrix embedding the folded beds in MTD7 is less abundant compared with the underlying MTDs 5 and 6, as it accounts for 47% of the deposit. Slump folds are open to tight conical and recumbent folds with no apparent vergence, since most of the folds display near horizontal axial planes (fig. 12 a, b). Fold axes have a strong spatial dispersion with common orthogonal trends. The first turbidite beds overlying MTD7 are affected by syn-sedimentary imbricated thrusts to the west and normal faults to the east (fig. 13a, b). These thrusts are striking N-S and dipping eastward (fig. 13c). The eastern cliff displays different slumped sheets bounded by normal faults and thrusts at different scales (fig. 12b, c). Younger slumped sheets truncate the previous one and cause the rotation of older faults (fig. 12b). These geometries suggest an apparent W-directed transport direction for MTD7, considered as a multiple-stage slump event. This slump was interpreted by Robles et al. (1989) as triggered by tectonic activity.

The mean axis is trending N-S (171°/6°) and the mean axial plane is striking NW-SE and dipping toward the SW (127°/16°S) (fig. 12d). The MAM and MAPS suggest an E-directed (toward 81°) and NNE-directed transport (toward 37°), respectively (fig. 12d). Similarly, with the underlying MTD, the fold axes dispersion and the angle of 44° for the transport sense yielded by the MAM and MAPS (fig. 12d) supports the hypothesis of a MTD dominated by layer normal shear. The DAM and the AIM give a S-directed

transport (from 171° to 176°, respectively) (fig. 12d). The results given by the DAM and by the AIM are only separated by 5°, suggesting layer normal shear and a S-directed transport (from 171° to 176°) for MTD7 (fig. 12d). Such transport direction is validated by the adjacent local palaeoflow, which are also dominated by a S-directed transport.

West of Bakio, the MTD7 is about 10 m thick and is located above fine to medium-bedded coarse-grained turbidite sandstones interbedded with mudstones interpreted as deposited in lobe environment (Robles et al., 1988). The 4 m thick basal part corresponds to a debrite made of disorganized meter-scale sandstone pillows, siderite nodules and quartz gravels embedded in a muddy matrix that becomes sandier upward (fig. 13d). The upper part of the MTD is composed of slumped beds of medium-bedded coarse-grained turbidites and mudstones. Only few axial planes and fold axes were measured and thus it does not allow accurate slope direction reconstruction for this outcrop. The lateral correlation from the outcrop at Armintza to the one west of Bakio suggests down-slope flow transformation with the creation of a basal debrite west of Bakio (fig. 13d), suggesting easterly-directed transport. By contrast, the small thrusts affecting the turbidite above MTD7 suggests a W-directed sliding (toward 265°) of the bed associated with the formation of normal faults upslope (fig. 13b) and of thrusts downslope (fig. 13a), using the MFOM. These contradictory apparent E- and W-directed transport directions may be the result of along strike variations within the same MTD transported southward, as changes in structural orientations is common from the central parts to the lateral borders in the same MTD (e.g. Debacker et al., 2009).

In the Armintza harbor, MTD7 displays relatively similar facies compared to the underlying deposits, suggesting limited run-out distance consistent with the preserved bed continuity within slump folds. By contrast, the presence of a basal debrite without

preserved bedding west of Bakio suggests a more significant run-out distance in this area. The S-directed transport (from 171° to 176°) inferred for MTD 7 suggests that it was sourced from an area, located offshore, north of the present-day coastline, possibly an uplifting palaeohigh. The source area for MTD7 was probably the same source area of MTDs 5 and 6, following their similar S-directed transport senses (from 171° to 176° and from 152° to 168°, respectively).

h. Minor Armintza MTD (MTD8)

In the western part of the Armintza harbor, a 2 m thick MTD is exposed in unit 2 of the Black Flysch Group, composed of thin-bedded, fine-grained siliciclastic turbidites interbedded with mudstones and siderite (e.g. Ábalos and Elorza, 2012), interpreted as deposited in a lower slope or basin plain environment (Robles et al., 1988). This MTD shows different anticlines separated by imbricate thrusts (fig. 14a). The folded facies are similar to the hosting unit, suggesting limited transport distances. The west-directed vergence of the folds (fig. 14a) and the thrust orientations, striking N-S and dipping eastward (fig. 14b) also indicate a W-directed transport (toward 263°) using the MFOM. The W-directed transport for these minor MTDs are relatively similar to those inferred by Ábalos and Elorza (2012), who analyzed small-scale slides and slump folds fossilized by siderite precipitation in the same area. This suggests a change in the slope direction compared with the underlying MTD7.

Two other additional MTDs are exposed along the new road from Bakio to Bermeo, at the base of unit 3 of the Black Flysch Group (MTDb, c in fig. 3). Their stratigraphic location at the base of unit 3 suggests that they may roughly correspond to lateral equivalents of the MTD4 (fig. 9). The MTDb is 4 m thick and the MTDc is 7 m

thick (fig. 14c, d). These MTDs consist in rootless folded fine-grained and thin-bedded turbidite sandstones and mudstones and isolated pillows of sandstones within a muddy matrix (fig. 14c, d). The matrix is abundant in MTDb and c as they contain up to 77% and 89%, respectively. The complete disconnection of beds showed by the rootless folds and the isolated pillows of sandstones suggests that these MTDs can be interpreted as muddy debrites. These MTDs are located in more distal areas of the mini-basin (fig. 3), they are muddier and more debritic compared to their possible equivalent (MTD4, fig. 9). This suggests progressive transformation from slumps dominated by folded turbidite sandstone to muddy debrite along the down-slope transport from relatively proximal to more distal areas.

VIII Interpretation:

This section discusses a possible palaeogeographic reconstruction based on the lateral thickness variations in the Black Flysch Group, in the study area. Then, the local paleogeography together with the inferred MTD transport senses are used to identify the local sources for each MTD. In addition, this section also provides an interpretation of matrix percentage, the clast nature and of the estimated MTD length from the source to outcrop, estimated using the location of the source and the outcrop for each MTD.

a) Revised palaeogeographic setting

Lateral thickness variations evidenced by the stratigraphic columns presented in figure 4 allow definition of a revised palaeographic setting for the area, that fit with the recent interpretations of Roca et al. (2020). West of Bakio the total thickness of the

Black Flysch Group reaches up to 1800 m, while it is less than 200 m west of Armintza (fig. 4). In addition, at least three unconformities are identified west of Armintza (S1, S2 and S3 surfaces, fig. 4). The first unconformity (S1 surface, fig. 4) corresponds to an erosive surface marked by karst cavities filled by sandstones, developed on the Early Albian carbonate platform limestones (Pujalte et al., 1987; Robles et al., 1988). This indicates a period of emersion and karst development followed by a drowning by fan-delta deposits of the Monte Grande Fm. (Robles et al., 1988). The Black Flysch Group unit unconformably covers the Early Albian carbonate platform intervals and the fan-delta deposits (S2 surface, fig. 4) (Agirrezabala, 2015; Agirrezabala et al., 2017). The Middle Cenomanian to Santonian Calcareous Flysch is unconformably overlying the Black Flysch Group units (S3 surface, fig. 4) (Agirrezabala et al., 2017). All these elements suggest the presence of a palaeohigh, where the Black Flysch Group and the Middle Cenomanian to Santonian Calcareous Flysch wedge out, as postulated in Robles et al., (1988). This palaeohigh coincides with the footwall of the Armintza sub-salt extensional fault inferred by Roca et al. (2020) (fig. 15). However, the absence of salt at the surface and the 600 m thick Albian to Santonian sediments deposited in the area (fig. 4) suggests that this structure probably remained buried, never piercing the surface.

The depocenter located between the Bakio salt wall and the Armintza fault, where up to 1800 m of Black Flysch Group is deposited may thus be considered as a minibasin, namely the Jata minibasin (fig. 15). Following the location of the Bakio salt wall and the Armintza fault, the width of the Jata minibasin is about 6000 m, which is consistent with minibasin geometries globally (e.g. Madof et al., 2009; Hearon et al.,

2014a, b; Kergaravat et al., 2016; Saura et al., 2016; Martín-Martín et al., 2017; Vergés et al., 2020). The Cormorán-1 well located within the Jata minibasin suggests the absence of salt at depth in the minibasin (e.g. Gómez et al., 2002). This may result from the creation of a primary weld during the Cretaceous and/or of welding during the Cenozoic shortening (Roca et al., 2020) (fig. 15a).

East of Bakio, Roca et al. (2020) defined two distinct minibasins, the Burgoa and the Sollube mini-basins separated by an E-W trending sub-salt extensional fault, called the Bermeo fault (fig. 15). The presence of such fault is not obvious on the field, since the only evidence is the small Triassic outcrop located in the Bermeo town (fig. 3).

b) Source areas for MTDs

MTD source can be defined as the active area where the evacuation was located and where mass-failure started (Moscardelli and Wood 2016 and reference therein). The transport directions inferred for all the MTDs in this study support the palaeogeography described above (fig. 15) and the recent interpretations of Roca et al. (2020). MTDs 2 and 4 are clearly derived from the Bakio salt wall (fig. 15b), demonstrating that it was growing during the deposition of the Bakio breccias Fm. and the Black Flysch Group, as postulated in Rowan et al. (2012), Ferrer et al., (2014) and Poprawski et al. (2014, 2016). The source area for the MTDs 6 and 7 clearly coincides with the footwall of the Armintza sub-salt extensional fault (fig. 15b). MTD5 may be derived from the Bakio salt wall or from the footwall of the Armintza sub-salt extensional fault (fig. 15b). However, the presence of several rounded quartz gravel- to pebble sized clasts within the matrix of the MTD5 (fig. 10c, d) is more consistent with a

source located on the footwall of the Armintza sub-salt extensional fault, that directly received reworked sediment from the Landes Massif. The NNE-directed MTD1 (fig. 6), which includes redeposited carbonates with limestones blocks, suggests a southerly carbonate platform source, possibly located in Bermeo town (fig. 3). This unknown platform was possibly growing at the crest of the Bermeo diapir/sub-salt fault inferred by Roca et al. (2020). Similarly, the ENE-directed MTD3 in unit 2 of the Black Flysch Group also suggests the same source area. The NNE-directed transport of MTD1 and the ENE-directed transport of the MTD3 reinforces the idea of a growing structure located in Bermeo bounding the Burgoa and Sollube minibasins, as proposed by Roca et al. (2020). The NNE- or ENE-directed slope north of Bermeo may be explained either by rotation on the northern flanks of the Bermeo diapir or by a slight northward tilting of the footwall of the Bermeo sub-salt extensional fault.

The palaeogeographic reconstruction of the study area and the measured palaeocurrent directions demonstrate that regionally-derived turbidity currents were flowing axially through the minibasins and were laterally confined between salt structures, similarly to other minibasins (e.g. Gee and Gawthorpe, 2006; Mayall et al., 2010; Back et al., 2011; Oluboyo et al. 2014), while MTDs were transported from the salt structures, in an oblique or orthogonal direction compared with the turbidity flows (fig. 15b). This interpretation is validated by the local palaeoflow south of the Matxitxako Cape, which shows SSW-directed turbidity flows (fig. 15b). These SSW-directed flows may thus be considered as driven along the axis of the Burgoa minibasin (Cumberpatch et al., 2021). By contrast, local turbidity flows near Gaztelugatxe together with the MTDs 2 and 4 rather represent a lateral source roughly

orthogonal with the axial palaeoflow (fig. 15b). A similar configuration may be inferred for the Jata minibasin. West of Bakio, turbidity flows are flowing toward the SSW and may represent flows sourced from the Landes Massif, and subsequently diverted by the Bakio salt wall topography (Poprawski et al., 2014). These palaeoflows possibly represent turbidity currents that flowed along the axis of the Jata minibasin, while the MTDs 6 and 7 are derived orthogonally to the minibasin axis from a lateral source (fig. 15b). The local S-directed palaeoflow near Armintza may represent turbidity flows derived from the Landes Massif, that spilled across the footwall of the Armintza fault and filled laterally in the Jata minibasin (fig. 15b), similarly to other deep-water environments where topographic highs strike perpendicular to the gravity-flow direction (e.g. Madof et al., 2009; Prather et al. 2012; Soutter et al. 2019). This is supported by the deep-incision of the Monte Grande Fm. (surface S2), at the base of the Black Flysch Group (Robles et al., 1988; Agirrezabala, 2015; Agirrezabala et al., 2017). This deep-incision surface may represent erosion at the entry point between a perched and ponded basin north of the footwall of the Armintza fault and the Jata minibasin, similar to that described by Prather et al. (2012) in the Gulf of Mexico.

c. MTDs length estimations

The MTD length is defined as the horizontal distance in the downslope direction following the main axis of a MTD body to its terminal end, excluding the evacuation area (Moscardelli and Wood 2016). This differs from the run-out distance that corresponds to the transport distance for each particle within a MTD (Moscardelli and Wood 2016). Run-out distances within the same MTD may have variable values, as clasts may undergo different amounts of displacements for example because of flow

transformation, or differential settling. The run-out distances can be qualitatively approached in the field by comparing the reworked facies within MTDs with the in situ facies from the hosting succession.

We used the palaeogeographic map (fig. 15b) to infer rough length estimations, taking into account the distance between the potential source area and the current location of each outcrop where MTDs are exposed. MTDs usually have their headwall dominated by extensive structures and their toe by compressive structures (e.g. Frey-MartÍnez et al., 2006 ; Alsop et al., 2016; Cardona et al., 2020). The outcrops in this study are dominated by compressive structures and thus they may represent any part of the compressive toe of larger bodies. In addition, the location of the source area and evacuation area of for each MTD is not accurate. Consequently, the estimated values represent a minimal length from the source to any part of the compressive toe, rather than the real MTD length.

The current distance between the outcrop of MTD1 and the Bermeo diapir/subsalt extensional fault, that was possibly the source for this MTD suggests a minimum length of about 800 m (fig.15b). Since MTD2 pinches out onto the Gaztelugatxe escarpment that bounds the carbonate platform located above the Bakio salt wall (fig. 3) (Poprawski et al., 2014, 2016), a minimum length of 100 m is assumed (fig.15b). The current distance between the outcrop of MTD3 and the Bermeo diapir/subsalt extensional fault, that was possibly the source for this MTD, suggests a minimum length of about 1600 m (fig.15b). The current distance between the outcrop of MTD4 and the carbonate platform located offshore along the strike of the Bakio salt wall (fig. 15b) gives an estimation of the minimum length of 2000 m. MTD5 is devoid of

carbonate clasts typically derived from the Bakio diapir and thus it probably comes from the footwall of the Armintza fault (fig. 15b). The minimum length assuming the Bakio salt wall is the source, is 1500 m and assuming the footwall of the Armintza fault is the source is up to 2000 m. The current distance between the outcrops of MTDs 6 and 7 and their possible source suggests a minimum length of 2000 m and of 1000 m, respectively (fig.15b).

d. Clasts nature and matrix proportion in MTDs

In this section, the relationships between the MTD minimum length, the clast nature and the matrix proportion are discussed for the MTDs of the Burgoa and Jata minibasins.

MTD2 contains both limestone debris in the basal debrite and in the matrix, and slump folds composed of turbidite sandstones in its upper part. Individual fossils among the carbonate debris suggests this MTD recorded the last mass-failure from the active platform, since it is covered by the first pure siliciclastic interval of unit 2 (Cumberpatch et al., 2021). The slumped turbidite sandstones have relatively similar facies compared to the overlying interval of unit 2, interpreted as deposited in a proximal lobe fringe environment (Cumberpatch et al., 2021). This suggests slope failure from the last remaining carbonate platform patches above the Bakio diapir followed by incorporation of turbidite sandstones during the down-slope transport across a proximal lobe fringe environment. Since MTD2 is probably deposited while the carbonate platform was still active, it is considered here as a carbonate-dominated MTD, although it could be also classified as a mixed MTD.

The carbonate-dominated MTDs (MTDs 1, 2) from the Burgoa minibasin display

carbonate clasts, reworked from a carbonate platform (figs 6a,b and 7a), and individual fossils that are similar to those hosting redeposited carbonates, suggesting a relatively short run-out distance. MTD2 is inferred to have a minimum length of only 100 m (fig. 15b) and exhibits a relatively low proportion of matrix (35%), consistent with the proximity to the carbonate platform growing above the Bakio salt wall. However, abundant individual carbonate clasts mixed in the matrix are below the resolution of the method use to estimate the proportion of matrix and thus this proportion may be slightly overestimated. MTD1 has an estimated minimum length of about 800 m (fig. 15b) and a high percentage of matrix (75%), coherent with a more distal location with respect to the source area. These results are consistent with the downslope clast distribution within MTDs, that may reflect the initial redeposited carbonate facies distributed along the slope, which are slightly disturbed by downslope migrating deformation, similarly to recent work (Le Goff et al. 2018). This suggests an initial sedimentary transport by rock falls, gravel and grain flows (Poprawski et al., 2016) from the carbonate platforms toward the slope and subsequent sliding of redeposited carbonates during the MTDs emplacement (Poprawski et al., 2016). These MTDs are thus interpreted to initiate in clast-rich redeposited facies near the platform and, following the downslope migration and deformation of muddier facies, is predicted in the more distal areas.

The siliciclastic-dominated MTDs (MTDs 3, 4, 5, 6, 7) from the Jata and Burgoa minibasins are devoid of shallow-water clasts and commonly comprised of reworked turbidites (figs. 8, 9, 10, 11, 12). MTDs 4 and 7 display relatively homogeneous reworked facies and a relatively low proportion of matrix, (59% and 47%; figs. 9 and 12), respectively. In MTD4, reworked facies are slightly finer and muddier than the underlying deposits and the folded beds show a partial lateral continuity, despite the presence of

sheath folds. MTD7 shows relatively similar facies compared to its underlying deposits. In deep-water siliciclastic dominated minibasins, coarse-grained turbidites are usually confined between the adjacent diapirs and thus restricted to the axial part of the minibasins, while fine-grained turbidites and mud drapes the diapir roofs (e.g. Madof et al., 2009; Mayall et al., 2010; Cumberpatch et al., 2021). This suggests that MTDs 4 and 7 initiated on the flanks of the adjacent salt structures in muddy facies and then interacted with local coarser facies in proximal fringe – lobe-off axis environments, since MTD are able to incorporate pieces of the underlying substrate (e.g. Ogata et al., 2014; Sobiesiak et al., 2016, 2018; Cardona et al., 2020). MTD7 may have incorporated more pieces of substrate or possibly underwent a more limited run-out transport compared to MTD4, as it displays relatively similar facies compared to its underlying deposits. In MTD7, the presence of a basal sand-rich debrite west of Bakio (fig. 13d) suggests down-slope flow transformation may occur. Similarly, if the two MTDs (MTDb, c) located along the new road from Bakio to Bermeo (fig. 14c, d) could be roughly considered as the lateral equivalents of the MTD4 (fig. 9), this suggests flow transformation from slumps (with 59% of matrix) to muddier debrites (with 77% and 89 % of matrix). This suggests that the toe of such MTDs may be dominated by mud-rich or clast-rich debrites.

MTD3, 5 and 6 show more heterogeneous reworked facies including fine and medium grained turbidites, siderite layers and nodules and quartz pebbles (only in MTD5) (figs 10 and 11) and a relatively high proportion of matrix, 81%, 77% and 64% respectively. These values may be slightly overestimated as centimeter scale clasts are abundant (figs. 10c, d and 11c, d), but under the image resolution. These MTDs are characterized by rootless folds, completely disconnected beds and by refolded structures suggesting an intense layer normal shear. The presence of siderite usually

found in basin plain environments (e.g. Ábalos and Elorza, 2012) together with quartz pebbles usually found in channel-lobe transition zone deposits (e.g. Cumberpatch et al., 2021) suggest reworking of different environments during the downslope transport of MTD5. In addition, these MTDs display relatively different facies compared to their underlying deposits suggesting a relatively significant run-out distance, consistent with the reworked heterogeneous facies, the rootless folds and their associated debritic facies. Compared with MTDs 4 and 7 (59% and 47% of matrix respectively), MTDs 3, 5 and 6 have also a relatively short length (≤2000 m) but a higher proportion of matrix (81%, 77% and 64% respectively). Assuming slope failure in muddy facies similar to those of MTDs 4 and 7 and relatively similar length, MTDs 3, 5 and 6 were possibly transported over muddier substrates compared with MTDs 4 and 7 and thus were not able to incorporate coarse facies in by the same proportion, due to the lack of coarser facies. Alternatively, flow evolution from turbulent to laminar, may have favored a down-slope transport of muddier facies (e.g. Cardona et al., 2020).

IX Discussion

This section compares the MTDs of the Jata and Burgoa minibasins with other MTDs from salt dominated basins and margins, worldwide. It also addresses the triggering processes for the local MTDs in the study area.

a. Sources for MTDs and comparison with subsurface analogs

MTDs can be classified according to their source areas and triggering mechanisms. Following the classification of Moscardelli and Wood (2008, 2016), regionally-derived MTDs or attached MTDs can be shelf-attached or slope-attached and

usually reach thousands of square kilometers in area and hundreds of meters in thickness. They may be triggered by sea level variations, regional tectonics, or high sedimentation rates (Moscardelli and Wood, 2016). Locally-derived MTDs or detached MTDs correspond to localized units, only reaching tens of square kilometers in area and triggered by local processes. Regionally-derived, also called extra-basinal, MTDs found in salt controlled basins commonly consist of debrites associated with rafted blocks and are usually devoid of preserved slumps because of their long run-out distance (Gamboa et al., 2011; Jackson, 2012 ; Omosanya and Alves, 2013 ; Ward et al., 2018; Doughty-Jones et al., 2019). The length of locally-derived MTDs from salt-controlled basins ranges from 1000 to 10000 m (Madof et al., 2009 ; Arfai et al., 2016 ; Gamboa and Alves, 2016 ; Doughty-Jones et al., 2019 ; Wu et al., 2020). They commonly show more preserved structures including slide deposits and folded strata, normal faults in their headwall and imbricate thrusts in their toe (Madof et al., 2009; Gamboa and Alves, 2016; Doughty-Jones et al., 2019), consistent with their relative small length and limited run-out distance. Tripsanas et al. (2004) described slumps near the diapirs that evolve laterally to muddier debris flows near the center of minibasins.

In the Jata and Burgoa minibasins, the studied MTDs are clearly sourced from the local, adjacent structures, including the Bakio salt wall and the footwalls of the Armintza and Bermeo sub-salt extensional faults (fig. 15b). The minimum length estimations for the MTDs from the Jata and Burgoa minibasins are in line with the locally sourced MTDs in the aforementioned literature from other salt-controlled basins, since they range from 100 to 2000 m long. The reworked facies within these MTDs are also consistent with local sources, as they are relatively similar to their host rocks. In addition, MTDs 1, 2, 3,

4 and 7 are dominated by slides and slumps and contain relatively well-preserved strata (figs. 6, 7, 8, 9 and 12). Only MTDs 5 and 6 are muddier with disconnected rootless folds (figs. 10 and 11). All this evidence suggests that MTDs in the Jata and Burgoa minibasins are locally-derived MTDs, similar to those described in Madof et al. (2009), Arfai et al. (2016), Gamboa and Alves (2016), Doughty-Jones et al. (2019) and Wu et al. (2020). MTDs 5 and 6 may correspond to the distal part of similar MTDs, similarly to the study of Tripsanas et al. (2004) and Cardona et al. (2020). However, MTD5 may also have a more regional signature because of the higher facies heterogeneity among its clasts and reworked beds, which include quartz gravels and pebbles (fig. 10b, c, d). The presence of these pebbles and gravels suggests the initial source area as the Landes Massif. This suggests an initial phase of sediment transfer from the Landes Massif to the footwall of the Armintza fault, by gravity-driven process and then local slope failure reworking the pebble-rich facies, following a 'fill-and-spill' model (e.g. Prather et al. 2012; Soutter et al. 2019). Alternatively, MTD5 may be sourced directly from the Landes Massif and thus it may be considered as a regionally-derived or slope-attached MTD, following the classification of Moscardelli and Wood (2016). similar with those described in Jackson, (2012), Ward et al., (2018) and Doughty-Jones et al. (2019). This is supported by the debritic character of MTD5. However, the small size of MTD5 suggests that it more likely to represent a locally derived MTD.

b. Seal and reservoir potential in MTDs,

Few subsurface studies focus on the facies of locally-derived MTDs in salt-controlled basins, since such facies are often below the scale of seismic data and thus

facies studies concentrate on cored data, which is usually of commercial interest and therefore not publically available for academic studies. Since fine-grained turbidites and mud usually drape the diapir roofs, locally-derived MTDs are assumed to be mud-rich (Madof et al., 2009). However, in the North Sea Davison et al. (2000) reported locally-derived Palaeocene MTDs including clasts of Cretaceous chalk mixed inside a muddy matrix, derived from the adjacent diapirs. In addition, Wu et al. (2019) described locally-derived MTDs containing from 40 to 60 % sandstone. This shows that the nature of facies within MTDs in salt controlled basins can be widely variable between different minibasins.

This field-based study brings some new ideas regarding the possible facies reworked within locally-derived MTDs. When the apex of the diapirs remain in deep-water environments, they are assumed to receive mainly mud and find-grained turbidites (Madof et al., 2009 ; Mayall et al., 2010 ; Cumberpatch et al., 2021). Consequently, slope failure creating MTDs are assumed to occur by diapir flank steepening in muddy facies (fig. 16 a, b). However, during their downslope trajectories MTDs may interact with other allocyclically-derived facies deposited at the sea floor. If these MTDs are transported above a muddy substrate, they may remain relatively muddy and thus they may have relatively good sealing properties in a hydrocarbon system, near and away from the diapirs as postulated by Madof et al. (2009) (fig. 16a). Such MTDs are exemplified by MTD 5 and 6 from the Jata minibasin (with up to 81% and 77% of matrix, respectively at 2000 m from the source).

If the trajectory of a locally-derived muddy MTD includes substrates with coarser facies, it may incorporate portions of the substrate (e.g. Ogata et al., 2014; Sobiesiak et al., 2016, 2018; Cardona et al., 2020) and thus the percentage of clasts and reworked

beds may increase, away from the source (fig. 16b). An increase the number of porous material may decrease the sealing properties of these MTDs away from the diapirs, and even enhance reservoir properties of these MTDs. This case may be illustrated by the MTDs 4 and 7 (with 59% of matrix at 2000 m from the source and 47% of matrix at 1000 m from the source, respectively) and by the sand-rich MTDs described in Wu et al., (2019) (including 40 to 60 % of clasts and reworked beds). In these MTDs, down-slope flow evolution may occur, suggesting that the toe of such MTDs may be dominated by clast-rich (fig. 13d)or mud-rich debrites (fig. 14c, c) .

MTDs 1 and 2 show specific clasts (here shallow-water carbonates) may be exported to deep-water environments, when the facies developed on the diapir roofs strongly differs from the facies in the adjacent minibasins (fig 15c, d). This may be the case when carbonate platforms are growing on the crest of diapirs in the photic zone, while the adjacent depocenters mainly received deep-water facies, like in Bakio (Poprawski et al., 2016) (fig. 16c). The comparison between MTD1 (100 m from the source and 35% of matrix) and 2 (800 m from the source and 75% of matrix) suggests that the proportion of matrix may increase away from the diapirs and the associated carbonate platforms for these MTDs, reflecting the lack of ability of mass failures to transport large clasts long distances. Consequently, such MTDs may have good reservoir properties near diapir, while their distal toe may be muddier with good sealing properties (fig. 16c).

All these elements suggest that reservoir and sealing properties could be roughly predicted for MTDs in subsurface studies by characterizing the nature of the diapir roof and the nature of the facies at the seafloor found along the MTDs trajectories. For siliciclastic-dominated MTDs, the seal risk may be reduced by drilling near the diapir, as

postulated by Madof et al., (2009), since coarse-grained porous facies are restricted to the axial part of the minibasins. By contrast, the seal risk increases near the diapir for carbonate-dominated MTDs, since redeposited carbonates with porous facies are redeposited near the diapir, if the carbonate platform grows above the topographic high. Regardless of the type of MTD, the geometries of the internal structures must be studied since internal thrusts for example may form paths for fluids (e.g. Wu et al., 2019; Cardona et al., 2020).

c. Triggering processes for MTDs in the Jata and Burgoa minibasins

In salt-controlled basins, the primary process triggering locally-derived MTDs is halokinesis (Davison et al., 2000; Madof et al., 2009; Back et al., 2011; Gamboa et al., 2011; Omosanya and Alves, 2013; Arfai et al., 2016; Gamboa and Alves, 2016; Doughty-Jones et al., 2019; Wu et al., 2020). Following the halokinetic sequence model (Giles and Lawton, 2002; Giles and Rowan, 2012), MTDs are inferred to occur during relatively low sediment accumulation rates, allowing the diapir to reach the surface, inducing rotation of its flanks and gravitational destabilization of its roof (fig. 16a).

In the Jata and Burgoa minibasins, the studied MTDs are locally-derived and thus halokinesis may is the primary trigger for these MTDs, since they were sourced from the Bakio salt wall and the footwalls of the Armintza and Bermeo sub-salt faults (fig. 15b). However, the studied MTDs are concentrated near the Middle to Late Albian boundary. This boundary is characterized by a regional unconformity or hiatus present at the margins of the Basque-Cantabrian basin (e.g. García-Mondéjar et al., 1996; Agirrezabala and López-Horgue, 2017), recently interpreted as the result of the transition from crustal thinning to mantle exhumation (Rowan, 2014). This suggests that

the studied MTDs were probably triggered by a combination of salt growth responding to more regional tectonics and to low sedimentation rates. Roca et al. (2020) assumed that the Armintza and Bermeo sub-salt faults and the basal salt detachment became inactive and that the Bakio diapir growth was mainly governed by differential loading during Late Albian. Less regional tectonic activity and limited salt growth may thus explain the decrease of the amount of MTDs in the upper part of the Black Flysch Group (fig. 4).

MTDs 1 and 2 (figs. 6, 7) show abundant carbonate clasts including individual fossils that indicate an active carbonate production top of the Bakio salt wall and possibly top of the Bermeo diapir/sub-salt fault. Aggradation of carbonate platform in relative sea level rise settings (Poprawski et al., 2016) may also favored the building of steep clinoforms and thus slope destabilization. Consequently, MTDs 1 and 2 were possibly triggered by a combination of salt growth and aggradation of the platform that also favored slope destabilization.

The footwall of the Armintza fault considered as the source for MTDs 5, 6 and 7 probably remained buried since it was covered by an up to 600 m thick package of Albian to Santonian sediments (fig. 15a), suggesting elevated sedimentation rates in the area. This suggests that slope failure associated with the emplacement of MTDs 5, 6 and 7 may also be triggered by high sedimentation rates generating an increase of fluid pore pressures and thus slope instability.

X Conclusions

The Burgoa and Jata minibasins adjacent to the Bakio salt wall provide a new outcrop-based example of MTDs related to both growing diapirs and regional tectonics.

This study highlights key elements concerning: (i) the understanding of the local palaeogeography controlling the transport direction of MTDs in the study area (ii), the distinction of three different types of locally-derived MTDs in minibasins and (iii) the reservoir and sealing potential of MTDs in deep-water minibasins. These new elements are detailed below:

(1) The comparison between different structural methodologies assuming layer parallel (MAM, MAPS, MFOM) and normal shear (DAM, AIM, GFPM) used in this study is a useful approach for the reconstruction of transport direction in MTDs at the outcrop. The inferred transport directions for MTDs can be compared to turbidity current directions that provide additional information about slope direction. Facies comparison within MTDs and in their hosting succession allows approaching qualitatively the run-out distance for local outcrops. Finally, assumptions about the source areas and MTD length can be made when all these information are summarized together with palaeogeographic information in a comprehensive way,

(2) Using slumping sense reconstruction methods, this study demonstrates that the MTDs 5, 6 and 7 are derived from the footwall of the Armintza sub-salt extensional fault, MTDs 2 and 4 are derived from the Bakio salt wall and MTD1 is derived from the Bermeo diapir/sub-salt extensional fault. This supports the palaeogeography recently defined by Roca et al. (2020), with two minibasins adjacent of the Bakio salt wall: the Burgoa and Jata minibasins. MTDs in this study are derived from local growing salt structures and thus, they are interpreted as locally-derived MTDs, triggered by salt growth associated with regional tectonics, although other triggers such as slope steepening associated with carbonate platform aggradation and salt withdrawal cannot

be excluded.

(3) Three types of diapir-associated MTDs are defined using seven outcrop examples from the Jata and Burgoa minibasins and comparison to subsurface examples. They differ by their source and clast type. In deep-water environments, MTDs are assumed to initiate as mud dominated bodies since the diapir apex mainly received fine-grained facies. During their downslope trajectories, MTDs may interact only with muddy facies and thus remain relatively muddy. These MTDs are assumed to be dominated by mud from their headwall to their toe. By contrast, after their initiation in muddy facies at the diapir crest, MTDs may interact with coarser facies during their downslope trajectories and thus they may incorporate sands. In this case, their headwalls are mud-dominated, their translational domains may become relatively sand-rich, while their toes may be dominated by mud-rich or clast-rich debrites related to dissagregation during flow evolution. When the apex of diapir is in the photic zone, carbonate platforms may develop and thus diapir growth may induce the genesis of carbonate-dominated MTDs. These MTDs highly differ from the siliciclastic counterparts since their headwall are dominated by carbonate platform-derived clasts and their toe by mud.

(4) This study suggests that reservoir and sealing properties could be roughly predicted for MTDs in subsurface studies by characterizing the nature of the diapir roof and the nature of the facies at the seafloor found along the MTDs trajectories. MTDs initiated from diapirs in deep-water environments tend to have relatively good sealing properties from the headwall to their toe, if there are no interactions with coarser facies at the sea floor. If coarse facies are present on the seafloor, sands incorporated by MTDs may form paths for fluids (“thief sands”) and thus may decrease the sealing potential. MTDs

initiated from diapirs with their apex in the photic zone associated with syn-kinematic carbonate platform growth tend to have high risk seals near diapirs, due to the high proportion of clasts and reworked beds with a good porosity.

XI Acknowledgements

The authors would like to thank the ARNT-CIFRE and Geolink, for the funding of the Ph.D. work of Yohann Poprawski. Yohann Poprawski also wish to acknowledge Luis M. Agirrezabala for helpful discussion about the stratigraphy of the area. The authors also thank Pau Arbués for his detailed and constructive comments and suggestions that greatly improved the manuscript. Associate Editor Roberto Tinterri is thanked for the handling of the manuscript.

XII References

Ábalos, B. (**2016**). *Geologic map of the Basque-Cantabrian Basin and a new tectonic interpretation of the Basque Arc.*, Int J Earth Sci (Geol Rundsch) 105: 2327–2354, doi: https://doi.org/10.1007/s00531-016-1291-6.

Ábalos, B. and Elorza, J. (**2012**). *Structural Diagenesis of Siderite Layers in Black Shales (Albian Black Flysch, Northern Spain)*, The Journal of Geology 120: 405-429.

Agirrezabala, L. (**1996**). *El Aptiense-Albiense del Anticlinorio Nor-Vizcaino entre Gernika y Azpeitia*, PhD Thesis, Euskal Herriko Unibertsitatea, Bilbo, 429 pp.

Agirrezabala, L.; Sarrionandia, F. and Carracedo-Sánchez, M. (**2017**). *Diatreme-forming volcanism in a deep-water faulted basin margin: Lower Cretaceous outcrops from the Basque-Cantabrian Basin, western Pyrenees*, Journal of Volcanology and Geothermal Research 337: 124 – 139, doi: https://doi.org/10.1016/j.jvolgeores.2017.03.019.

Agirrezabala, L. M. (**2015**). *Syndepositional forced folding and related fluid plumbing above a magmatic laccolith: Insights from outcrop (Lower Cretaceous, Basque-Cantabrian Basin, western Pyrenees)*, Geological Society of America Bulletin 127 (7-8): 982–1000, doi: https://doi.org/10.1130/B31192.1.

Agirrezabala, L. M. and López-Horgue, M. A. (**2017**). *Environmental and ammonoid faunal changes related to Albian Bay of Biscay opening: Insights from the northern margin of the Basque-Cantabrian Basin*, Journal of Sea Research 130: 36 – 48, doi: https://doi.org/10.1016/j.seares.2017.04.002.

Agirrezabala, L. M.; Permanyer, A.; Suárez-Ruiz, I. and Dorronsoro, C. (**2014**). *Contact metamorphism of organic-rich mudstones and carbon release around a magmatic sill in the Basque-Cantabrian Basin, western Pyrenees*, Organic Geochemistry 69: 26 – 35, doi: https://doi.org/10.1016/j.orggeochem.2014.01.014.

Alsop, G.; Marco, S.; Weinberger, R. and Levi, T. (2016). Sedimentary and structural controls on seismogenic slumping within mass transport deposits from the Dead Sea Basin, Sedimentary Geology, *344*, 71 – 90, doi: https://doi.org/10.1016/j.sedgeo.2016.02.019.

Alsop, G. I. and Holdsworth, R. E. (**2007**). *Flow perturbation folding in shear zones*, Geological Society, London, Special Publications 272: 75-101, doi: https://doi.org/10.1144/GSL.SP.2007.272.01.06.

Alsop, G. I. and Marco, S. (**2012**). *A large-scale radial pattern of seismogenic slumping towards the Dead Sea Basin*, Journal of the Geological Society 169: 99-110, doi: http://dx.doi.org/10.1144/0016-76492011-032.

Alsop, G. I. and Marco, S. (**2013**). *Seismogenic slump folds formed by gravity-driven tectonics down a negligible subaqueous slope*, Tectonophysics 605: 48 – 69, doi: https://doi.org/10.1016/j.tecto.2013.04.004.

Arfai, J.; Lutz, Rü.; Franke, D.; Gaedicke, C. and Kley, J. (**2016**). *Mass-transport deposits and reservoir quality of Upper Cretaceous Chalk within the German Central Graben, North Sea*, International Journal of Earth Sciences 105: 797-818, doi: https://doi.org/10.1007/s00531-015-1194-y.

Aurell, M.; Bádenas, B.; Ipas, J. and Ramajo, J. (**2010**). *Sedimentary evolution of an Upper Jurassic epeiric carbonate ramp, Iberian Basin, NE Spain*, Geological Society, London, Special Publications 329: 89-111, doi: https://doi.org/10.1144/SP329.5.

Aurell, M.; Robles, S.; Bádenas, B.; Rosales, I.; Quesada, S.; Meléndez, G. and García-Ramos, J. (**2003**). *Transgressive-regressive cycles and Jurassic palaeogeography of northeast Iberia*, Sedimentary Geology 162: 239 – 271, doi: https://doi.org/10.1016/S0037-0738(03)00154-4.

Back, S.; Van Gent, H.; Reuning, L.; Grötsch, J.; Niederau, J. and Kukla, P. (**2011**). *3D seismic geomorphology and sedimentology of the Chalk Group, southern Danish North Sea*, Journal of the Geological Society 168: 393-406, doi:

https://doi.org/10.1144/0016-76492010-047.

Bilbao-Lasa, P.; Jara-Muñoz, J.; Pedoja, K.; Álvarez, I.; Aranburu, A.; Iriarte, E. and Galparsoro, I. (**2020**). *Submerged Marine Terraces Identification and an Approach for Numerical Modeling the Sequence Formation in the Bay of Biscay (Northeastern Iberian Peninsula)*, Frontiers in Earth Science 8: 47, doi: https://doi.org/10.3389/feart.2020.00047.

Bradley, D. and Hanson, L. (**1998**). *Paleoslope Analysis of Slump Folds in the Devonian Flysch of Maine*, The Journal of Geology 106: 305-318.

Brinkmann, R. and Logters, H. (**1968**). *Diapirs in western Pyrenees and foreland, Spain*, American Association of Petroleum Geologists Memoir 8: 275-292.

Cámara, P. (**2017**). *Chapter 17 - Salt and Strike-Slip Tectonics as Main Drivers in the Structural Evolution of the Basque-Cantabrian Basin, Spain*. In: Soto, J. I.; Flinch, J. F. & Tari, G. (Ed.), *Permo-Triassic Salt Provinces of Europe, North Africa and the Atlantic Margins*, Elsevier, pp 371-393, doi: https://doi.org/10.1016/B978-0-12-809417-4.00018-5.

Cardona, S., Wood, L.J., Dugan, B., Jobe, Z. and Strachan, L.J. (2020). Characterization of the Rapanui mass-transport deposit and the basal shear zone: Mount Messenger Formation, Taranaki Basin, New Zealand. Sedimentology, 67: 2111-2148, doi: https://doi.org/10.1111/sed.12697.

Castañares, L. M.; Robles, S.; Gimeno, D. and Vicente Bravo, J. C. (**2001**). *The Submarine Volcanic System of the Errigoiti Formation (Albian-Santonian of the Basque-Cantabrian Basin, Northern Spain): Stratigraphic Framework, Facies, and Sequences*, Journal of Sedimentary Research 71: 318-333, doi: https://doi.org/10.1306/080700710318.

Cuevas, J. and Tubía, J. (**1999**). *The discovery of scapolite marbles in the Biscay Synclinorium (Basque–Cantabrian basin, Western Pyrenees): geodynamic implications*, Terra Nova 11: 259-265, doi: https://doi.org/10.1046/j.1365-3121.1999.00255.x.

Cumberpatch, Z.A., Kane, I. A., Soutter, E.L., Hodgson, D.M., Jackson, C.A-L., Kilhams, B.A. and Poprawski, Y. (2021). Interactions between deep-water gravity flows and active salt tectonics. *Journal of Sedimentary Research* 91 (1): 34–65, doi: https://doi.org/10.2110/jsr.2020.047.

Davison, I.; Alsop, G.; Evans, N. and Safaricz, M. (**2000**). *Overburden deformation patterns and mechanisms of salt diapir penetration in the Central Graben, North Sea*, Marine and Petroleum Geology 17: 601 – 618, doi: https://doi.org/10.1016/S0264-8172(00)00011-8.

Debacker, T. N.; Dumon, M. and Matthys, A. (**2009**). *Interpreting fold and fault geometries from within the lateral to oblique parts of slumps: A case study from the Anglo-Brabant Deformation Belt (Belgium)*, Journal of Structural Geology 31: 1525 – 1539, doi: https://doi.org/10.1016/j.jsg.2009.09.002.

De Graciansky, P.C., Hardenbol, J., Jacquin, T., Vail, P.R. (1998). Mesozoic and Cenozoic Sequence Stratigraphy of European Basins. SEPM Special Publication, 60, 786 pp, doi: https://doi.org/10.2110/pec.98.02.

Doughty-Jones, G.; Lonergan, L.; Mayall, M. and Dee, S. (**2019**). *The role of structural growth in controlling the facies and distribution of mass transport deposits in a deep-water salt minibasin*, Marine and Petroleum Geology 104: 106 – 124, doi: https://doi.org/10.1016/j.marpetgeo.2019.03.015.

Ducoux, M.; Jolivet, L.; Callot, J.-P.; Aubourg, C.; Masini, E.; Lahfid, A.; Homonnay, E.; Cagnard, F.; Gumiaux, C. and Baudin, T. (**2019**). *The Nappe des Marbres Unit of the Basque-Cantabrian Basin: The Tectono-thermal Evolution of a Fossil Hyperextended Rift Basin*, Tectonics 38: 3881-3915, doi: https://doi.org/10.1029/2018TC005348.

Espejo, J. (**1973**). *Mapa Geológico de España 1:50.000, Hoja 38 (Bermeo). Segunda Serie (MAGNA), Primera Edición IGME*.

Espejo, J. and Pastor, F. (**1973.**). *Mapa Geológico de España 1:50.000, Hoja 37 (Algorta). Segunda Serie (MAGNA), Primera Edición IGME*.

Farrell, S. (**1984**). *A dislocation model applied to slump structures, Ainsa Basin, South Central Pyrenees*, Journal of Structural Geology 6: 727 – 736, doi: https://doi.org/10.1016/0191-8141(84)90012-9.

Ferrer, O.; Roca, E.; Benjumea, B.; Muñoz, J.; Ellouz, N. and MARCONI-Team (**2008**). *The deep seismic reflection MARCONI-3 profile: Role of extensional Mesozoic structure during the Pyrenean contractional deformation at the eastern part of the Bay of Biscay*, Marine and Petroleum Geology 25: 714 – 730, doi: https://doi.org/10.1016/j.marpetgeo.2008.06.002.

Ferrer, O.; Arbués, P.; Roca, E.; Giles, K.; Rowan, M. G.; De Matteis, M. and Muñoz, J. A. (**2014**). *Effect of Diapir Growth on Synkinematic Deepwater Sedimentation: The Bakio Diapir (Basque-Cantabrian Basin, Northern Spain)*, American Association of Petroleum Geologists Annual Convention and Exhibition Houston, USA.

Festa, A.; Ogata, K.; Pini, G. A.; Dilek, Y. and Alonso, J. L. (**2016**). *Origin and significance of olistostromes in the evolution of orogenic belts: A global synthesis*, Gondwana Research 39: 180 – 203, doi: https://doi.org/10.1016/j.gr.2016.08.002.

Frey-Martínez, J.; Cartwright, J. and James, D. (**2006**). *Frontally confined versus*

frontally emergent submarine landslides: A 3D seismic characterisation, Marine and Petroleum Geology 23: 585 – 604, doi: https://doi.org/10.1016/j.marpetgeo.2006.04.002.

Gamboa, D.; Alves, T. and Cartwright, J. (**2011**). *Distribution and characterization of failed (mega)blocks along salt ridges, southeast Brazil: Implications for vertical fluid flow on continental margins*, Journal of Geophysical Research; B08103, doi:10.1029/2011JB008357.

Gamboa, D. and Alves, T. M. (**2016**). *Bi-modal deformation styles in confined mass-transport deposits: Examples from a salt minibasin in SE Brazil*, Marine Geology 379: 176 – 193, doi: https://doi.org/10.1016/j.margeo.2016.06.003.

Garcia-Tortosa, F. J.; Alfaro, P.; Gibert, L. and Scott, G. (**2011**). *Seismically induced slump on an extremely gentle slope (< 1) of the Pleistocene Tecopa paleolake (California)*, Geology 39: 1055-1058, doi: https://doi.org/10.1130/G32218.1.

García-Mondéjar, J.; Agirrezabala, L. M.; Aranburu, A.; Fernández-Mendiola, P. A.; Gómez-Pérez, I.; López-Horgue, M. and Rosales, I. (**1996**). *Aptian— Albian tectonic pattern of the Basque— Cantabrian Basin (Northern Spain)*, Geological Journal 31: 13-45, doi: https://doi.org/10.1002/(SICI)1099-1034(199603)31:1<13::AID-GJ689>3.0.CO;2-Y.

García-Mondéjar, J.; Fernández-Mendiola, P.; Agirrezabala, L.; Aranburu, A.; López-Horgue, M.; Iriarte, E. and Martinez de Rituerto, S. (**2004**). *Extensión del Aptiense-Albiense en la Cuenca Vasco-Cantábrica*, Geología de España, 340-343.

García-Mondéjar, J. and Robador, A. (**1987**). *Sedimentación y paleografía del Complejo Urgoniano (Aptiense-Albiense) en el área de Bermeo (región Vasco-Cantábrica septentional)*, Acta geológica hispánica 21: 411-418.

Garrote-Ruiz, A.; García-Potero, J.; A., A.-G.; Eguiguren-Altuna, E. and García-Pascual, I. (**1991**). *Mapa de la Hoja n° 38-I (Bermeo) del Mapa Geológico del País Vasco a escala 1:25.000. Ente Vasco de la Energía-EVE, Bilbao.*

Garrote-Ruiz, A.; García-Potero, J.; A., A.-G.; Eguiguren-Altuna, E. and García-Pascual, I. (**1992**). *Mapa de la Hoja n° 38-III (Mungia) del Mapa Geológico del País Vasco a escala 1:25.000. Ente Vasco de la Energía-EVE, Bilbao*.

Garrote-Ruiz, A.; García-Potero, J.; L., M.-J.; A., A.-G.; Eguiguren-Altuna, E. and García-Pascual, I. (**1993a**). *Mapa de la Hoja n° 37-II (Armintza) del Mapa Geológico del País Vasco a escala 1:25.000. Ente Vasco de la Energía-EVE, Bilbao*.

Garrote-Ruiz, A.; García-Potero, J.; L., M.-J.; A., A.-G.; Eguiguren-Altuna, E. and García-Pascual, I. (**1993b**). *Mapa de la Hoja n° 37-IV (Getxo) del Mapa Geológico del País Vasco a escala 1:25.000. Ente Vasco de la Energía-EVE, Bilbao*.

Gee, M. and Gawthorpe, R. (**2006**). *Submarine channels controlled by salt tectonics: Examples from 3D seismic data offshore Angola*, Marine and Petroleum Geology 23: 443 – 458, doi: https://doi.org/10.1016/j.marpetgeo.2006.01.002.

Giles, K. A. and Lawton, T. F. (**2002**). *Halokinetic sequence stratigraphy adjacent to the El Papalote diapir, northeastern Mexico*, AAPG bulletin 86: 823-840, doi: https://doi.org/10.1306/61EEDBAC-173E-11D7-8645000102C1865D.

Giles, K. A. and Rowan, M. G. (**2012**). *Concepts in halokinetic-sequence deformation and stratigraphy*, Geological Society, London, Special Publications 363: 7-31, doi: https://doi.org/10.1144/SP363.2.

Gómez, M.; Vergés, J. and Riaza, C. (**2002**). *Inversion tectonics of the northern margin of the Basque Cantabrian Basin*, Bulletin de la Société Géologique de France 173: 449-459, doi: https://doi.org/10.2113/173.5.449.

Haq, B.U. (2014). Cretaceous eustasy revisited. Glob. Planet. Chang. 113, 44-58, doi: https://doi.org/10.1016/j.gloplacha.2013.12.007.

Harrison, J. C. and Jackson, M. P. A. (**2014**). *Exposed evaporite diapirs and minibasins above a canopy in central Sverdrup Basin, Axel Heiberg Island, Arctic Canada*, Basin Res 26: 567-596, doi: https://doi.org/10.1111/bre.12037.

Hearon, T. E.; Rowan, M. G.; Lawton, T. F.; Hannah, P. T. and Giles, K. A. (**2014**). *Geology and tectonics of Neoproterozoic salt diapirs and salt sheets in the eastern Willouran Ranges, South Australia*, Basin Research: 27: 183-207, doi: https://doi.org/10.1111/bre.12067.

Hearon, T. E.; Rowan, M. G.; Giles, K. A. and Hart, W. H. (**2014**). *Halokinetic deformation adjacent to the deepwater Auger diapir, Garden Banks 470, northern Gulf of Mexico: Testing the applicability of an outcrop-based model using subsurface data*, Interpretation 2: SM57-SM76, doi: https://doi.org/10.1190/INT-2014-0053.1.

Jackson, C. (**2012**). *The initiation of submarine slope failure and the emplacement of mass transport complexes in salt-related minibasins: A three-dimensional seismic-reflection case study from the Santos Basin, offshore Brazil*, Geological Society of America Bulletin 124: 746-761, doi: https://doi.org/10.1130/B30554.1.

Jones, O. T. (**1939**). *The geology of the Colwyn Bay district: a study of submarine slumping during the Salopian period*, Quarterly Journal of the Geological Society 95: 335-382, doi: https://doi.org/10.1144/GSL.JGS.1939.065.01-04.14.

Kergaravat, C.; Ribes, C.; Legeay, E.; Callot, J.-P.; Kavak, K. S. and Ringenbach, J.-C. (**2016**). *Minibasins and salt canopy in foreland fold-and-thrust belts: The central Sivas Basin, Turkey*, Tectonics 35: 1342-1366, doi:

https://doi.org/10.1002/2016TC004186.

Kernen, R. A.; Giles, K. A.; Rowan, M. G.; Lawton, T. F. and Hearon, T. E. (**2012**). *Depositional and halokinetic-sequence stratigraphy of the Neoproterozoic Wonoka Formation adjacent to Patawarta allochthonous salt sheet, Central Flinders Ranges, South Australia*, Geological Society, London, Special Publications 363: 81-105, doi: https://doi.org/10.1144/SP363.5.

Larrasoaña, J. C.; Parés, J. M.; Millán, H.; del Valle, J. and Pueyo, E. L. (**2003**). *Paleomagnetic, structural, and stratigraphic constraints on transverse fault kinematics during basin inversion: The Pamplona Fault (Pyrenees, north Spain)*, Tectonics, 22, 1071, doi:10.1029/2002TC001446, 6.

Le Goff, J. L.; Reijmer, J.; Cerepi, A.; Loisy, C.; Swennen, R.; Heba, G.; Cavailhes, T. and Graaf, S. D. (**2019**). *The dismantling of the Apulian carbonate platform during the late Campanian – early Maastrichtian in Albania*, Cretaceous Research 96: 83 – 106, doi: https://doi.org/10.1016/j.cretres.2018.11.013.

López-Horgue, M.; Owen, H.; Aranburu, A.; Fernández-Mendiola, P. and García-Mondéjar, J. (**2009**). *Early late Albian (Cretaceous) of the central region of the Basque-Cantabrian Basin, northern Spain: biostratigraphy based on ammonites and orbitolinids*, Cretaceous Research 30: 385 – 400, doi: https://doi.org/10.1016/j.cretres.2008.08.001.

Madof, A. S.; Christie-Blick, N. and Anders, M. H. (**2009**). *Stratigraphic controls on a salt-withdrawal intraslope minibasin, north-central Green Canyon, Gulf of Mexico: Implications for misinterpreting sea level change*, AAPG bulletin 93: 535-561, doi: https://doi.org/10.1306/12220808082.

Martín-Chivelet, J.; Berástegui, X.; Rosales, I.; Vilas, L.; Vera, J.; Caus, E.; Gräfe, K.; Mas, R.; Puig, C.; Segura, M.; Robles, S.; Floquet, M.; Quesada, S.; Ruiz-Ortiz, P.; Fregenal-Martínez, M.; Salas, R.; Arias, C.; García, A.; Martín-Algarra, A.; Meléndez, M.; Chacón, B.; Molina, J.; Sanz, J.; Castro, J.; García-Hernández, M.; Carenas, B.; García-Hidalgo, J.; Gil, J. and Ortega, F., **2002**. *Cretaceous. In: The Geology of Spain. Gibbons, W. & Moreno, T. (Ed.). pp. 255–292*. Geological Society of London, London.

Martín-Martín, J. D.; Vergés, J.; Saura, E.; Moragas, M.; Messager, G.; Baqués, V.; Razin, P.; Grélaud, C.; Malaval, M.; Joussiaume, R.; Casciello, E.; Cruz-Orosa, I. and Hunt, D. W. (**2017**). *Diapiric growth within an Early Jurassic rift basin: The Tazoult salt wall (central High Atlas, Morocco)*, Tectonics 36: 2-32, doi: https://doi.org/10.1002/2016TC004300.

Martinsen, O. and Bakken, B. (**1990**). *Extensional and compressional zones in slumps and slides in the Namurian of County Clare, Ireland*, Journal of the Geological Society 147: 153-164, doi: https://doi.org/10.1144/gsjgs.147.1.0153.

Mathey, B. (**1987**). *Les Flyschs Crétacé supérieur des Pyrénées Basques: âge, anatomie, origine du matériel, milieu de dépôt et la relation avec l'ouverture du Golfe de Gascogne.*, Thèse de Doctorat d'Etat, Centre des Sciences de la Terre, Université de Bourgogne, Dijon, 403 pp.

Mayall, M.; Lonergan, L.; Bowman, A.; James, S.; Mills, K.; Primmer, T.; Pope, D.; Rogers, L. and Skeene, R. (**2010**). *The response of turbidite slope channels to growth-induced seabed topography*, AAPG Bulletin 94: 1011-1030, doi: https://doi.org/10.1306/01051009117.

Montigny, R.; Azambre, B.; Rossy, M. and Thuizat, R. (**1986**). *K-Ar Study of cretaceous magmatism and metamorphism in the pyrenees: Age and length of rotation of the Iiberian Peninsula*, Tectonophysics 129: 257 – 273, doi: https://doi.org/10.1016/0040-1951(86)90255-6.

Moscardelli, L. and Wood, L. (**2008**). *New classification system for mass transport complexes in offshore Trinidad*, Basin Research 20: 73-98, doi: https://doi.org/10.1111/j.1365-2117.2007.00340.x.

Moscardelli, L. and Wood, L. (**2016**). *Morphometry of mass-transport deposits as a predictive tool*, GSA Bulletin 128: 47-80, doi: https://doi.org/10.1130/B31221.1.

Mulder, T. and Cochonat, P. (**1996**). *Classification of offshore mass movements*, Journal of Sedimentary Research 66: 43-57, doi: https://doi.org/10.1306/D42682AC-2B26-11D7-8648000102C1865D.

Ogata, K.; Pogačnik, Ž.; Pini, G.; Tunis, G.; Festa, A.; Camerlenghi, A. and Rebesco, M. (**2014**). *The carbonate mass transport deposits of the Paleogene Friuli Basin (Italy/Slovenia): Internal anatomy and inferred genetic processes*, Marine Geology 356: 88 – 110, doi: https://doi.org/10.1016/j.margeo.2014.06.014.

Oluboyo, A. P.; Gawthorpe, R. L.; Bakke, K. and Hadler-Jacobsen, F. (**2014**). *Salt tectonic controls on deep-water turbidite depositional systems: Miocene, southwestern Lower Congo Basin, offshore Angola*, Basin Research 26: 597-620, doi: https://doi.org/10.1111/bre.12051.

Omosanya, K. O. and Alves, T. M. (**2013**). *Ramps and flats of mass-transport deposits (MTDs) as markers of seafloor strain on the flanks of rising diapirs (Espírito Santo Basin, SE Brazil)*, Marine Geology 340: 82 – 97, doi: https://doi.org/10.1016/j.margeo.2013.04.013.

Payros, A.; Orue-Etxebarria, X. and Pujalte, V. (**2006**). *Covarying sedimentary and biotic fluctuations in Lower–Middle Eocene Pyrenean deep-sea deposits: Palaeoenvironmental implications*, Palaeogeography, Palaeoclimatology, Palaeoecology

234: 258 – 276, doi: https://doi.org/10.1016/j.palaeo.2005.10.013.

Pedrera, A.; García-Senz, J.; Ayala, C.; Ruiz-Constán, A.; Rodríguez-Fernández, L. R.; Robador, A. and González Menéndez, L. (**2017**). *Reconstruction of the Exhumed Mantle Across the North Iberian Margin by Crustal-Scale 3-D Gravity Inversion and Geological Cross Section*, Tectonics 36: 3155-3177, doi: https://doi.org/10.1002/2017TC004716.

Poprawski, Y.; Basile, C.; Agirrezabala, L. M.; Jaillard, E.; Gaudin, M. and Jacquin, T. (**2014**). *Sedimentary and structural record of the Albian growth of the Bakio salt diapir (the Basque Country, northern Spain)*, Basin Research 26: 746-766, doi: https://doi.org/10.1111/bre.12062.

Poprawski, Y.; Basile, C.; Jaillard, E.; Gaudin, M.; Lopez, M. (2016). Halokinetic sequences in carbonate systems: An example from the Middle Albian Bakio Breccias Formation (Basque Country, Spain), Sedimentary Geology 334: 34-52,doi: https://doi.org/10.1016/j.sedgeo.2016.01.013.

Puelles, P.; Ábalos, B.; García de Madinabeitia, S.; Sánchez-Lorda, M.; Fernández-Armas, S. and Gil Ibarguchi, J. (**2014**). *Provenance of quartz-rich metamorphic tectonite pebbles from the "Black Flysch" (W Pyrenees, N Spain): An EBSD and detrital zircon LA–ICP-MS study*, Tectonophysics 632: 123 – 137, doi: https://doi.org/10.1016/j.tecto.2014.06.004.

Pujalte, V.; Baceta, J. I. and Schmitz, B. (**2015**). *A massive input of coarse-grained siliciclastics in the Pyrenean Basin during the PETM: the missing ingredient in a coeval abrupt change in hydrological regime*, Climate of the Past, 11, 1653–1672, doi: https://doi.org/10.5194/cp-11-1653-2015.

Pujalte, V.; Robles, S. and Garcia-Mondéjar, J. (**1986**). *Caracteristicas sedimentológicas y paleogeográficas del fan-delta albiense de la Formación Monte Grande y sus relaciones con el Flysh Negro (Arminza-Górliz, Vizcaya)*, Acta geológica hispánica 21: 141-150.

Rat, P. (**1988**). *The Basque-Cantabrian basin between the Iberian and European plates: Some facts but still many problems*, Revista de la Sociedad Geológica de España 1: 327-348.

Robles, S.; Garrote, A. and García-Mondéjar, J. (**1989**). *XII Congreso Español de Sedimentología: Simposios y conferencias.*, Universidad del País Vasco. Departamento de Estratigrafía, Geodinámica y Paleontología, Bilbao. .

Robles, S.; Pujalte, V. and Garcia-Mondéjar, J. (**1988**). *Evolución de los sistemas sedimentarios del Margen continental Cantábrico durante el Albiense y Cenomaniense,*

en la transversal del litoral vizcaino, Revista de la Sociedad Geológica, Márgenes continentales de la Peninsula Ibérica 1: 3-4.

Roca, E.; Muñoz, J. A.; Ferrer, O. and Ellouz, N. (**2011**). *The role of the Bay of Biscay Mesozoic extensional structure in the configuration of the Pyrenean orogen: Constraints from the MARCONI deep seismic reflection survey*, Tectonics 30, TC2001, doi: doi:10.1029/2010TC002735.

Roca, E., Ferrer, O., Rowan, M.G., Muñoz, J.A., Butillé, M., Giles, K.A., Arbués, P., de Matteis, M. (2020). Salt tectonics and controls on halokinetic-sequence development of an exposed deepwater diapir: The Bakio Diapir, Basque-Cantabrian Basin, Pyrenees, Marine and Petroleum Geology, doi: https://doi.org/10.1016/j.marpetgeo.2020.104770.

Rowan, M.G. (2014). Passive-margin salt basins: hyperextension, evaporite deposition, and salt tectonics. Basin Res, 26: 154-182. https://doi.org/10.1111/bre.12043

Rowan, M.; Giles, K.; Roca, E.; Arbues, P. and Ferrer, O. (**2012**). *Analysis of Growth Strata Adjacent to an Exposed Deepwater Salt Diapir, northern Spain*, American Association of Petroleum Geologists Annual Convention, Long Beach, USA.

Saura, E.; Ardèvol i Oró, L.; Teixell, A. and Vergés, J. (**2016**). *Rising and falling diapirs, shifting depocenters, and flap overturning in the Cretaceous Sopeira and Sant Gervàs subbasins (Ribagorça Basin, southern Pyrenees)*, Tectonics 35: 638-662, doi: https://doi.org/10.1002/2015TC004001.

Serrano, A. and Martínez del Olmo, W. (**1990**). *Tectónica salina en el Dominio Cántabro-Navarro: evolución, edad y origen de las estructuras salinas*, Formaciones evaporíticas de la Cuenca del Ebro y cadenas periféricas, y de la zona de Levante: Empresa Nacional de Residuos Radioactivos Sociedad Anónima and Universitat de Barcelona: 39-53.

Sharman, G. R.; Graham, S. A.; Masalimova, L. U.; Shumaker, L. E. and King, P. R. (**2015**). *Spatial patterns of deformation and paleoslope estimation within the marginal and central portions of a basin-floor mass-transport deposit, Taranaki Basin, New Zealand*, Geosphere 11: 266-306, doi: https://doi.org/10.1130/GES01126.1.

Sobiesiak, M. S.; Kneller, B.; Alsop, G. I. and Milana, J. P. (**2016**). *Internal deformation and kinematic indicators within a tripartite mass transport deposit, NW Argentina*, Sedimentary Geology 344: 364 – 381, doi: https://doi.org/10.1016/j.sedgeo.2016.04.006.

Sobiesiak, M. S.; Kneller, B.; Alsop, G. I. and Milana, J. P. (**2018**). *Styles of basal interaction beneath mass transport deposits*, Marine and Petroleum Geology 98: 629 – 639, doi: https://doi.org/10.1016/j.marpetgeo.2018.08.028.

Soutter, E. L.; Kane, I. A.; Fuhrmann, A.; Cumberpatch, Z. A. and Huuse, M. (**2019**). *The stratigraphic evolution of onlap in siliciclastic deep-water systems: Autogenic modulation of allogenic signals*, Journal of Sedimentary Research 89: 890-917, doi: https://doi.org/10.2110/jsr.2019.49.

Strachan L. J. (2008). *Flow transformations in slumps: a case study from the Waitemata Basin, New Zealand*, Sedimentology 55: 1311-1332, doi: https://doi.org/10.1111/j.1365-3091.2007.00947.x.

Strachan, L. and Alsop, G. I. (**2006**). *Slump folds as estimators of palaeoslope: a case study from the Fisherstreet Slump of County Clare, Ireland*, Basin Research 18: 451-470, doi: https://doi.org/10.1111/j.1365-2117.2006.00302.x.

Tripsanas, E. K.; Bryant, W. R. and Phaneuf, B. A. (**2004**). *Slope-instability processes caused by salt movements in a complex deep-water environment, Bryant Canyon area, northwest Gulf of Mexico*, AAPG Bulletin 88: 801-823, doi: https://doi.org/10.1306/01260403106.

Tugend, J.; Manatschal, G.; Kusznir, N. J.; Masini, E.; Mohn, G. and Thinon, I. (**2014**). *Formation and deformation of hyperextended rift systems: Insights from rift domain mapping in the Bay of Biscay-Pyrenees*, Tectonics 33: 1239-1276, doi: https://doi.org/10.1002/2014TC003529.

Ubide, T.; Wijbrans, J. R.; Galé, C.; Arranz, E.; Lago, M. and Larrea, P. (**2014**). *Age of the Cretaceous alkaline magmatism in northeast Iberia: Implications for the Alpine cycle in the Pyrenees*, Tectonics 33: 1444-1460, doi: https://doi.org/10.1002/2013TC003511.

Vergés, J.; Fernández, M. and Martínez, A. (**2002**). *The Pyrenean orogen: pre-, syn-, and post-collisional evolution*, In: Rosenbaum, G. and Lister, G.S. Reconstruction of the evolution of the Alpine-Himalayan Orogen. Journal of the Virtual Explorer 8: 55 – 74, doi: https://doi.org/10.3809/jvirtex.2002.00058.

Vergés, J.; Poprawski, Y.; Almar, Y.; Drzewiecki, P. A.; Moragas, M.; Bover-Arnal, T.; Macchiavelli, C.; Wright, W.; Messager, G.; Embry, J.-C. and Hunt, D. (2020). *Tectono-sedimentary evolution of Jurassic–Cretaceous diapiric structures: Miravete anticline, Maestrat Basin, Spain*, Basin Research 32: 1653– 1684, doi: https://doi.org/10.1111/bre.12447

Vicente Bravo, J. and Robles, S. (**1991a**). *Caracterización de las facies de la transición canal-lóbulo en la secuencia Jata del Flysch Negro (Albiense Superior norte de Vizcaya)*, Geogaceta 10: 72-75.

Vicente-Bravo, J. and Robles, S. (**1991b**). *Geometría y modelo deposicional de la*

secuencia Sollube del Flysch Negro (Albiense medio, norte de Bizkaia), Geogaceta 10: 69-72.

Vicente Bravo, J. and Robles, S. (**1995**). *Large-scale mesotopographic bedforms from the Albian Black Flysch, northern Spain: characterization, setting and comparison with recent analogues. In: Pickering K.T., Hiscott R.N., Kenyon N.H., Ricci Lucchi F., Smith R.D.A. (eds) Atlas of Deep Water Environments. Springer, Dordrecht,* 216-226, doi: https://doi.org/10.1007/978-94-011-1234-5_32

Ward, N. I. P.; Alves, T. M. and Blenkinsop, T. G. (**2018**). *Submarine sediment routing over a blocky mass-transport deposit in the Espírito Santo Basin, SE Brazil*, Basin Research 30: 816-834; doi: https://doi.org/10.1111/bre.12282.

WOODCOCK, N. H. (**1976**). *Structural style in slump sheets: Ludlow Series, Powys, Wales*, Journal of the Geological Society 132: 399-415, doi: https://doi.org/10.1144/gsjgs.132.4.0399.

WOODCOCK, N. H. (**1979**). *The use of slump structures as palaeoslope orientation estimators*, Sedimentology 26: 83-99, doi: https://doi.org/10.1111/j.1365-3091.1979.tb00339.x.

Wu, N.; Jackson, C. A.; Johnson, H. and Hodgson, D. M. (**2019**). *Lithological, petrophysical and seal properties of mass-transport complexes (MTCs), northern Gulf of Mexico.*, https://doi.org/10.31223/osf.io/hcdj6

Wu, N.; Jackson, C. A.-L.; Johnson, H. D.; Hodgson, D. M. and Nugraha, H. D. (**2020**). *Mass-transport complexes (MTCs) document subsidence patterns in a northern Gulf of Mexico salt minibasin*, Basin Research 32: 1300– 1327, doi: https://doi.org/10.1111/bre.12429.

Figure 1: Geological map of the Basque-Cantabrian basin, slightly modified from Ábalos (2016). Wells used for the building of the structural cross-section and wells in the study area are shown. The extent of Figure 2 is shown by the dashed black line, and the study area (Figure 3) is shown in the black box.

Figure 2: Balanced structural cross-section of the Basque-Cantabrian basin at present-day and restored for the Early Cenomanian, slightly modified from Pedrera et al., (2017). The initial colors published in Pedrera et al., (2017) were changed to be homogeneous with the colors of Figure 1. The study area is shown, projected onto the cross-section.

Figure 3: Geological map of the study area including the coastline from Mundaka to Plentzia. This geological map was constructed using the stratigraphic and tectonic contacts drawn in the maps of the “Instituto Geológico y Minero de España” (Espejo, 1973 ; Espejo and Pastor. 1973), “Ente Vasco de la Energía” (Garrote-Ruiz et al., 1991, 1992, 1993a & b) and Poprawski et al. (2014) and Ábalos (2016). Offshore geological interpretations with bed traces are those proposed in Roca et al. (2020), using high resolution bathymetric data. The black labels show the location of the MTD1 to MTD7. The grey lines a to e show the location of the stratigraphic columns presented in figure 4. Labels S2 to S3 indicate the location of important erosional surfaces and angular unconformities described in figure 4. Rose-diagrams indicate the directions of regionally derived turbidity currents from the Black Flysch Group, obtained from sole marks and scour orientations. Rose-diagram a. has been built using data from Robles (1989) and Agirrezabala (2015), the rose-diagram b. using data from Robles (1989) and the rose-diagrams c. using data from Cumberpatch et al. (2021). Highest frequencyclass in the rose diagrams corresponds to 12 measurement and the smallest to 1 measurement.

Figure 4: Stratigraphy of the Jata and Burgoa minibasins. a. The stratigraphic columns are modified from Agirrezabala (2015) and Agirrezabala et al. (2017) (column a), from

Robles et al., (1988) (columns b, c, d and f), from Poprawski et al., (2014) (column e). Distances between the stratigraphic columns are not at scale. The black labels MTD1 to MTD7 show the location of the mass-transport deposits studied in this paper. Labels S1 to S3 indicate the location of important erosional surfaces and angular unconformities. S1, S2 and S3 are described in Robles et al. (1988), Agirrezabala (2015) and Agirrezabala et al. (2017), S2 is described in Robles et al. (1988) and Poprawski et al. (2014 ; 2016). The correlations between the stratigraphic columns are mainly based on lithostratigraphic relationships, with some scarce biostratigraphic constrains (numbers from 1 to 9). Number 1 to 9 indicate biostratigraphic data described in the literature and summarized in table 1. b. Correlations from Amrintza to the coastline between Armintza and Bakio following the offshore bed traces of Roca et al. (2020) and showing the lateral extension of the Middle and Late Albian boundary, inferred by López-Horgue et al. (2009).

Figure 5: Methods used for the mass failure transport sense reconstruction and for the estimation of the amount of clasts and reworked beds (versus matrix) for the MTDs in this study. a. Example of symmetric folds formed in layer parallel shear and theoretical distribution of axial planes and folds axes in an equal area stereograph modified from Bradley and Hanson (1998). b. Example of sheath folds formed in layer normal shear and theoretical distribution of axial planes and folds axes in an equal area stereograph modified from Bradley and Hanson (1998). c. Raw field photograph of the MTD5 (see fig. 3 for its location). d. The same field photograph of the MTD5, where polygons for the clasts and reworked beds and for the matrix were drawn using vectorial drawing software. The number of pixels representing the clasts, reworked beds and matrix are

then used to estimate the percent of matrix versus clast and reworked beds for each MTD.

Figure 6: Field photographs and stereonets for MTD1 localized along the coastline, north of Bermeo. a. Overview of the MTD1 showing imbricate thrusts developed in redeposited carbonates including limestones blocks. b. Detailed view of the limestone blocks embedded within the MTD1 located on an outcrop located further East compared to Fig. 6a. c. Detailed view of clasts including corals within the MTD1. d. Detailed view of imbricate thrusts affecting mud-supported breccias with limestones blocks, located on an outcrop located further East compared to Fig. 6a. e. Detailed view of recumbent fold developed in fine-grained calcarenites and marls. f. Stereonet showing folds axes (blue points) and poles of the axial planes (red squares) after restoration (S0 used for the restoration: N70°,70°N). The best axis (fold axes) is shown by the blue star, the best plane (axial planes) by the red circle and the orange plane is the best plane calculated on the thrust population dataset. The black great circle is calculated based on the pole of the planes and is used to assume the transport direction for the AIM. Number of data: 13 axial planes and 14 fold axes. g. Stereonet showing the poles and planes of the syn-sedimentary thrusts found in the MTD1, after restoration (S0 used for the restoration: N100°,45°N). Number of data: 16 (fault planes). The black great circle is calculated based on the pole of the planes and is used to assume the transport direction for the GFPM-N.

Figure 7: Field photographs and stereonets for MTD2 localized along the coastline, at

the toe of the Gaztelugatxe scarp (Poprawski et al., 2014) northeast of Bakio. a. Overview of MTD2 made of a basal carbonate debrite and of an upper part with folded turbidite sandstones embedded in a muddy matrix including limestones debris. b. Detailed view of a sheath fold showing clockwise and an anticlockwise rotation of the hinge in the lateral fold terminations. c. Detailed view of an asymmetric folds verging eastward and suggesting an apparent transport direction toward the east. d. Details of the carbonate clasts found within the MTD2, showing here a bivalve shell. e. Stereonet showing folds axes (blue points) and the pole of the axial planes (red squares) after restoration (S0 used for the restoration: N15°,35°E for the outcrops West of the stairs going to the Gaztelugatxe hermitage and N15°,55°E for the outcrops West of the same stairs). The best axis (fold axes) is shown by the blue star and the best plane (axial planes) by the red circle. The black great circle is calculated based on the pole of the planes and is used to assume the transport direction for the AIM. Number of data: 41 axial planes and 63 fold axes.

Figure 8: Field photographs and stereonets for MTD3 localized along the coastline, northwest of Bermeo. a. Overview of MTD3 showing folded coarse-grained and medium-bedded turbidite beds embedded in a muddy matrix. b. Detailed view of asymmetric folds apparently verging westward. c. Detailed view of an asymmetric open fold apparently verging southward, transported along a syn-sedimentary thrust. d. Stereonet showing folds axes (blue points) and the pole of the axial planes (red squares) after restoration (S0 used for the restoration: N78°,42°N). The best axis (fold axes) is shown by the blue star and the best plane (axial planes) by the red circle. The black great circle

is calculated based on the pole of the planes and is used to assume the transport direction for the AIM. Number of data: 20 axial planes and 20 fold axes.

Figure 9: Field photographs and stereonets for MTD4 localized along the coastline, on the cliffs of the Matxitxako Cape. a. Overview of MTD4 made of thin- to medium bedded fine-to coarse-grained sandy turbidites interbedded with mudstones. b. Detailed view of tight recumbent and sheath folds apparent verging toward the southwest and associated with thrusts and back-thrusts. c. Clasts with C-S structures or sigmoid geometries, indicating an apparent transport toward the southwest. d. Detailed view of carbonate clasts in the coarse-grained turbidite facies above the MTD4. e. Stereonet showing folds axes (blue points) and the pole of the axial planes (red squares) after restoration (S0 used for the restoration: N112°,10°N). The best axis (fold axes) is shown by the blue star and the best plane (axial planes) by the red circle. The black great circle is calculated based on the pole of the planes and is used to assume the transport direction for the AIM. Number of data: 18 axial planes and 18 fold axes.

Figure 10: Field photographs and stereonets for MTD5 localized along the coastline, at 1,5 km west of Bakio. a. Overview of MTD5 that consists of folded layers of thin-bedded fine-grained turbidite beds disconnected and embedded in a muddy matrix with quartz gravels and pebbles. b., c., d. Detailed views of the folded layers of thin-bedded fine-grained turbidite beds and of the quartz gravels and pebbles. e. Stereonet showing folds axes (blue points) and the pole of the axial planes (red squares) after restoration (S0 used for the restoration: N110°,15°S). The best axis (fold axes) is shown by the blue star

and the best plane (axial planes) by the red circle. The black great circle is calculated based on the pole of the planes and is used to assume the transport direction for the AIM. Number of data: 30 axial planes and 30 fold axes.

Figure 11: Field photographs and stereonets for MTD6 localized along the coastline, at 3,5 km west of Bakio. a. Overview of MTD6 that consists of folded thin- and medium-bedded fine- and coarse-grained turbidites and siderite beds within a muddy matrix. b., c. Detailed views of rootless folded layers. d. Slump fold affecting laminae with siderite levels. e. Stereonet showing folds axes (blue points) and the pole of the axial planes (red squares) after restoration (S0 used for the restoration: N00°,25°W). The best axis (fold axes) is shown by the blue star and the best plane (axial planes) by the red circle. The black great circle is calculated based on the pole of the planes and is used to assume the transport direction for the AIM. Number of data: 16 axial planes and 16 fold axes.

Figure 12: Field photographs and stereonets for MTD7 localized along the coastline, on the cliffs of the Armintza harbor. a Overview of MTD7, localized above a basaltic lava flow with pillows basalts in the central cliff of the Armintza harbor. b. Overview of the MTD7, made of reworked medium-bedded coarse-grained turbidites and mudstones with facies similar to the underlying interval. c. Detailed view of one downward facing fold (here, possibly a synformal anticline) verging westward and truncated by faults. d. Stereonet showing folds axes (blue points) and the pole of the axial planes (red squares) after restoration (S0 used for the restoration: N80°,30°S). The best axis (fold axes) is shown by the blue star and the best plane (axial planes) by the red circle. The black

great circle is calculated based on the pole of the planes and is used to assume the transport direction for the AIM. Number of data: 31 axial planes and 108 fold axes.

Figure 13: Field photographs and stereonets of the minor synsedimentary structures localized stratigraphicially above MTD7 in the Armintza harbor and of the lateral equivalent of MTD7, west of Bakio. a. b. Detailed view of small structures located in the first bed covering MTD7 showing normal faults developed upslope and thrust sheets developed downslope. c Stereonet showing the planes and poles of the thrusts that are dipping eastward after restoration (S0 used for the restoration: N80°,30°S). Number of data: 7 (faults planes). d. Overview of the outcrop of the MTD7, located west of Bakio showing an basal part with debrite facies and upper part dominated by slump folds.

Figure 14: Field photographs and stereonets for other additional MTDs from the study area. a. Detailed view of a minor MTD (MTDa, in figure 3) that consists of imbricate thrust sheet, located in the western part of the Armintza harbour. b. Stereonet showing the planes and poles of the thrusts that are dipping eastward after restoration (S0 used for the restoration: N72°,60°S). Number of data: 5 (faults planes). c. and d. Field photographs of MTDs b and c exposed along the new road from Bakio to Bermeo (see fig 3 for their location).

Figure 15: a. Conceptual 3D block showing the palaeogeography of the study area based on simplified lithostratigraphic columns and taking into account interpretations from Roca et al. (2020) from the Jata and Burgoa minibasins. b. Conceptual palaeogeographic map showing the location and the axis of the minibasins, palaeo-highs and the possible spatial extension of MTDs. The exact location of the present-day

outcrops for each MTD is shown on figure 3. Black labels correspond to the different MTDs and arrows indicate their possible transport sense, inferred with the different methods used in this paper. The number of structural data used for the transport sense reconstruction is also indicated. Rose-diagrams indicate regionally derived turbidity currents of the Black Flysch Group obtained from sole marks and scour orientations. Rose-diagram a. has been built using data from Robles (1989) and Agirrezabala (2015), the rose-diagram b. using data from Robles (1989) and the rose-diagrams c. using data from Cumberpatch et al. (2021). Highest frequency class in the rose diagrams corresponds to 12 measurement and the smallest to 1 measurement.

Figure 16: Conceptual model for locally-derived MTDs in salt-controlled basins. a. Locally-derived siliciclastic MTD in deep-water environment without along slope interaction with coarse-grained facies (mud-rich MTDs). b. Locally-derived siliciclastic MTD in deep-water environment with along slope interaction with coarse-grained facies (sand-rich MTDs). c. Locally-derived carbonate-dominated MTD linked with syn-kinetmatic carbonate platform growth in the photic zone at the apex of diapirs (carbonate-dominated MTDs).

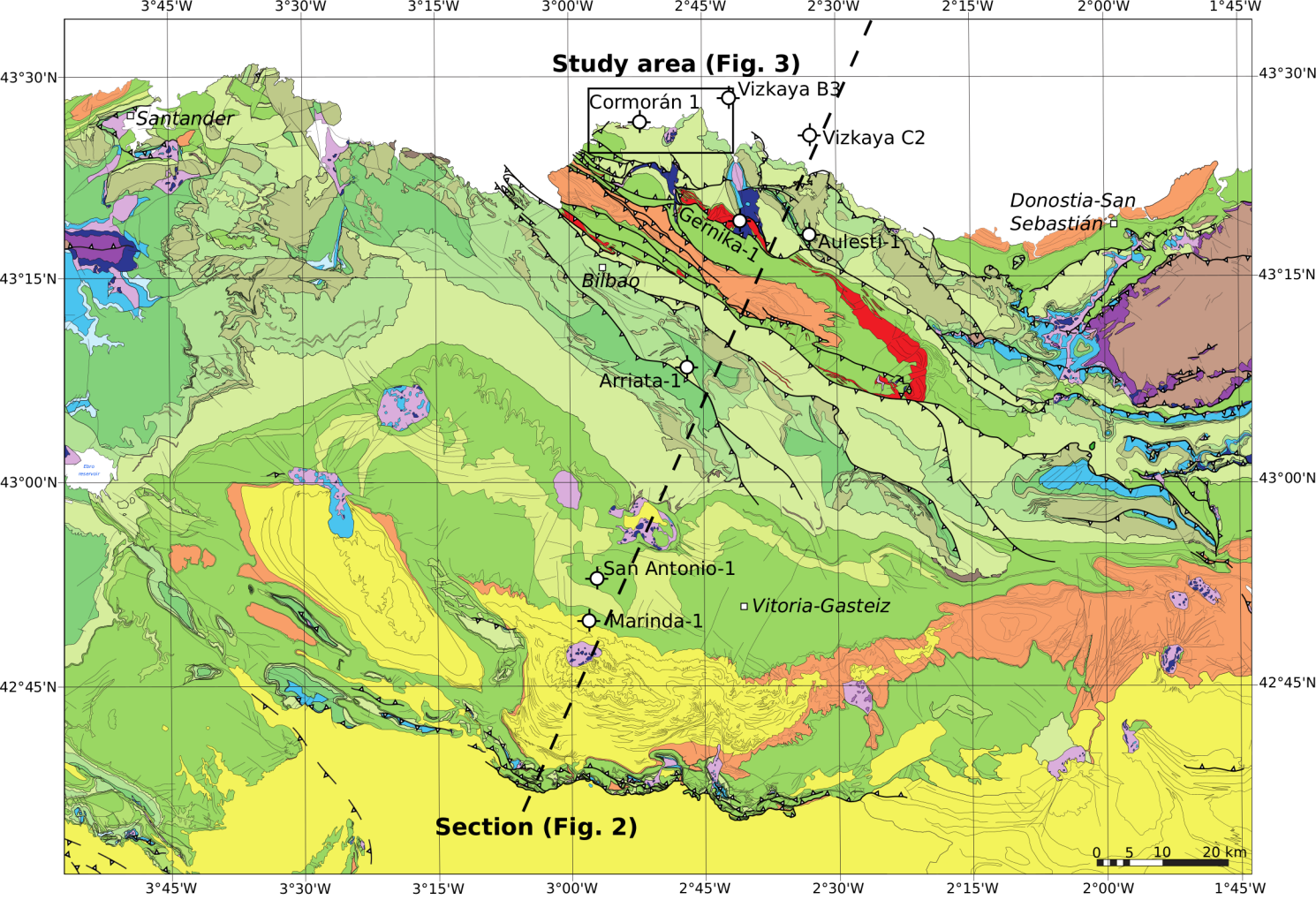

Tertiary
- Syn- to post-collision continental Rupelian to Tortonian deposits
- Marine pre-collision Danian to Lutetian deposits

Late Cretaceous
- Cenomanian to Maastrichtian marine deposits
- Magmatic rocks
- Subijana limestone (Coniacian)
- Gárate limestone (Turonian)

Late Albian-Early Cenomanian
- Fuvial (Utrillas Fm.), shallow marine (Valmaseda Fm.) and deep-marine (Black Flysch Group) deposits
- Magmatic rocks
- Limestones with Urgonian facies

Aptian to Middle Albian
- Basinal marly deposits
- Limestones with Urgonian facies

Purbeck-Weald Complex
- Weald facies sequence (Valanginian-Barremian)
- Purbeck facies sequence (Kimmeridgian-Valanginian
- Marine Jurassic

Keuper (salt)
- Salt-bearing red clay
- Dolerites (ophites)

Pre-salt rocks
- Permian-Buntsandstein
- Basement

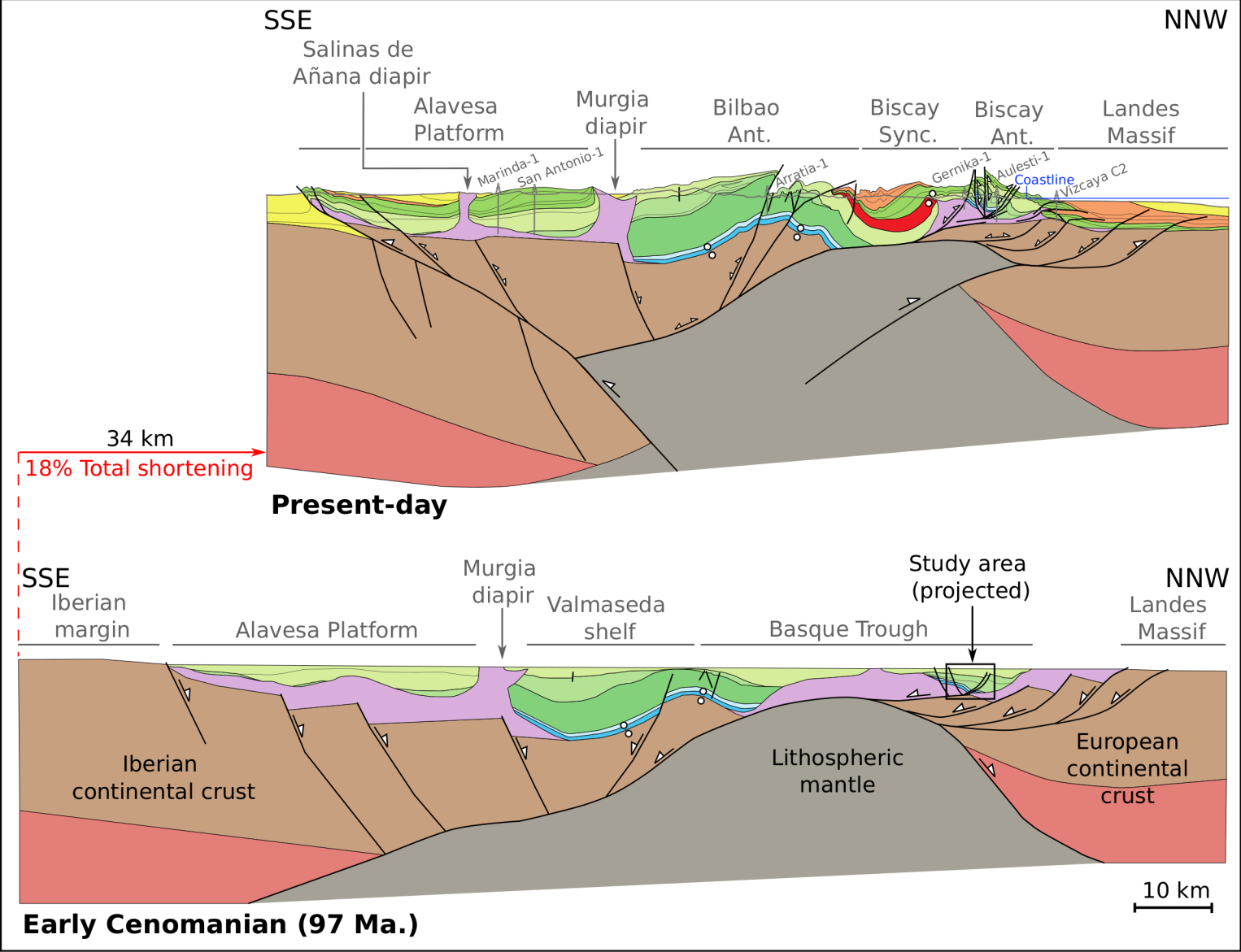
SSE
NNW
Salinas de Añana diapir
Alavesa Platform
Murgia diapir
Bilbao Ant.
Biscay Sync.
Biscay Ant.
Landes Massif
Marinda-1
San Antonio-1
Arratia-1
Gernika-1
Aulesti-1
Coastline
Vizcaya C2
34 km
18% Total shortening
Present-day
SSE
Iberian margin
Alavesa Platform
Murgia diapir
Valmaseda shelf
Basque Trough
Study area (projected)
NNW
Landes Massif
Iberian continental crust
Lithospheric mantle
European continental crust
10 km
Early Cenomanian (97 Ma.)

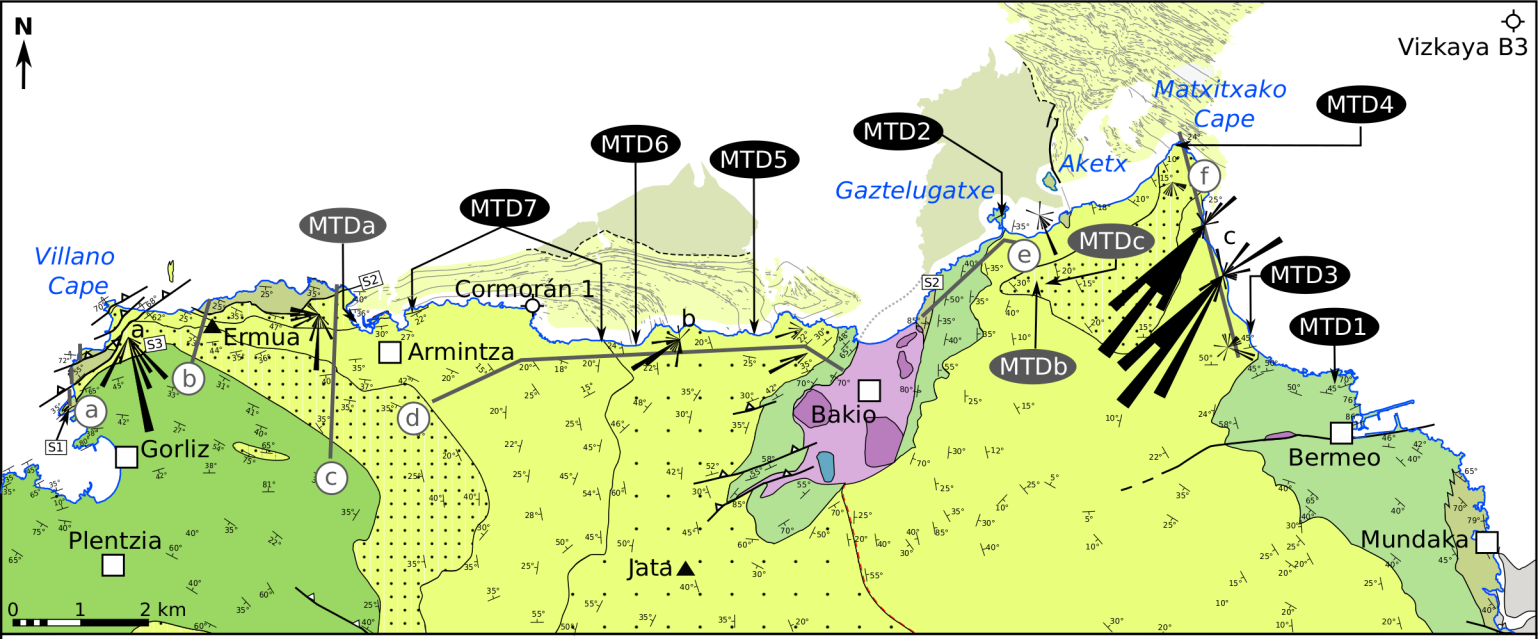

Late Cretaceous

Middle Cenomanian to Santonian thin-bedded fine-grained calcarenites interbedded with mudstones

Black Flysch Group (early Middle Albian - Lower Cenomanian)

Unit 3 : amalgamated, thick-bedded, coarse-grained turbidite sandstones interbedded with rare and thin mudstones intervals.

Unit 2: thin-bedded, fine-grained turbidite sandstones interbedded with mudstones and siderite beds

Unit 1: fine- and coarse-grained turbidite sandstones, slumps, mud- and clast-supported conglomerates and breccias interbedded with mudstones and siderite beds.

Black flysch facies currently offshore, inferred by Roca et al. (2020) using high resolution bathymetric data.

Magmatic rocks interbedded in the Black Flysch Group (Errigoiti Fm. in Castañares et al., 2001)

Aptian to Middle Albian carbonates

Redeposited carbonates and marls, Early to Middle Albian

Limestones with Urgonian facies associated with siliciclastic fan-delta deposits, Lower Albian.

Limestones with Urgonian facies and possibly carbonate breccias currently offshore, inferred by Roca et al. (2020) using high resolution bathymetric data.

Keuper

Salt-bearing red clay

Dolerites (ophites)

Dolomites and carbonates (Garrote-Ruiz et al., 1991)

Thrusts and undifferentiated faults

Possible unconformity of Unit 2 overlying the basal part of Unit 1

Current offshore extension of Bakio salt wall according to Roca et al. (2020)

towns ▲ mounts

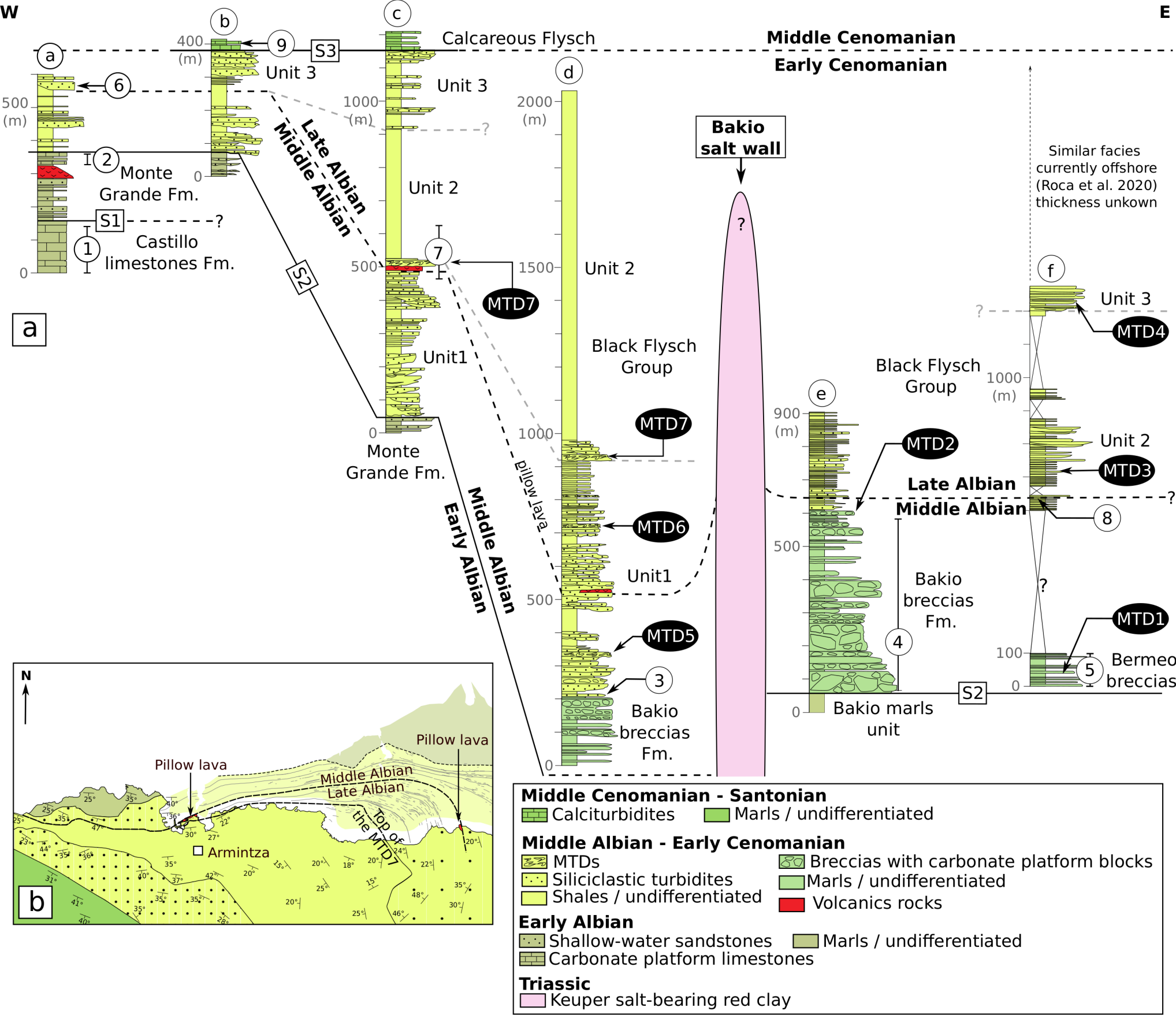
W
E
a
b
c
d
e
f
Middle Cenomanian
Early Cenomanian
Calcareous Flysch
Unit 3
Unit 2
Unit1
Monte Grande Fm.
Castillo limestones Fm.
Late Albian
Middle Albian
Early Albian
S1
S2
S3
Bakio salt wall
Similar facies currently offshore (Roca et al. 2020) thickness unkown
Black Flysch Group
pillow lava
MTD1
MTD2
MTD3
MTD4
MTD5
MTD6
MTD7
Bakio breccias Fm.
Bakio marls unit
Bermeo breccias
Pillow lava
Armintza
Top of the MTD7
N
Middle Cenomanian - Santonian
Calciturbidites
Marls / undifferentiated
Middle Albian - Early Cenomanian
MTDs
Siliciclastic turbidites
Shales / undifferentiated
Breccias with carbonate platform blocks
Marls / undifferentiated
Volcanics rocks
Early Albian
Shallow-water sandstones
Carbonate platform limestones
Marls / undifferentiated
Triassic
Keuper salt-bearing red clay

a

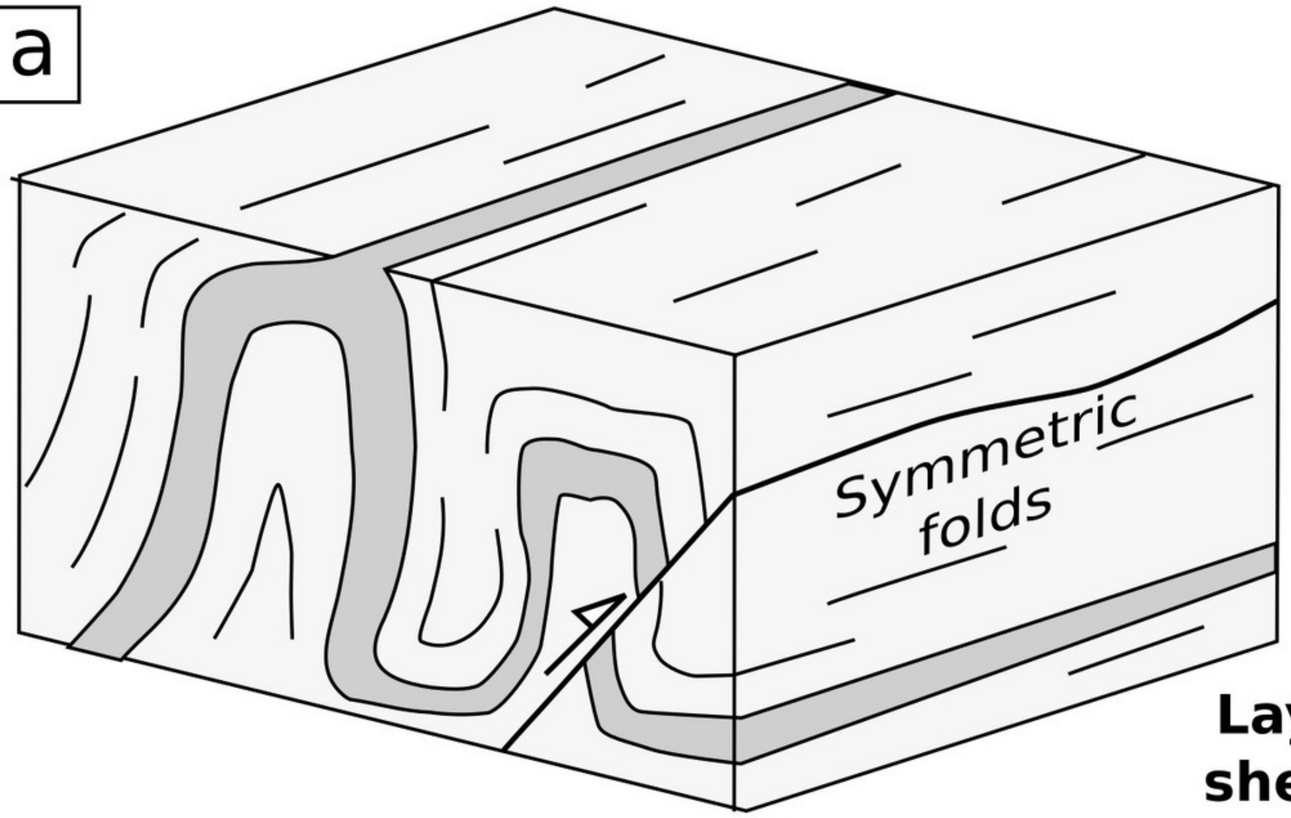

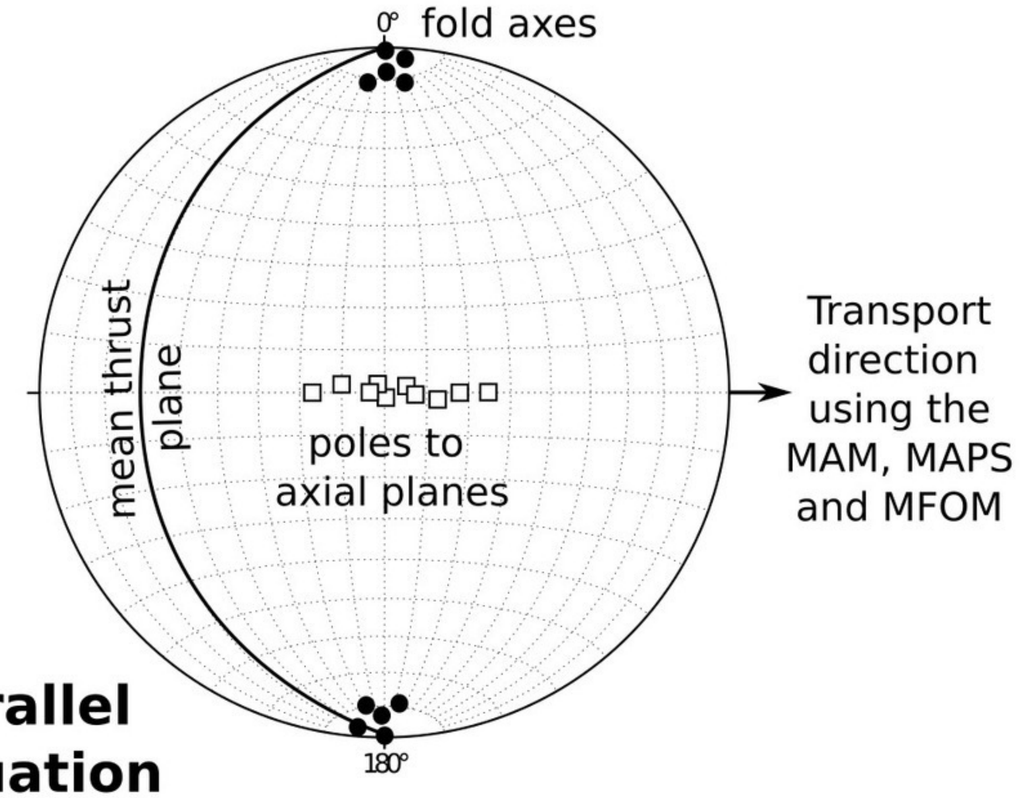

Layer parallel shear situation

b

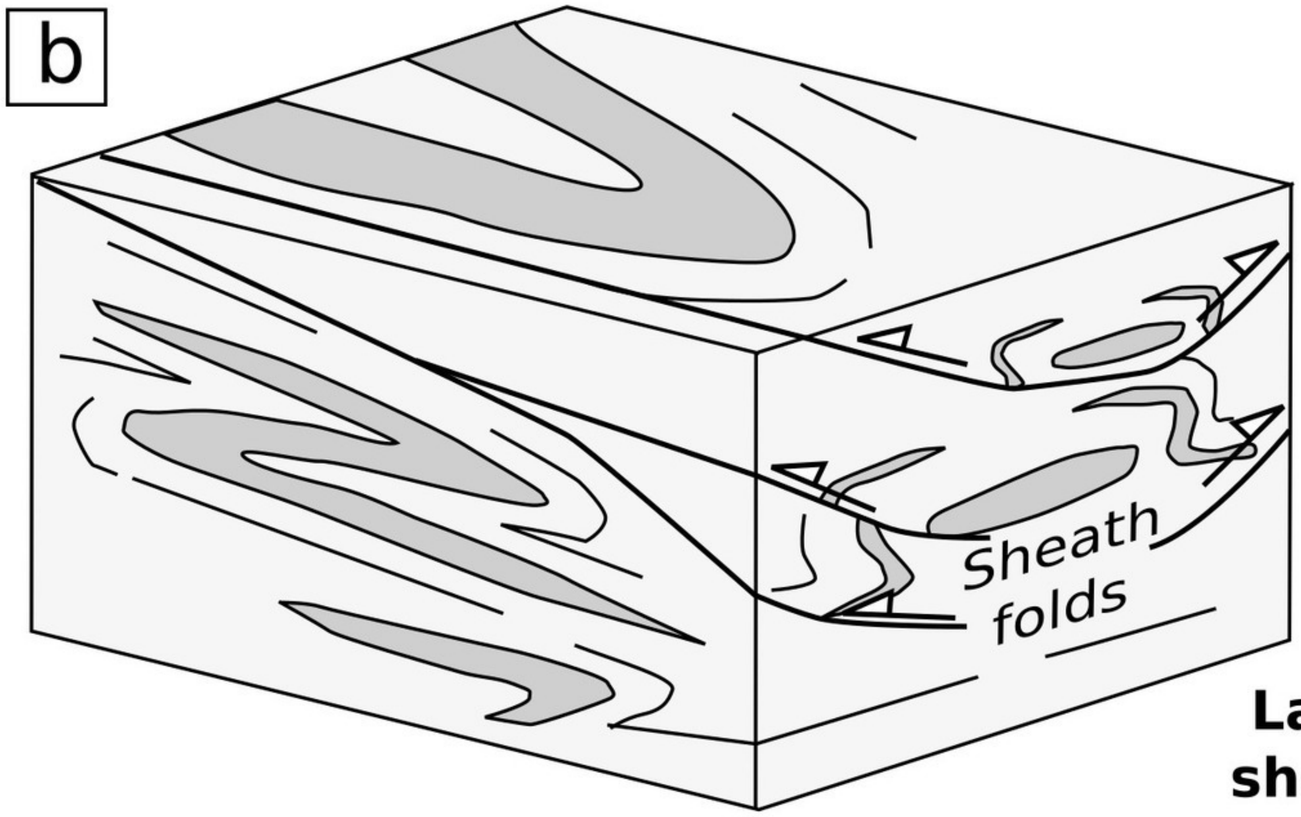

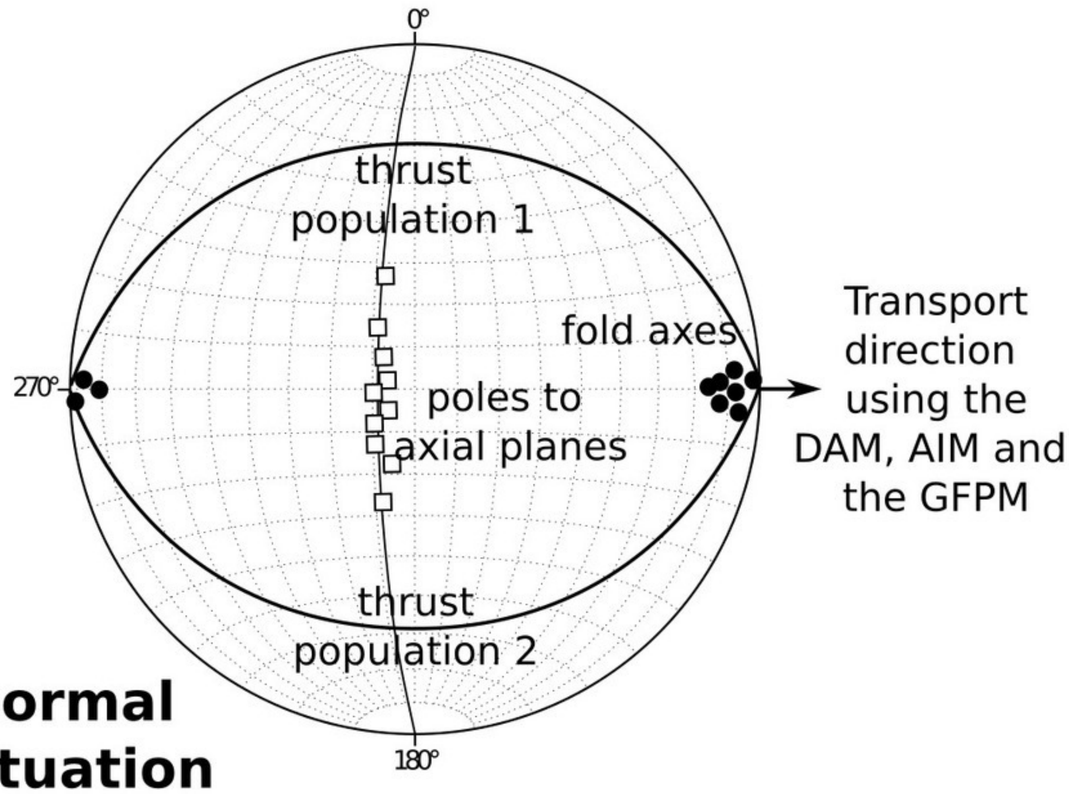

Layer normal shear situation

Matrix and clasts
digitalization
for % estimation

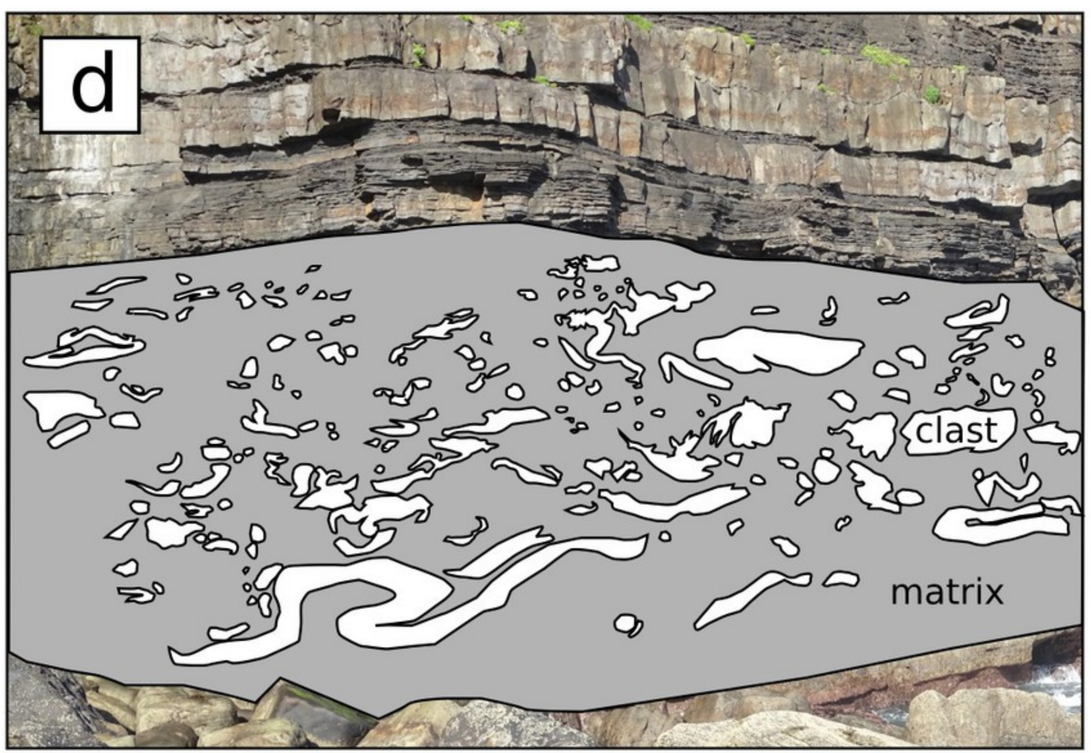

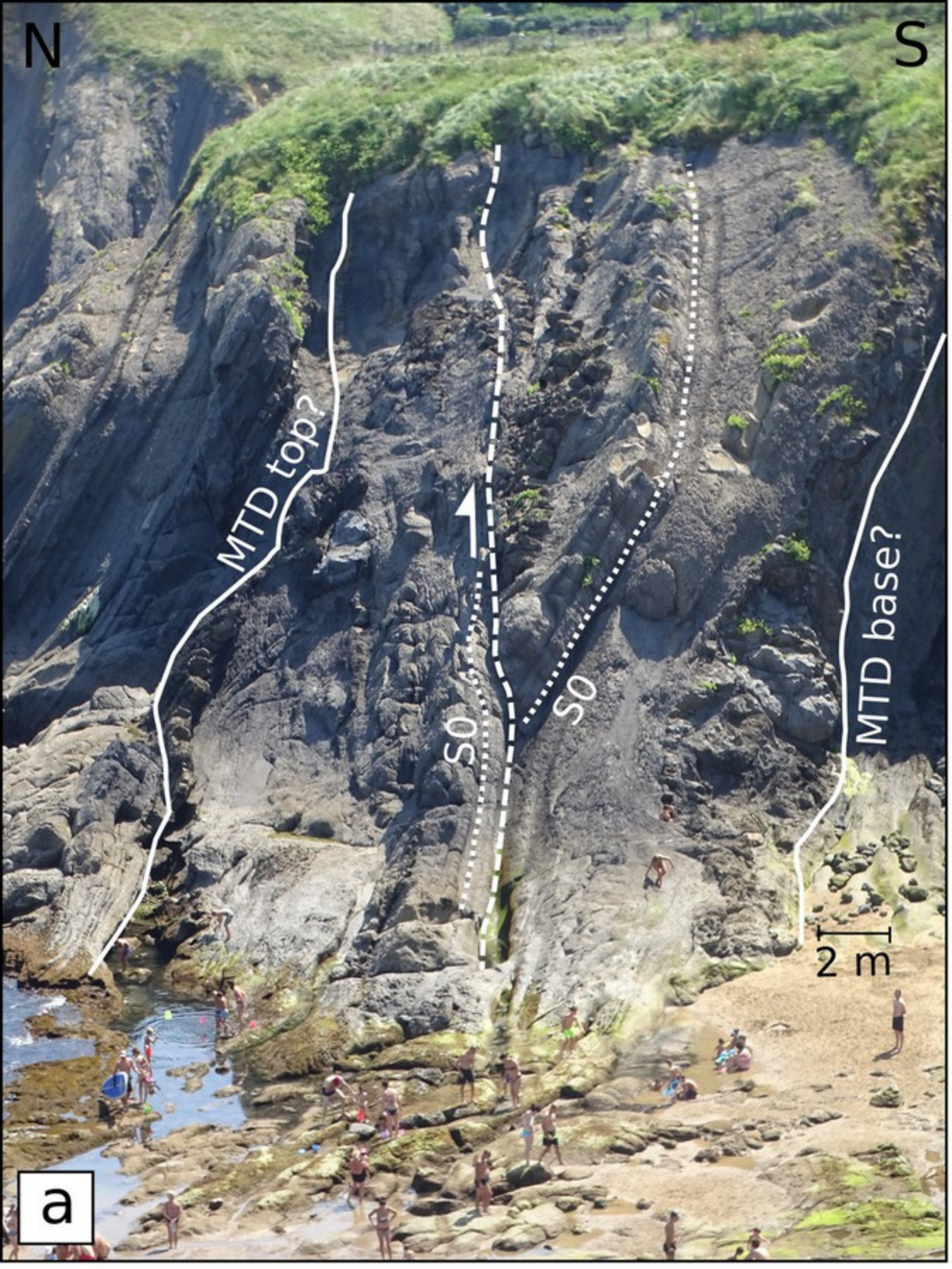
N
S
MTD top?
S0
S0
MTD base?
2 m
a


b


Canon
c

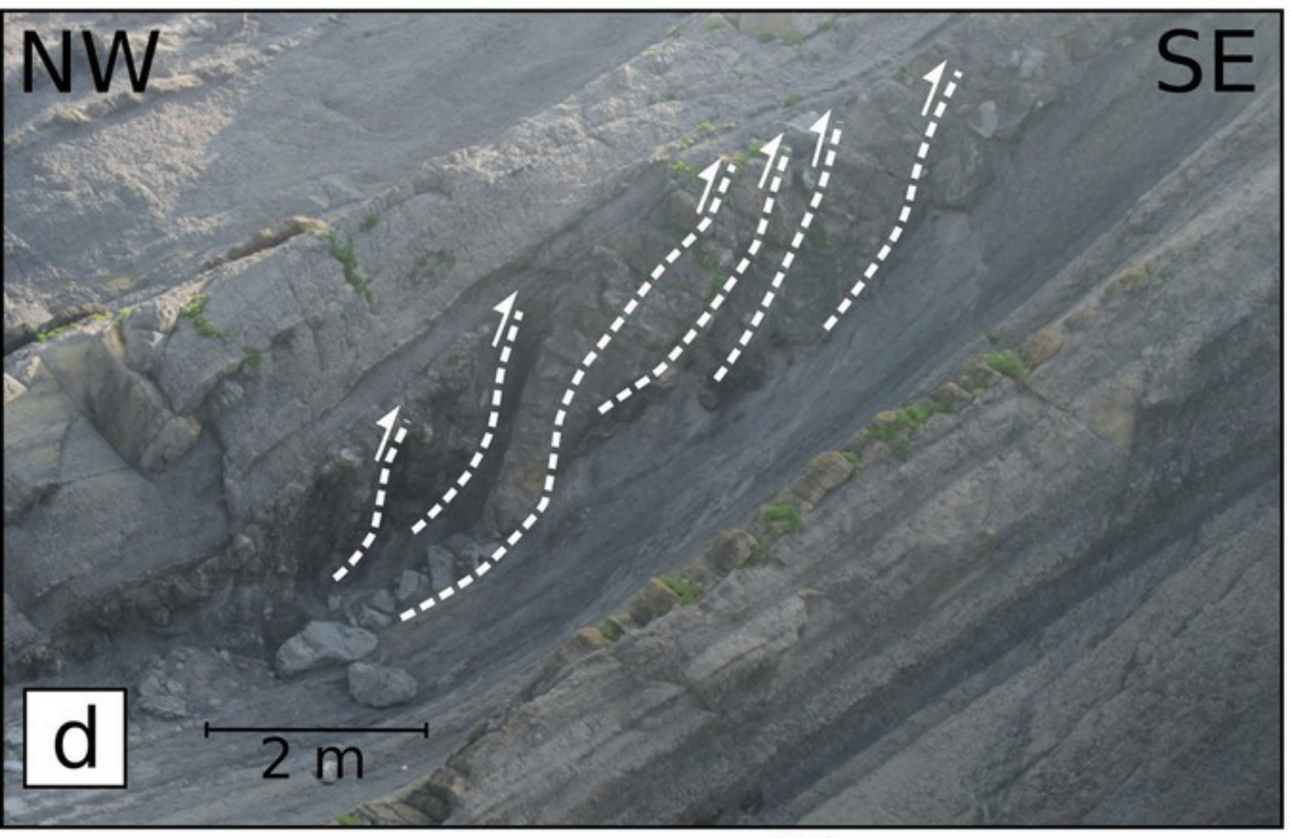
NW
SE
2 m
d


e

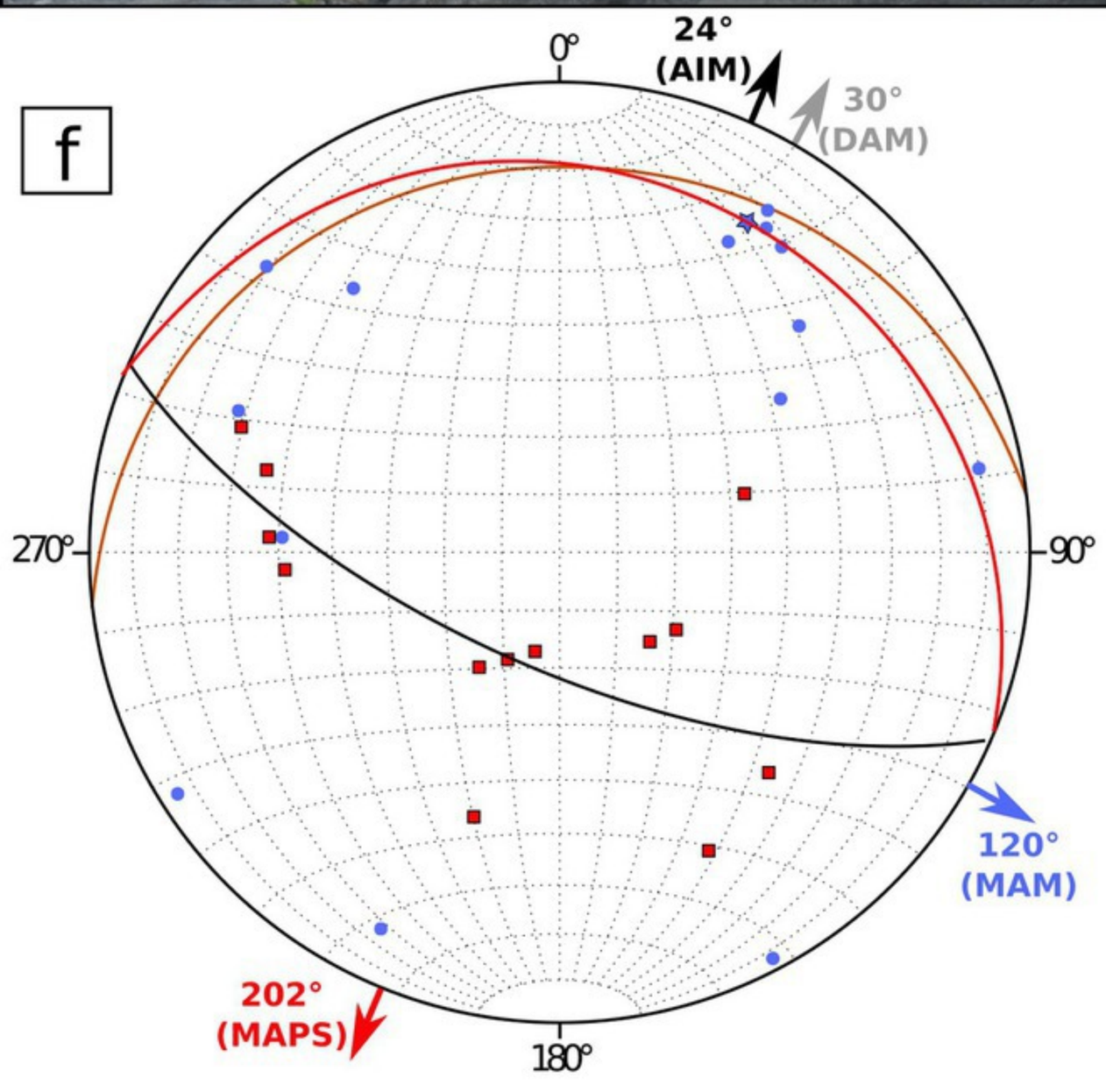
f
0°
24°
(AIM)
30°
(DAM)
270°
90°
120°
(MAM)
202°
(MAPS)
180°

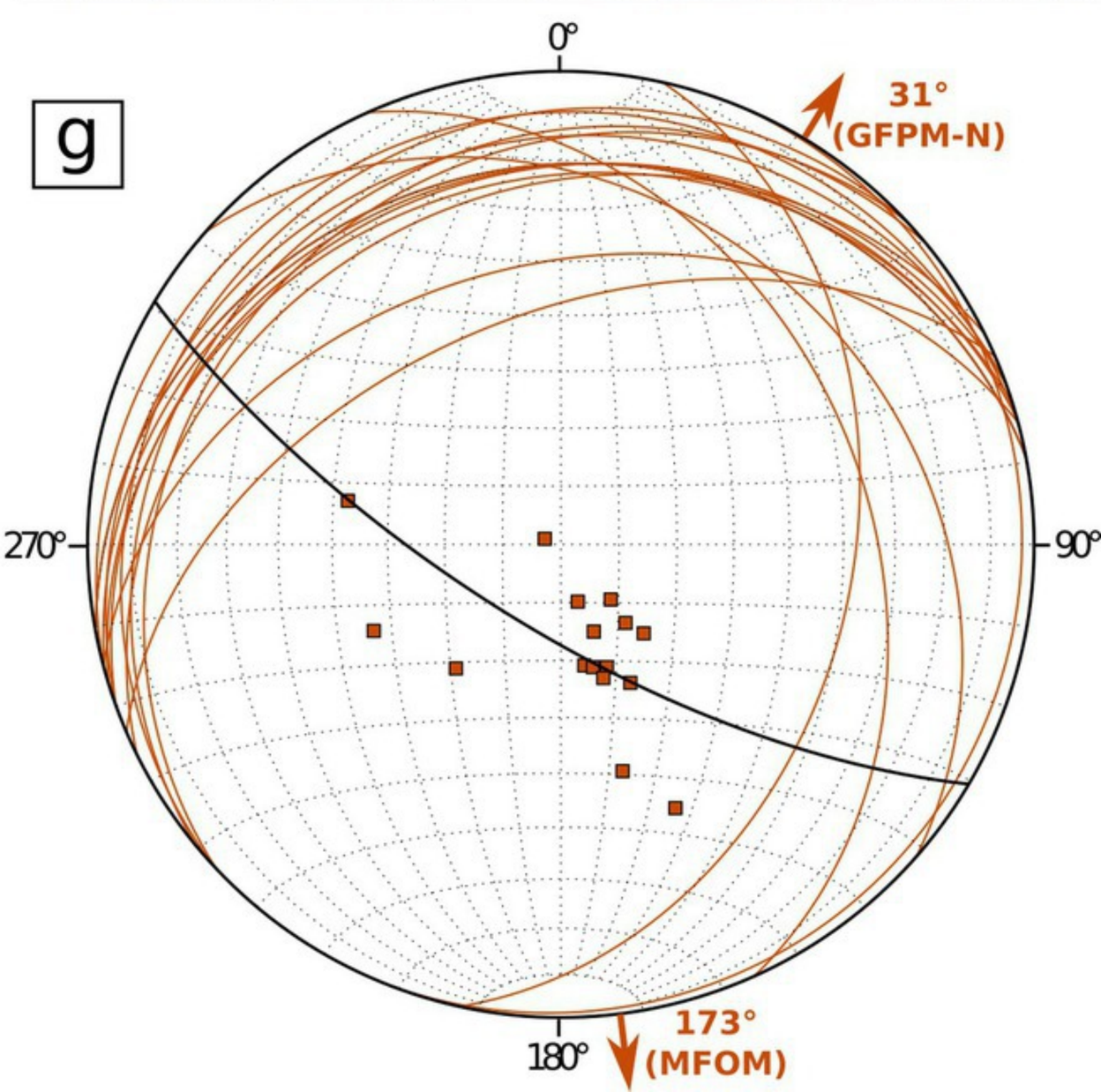
g
0°
31°
(GFPM-N)
270°
90°
180°
173°
(MFOM)

N

S

MTD top

Debrite

Slump

MTD base

1m

a

N

anticlokwise rotation
of the hinge

clokwise rotation
of the hinge

Apparent eastward
transport sense

b

W

E

Apparent eastward
transport sense

c

d

e

348°(DAM)

354°(AIM)

78°
(MAM)

270°

90°

118°
(MAPS)

174°(AIM
corrected)

168°(DAM
corrected)

S
N
Muddy debrite
MTD top
MTD base
c
Beds thinning westward
Slump
2m
a
N
b
S
N
C
Apparent southward transport sense
d
0°
58° (DAM)
63° (AIM)
90°
180°
270°
243° (AIM)
238° (DAM)
147°(MAPS)
148°(MAM)

NE
SW
MTD top
MTD base
1m
a
b
NE
SW
Main apparent
transport sense
Back-thrusts
Truncated layers
b
NE
SW
Apparent southwestward
transport sense
c
d
e
0°
281°
(MAPS)
270°
90°
233°
(MAM)
143°
(DAM)
154°
(AIM)
180°

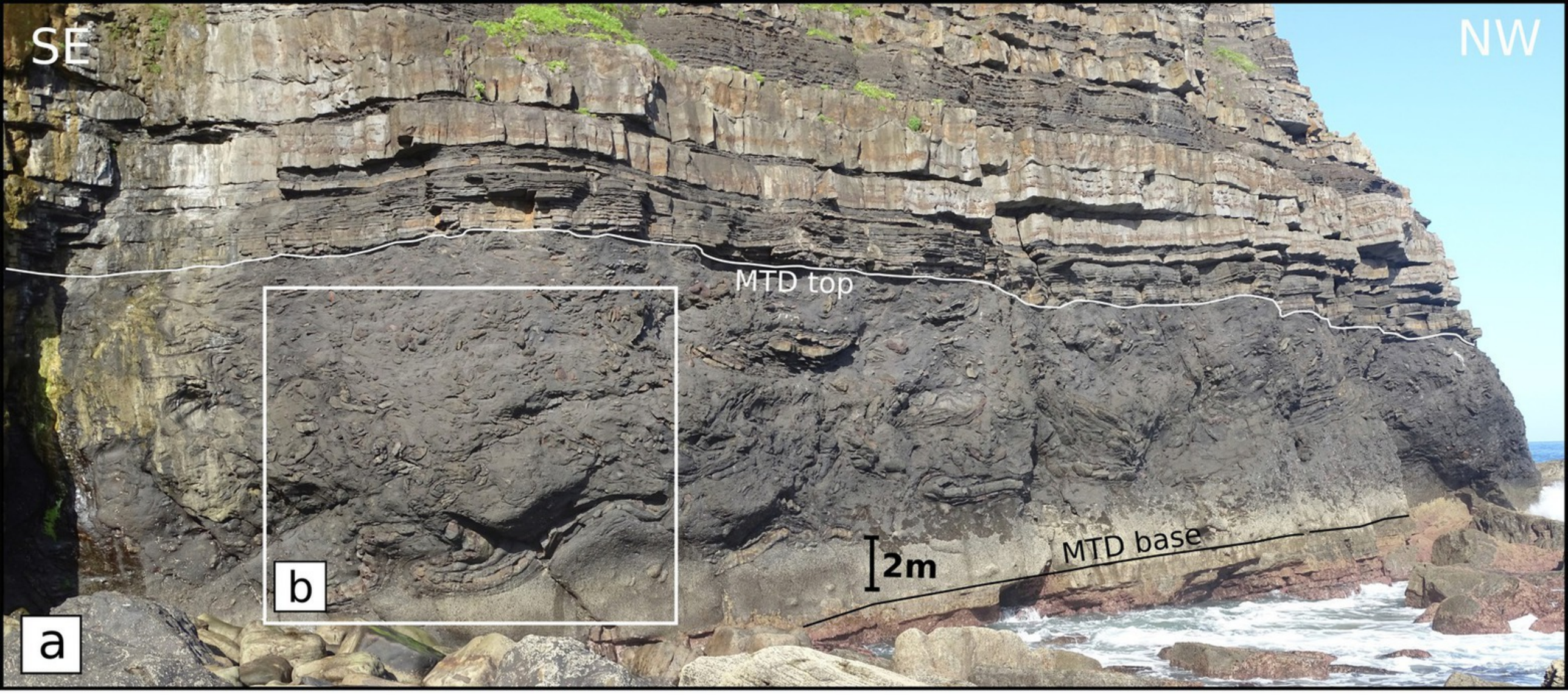
SE
NW
MTD top
MTD base
2m
b
a

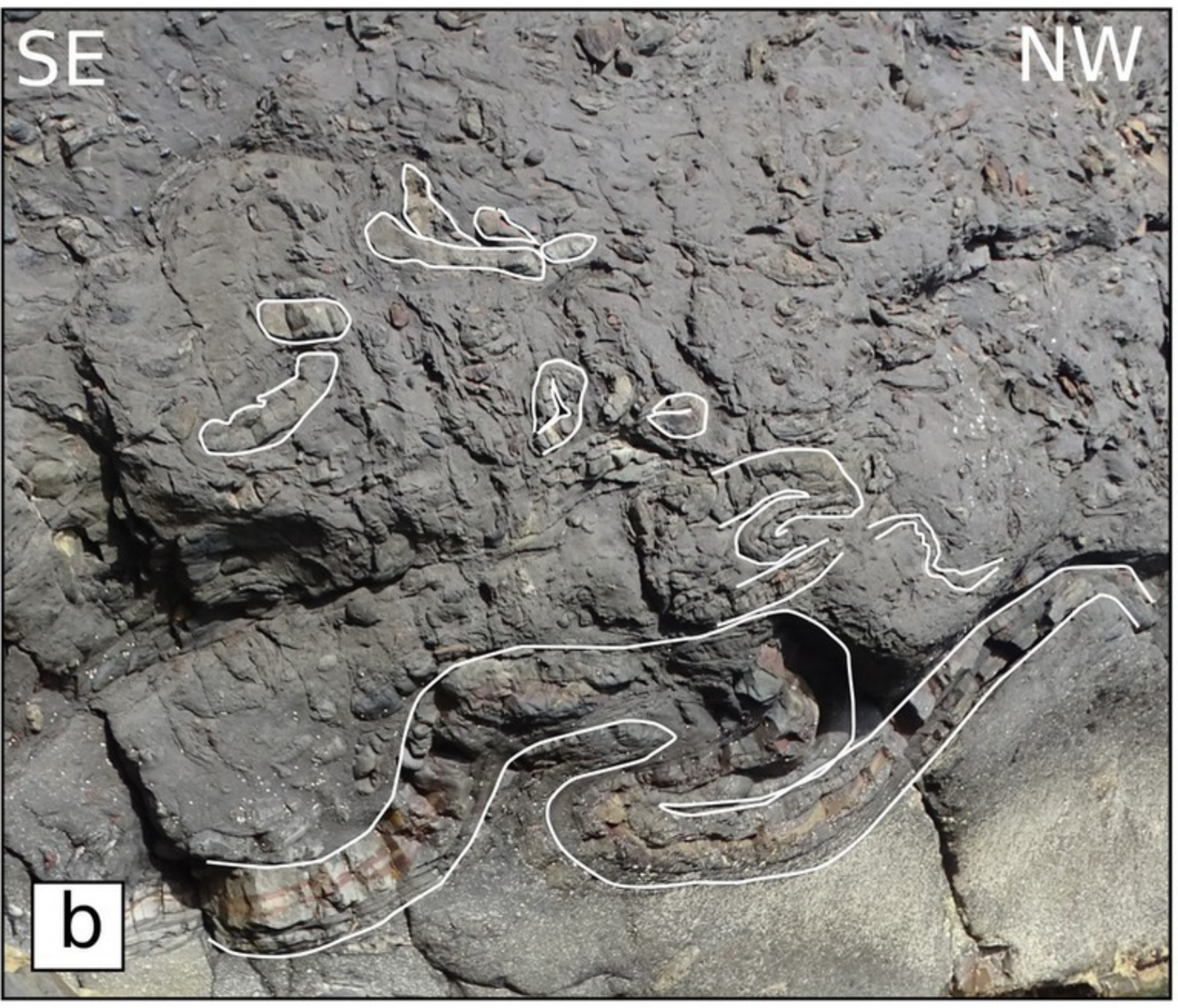
SE
NW
b

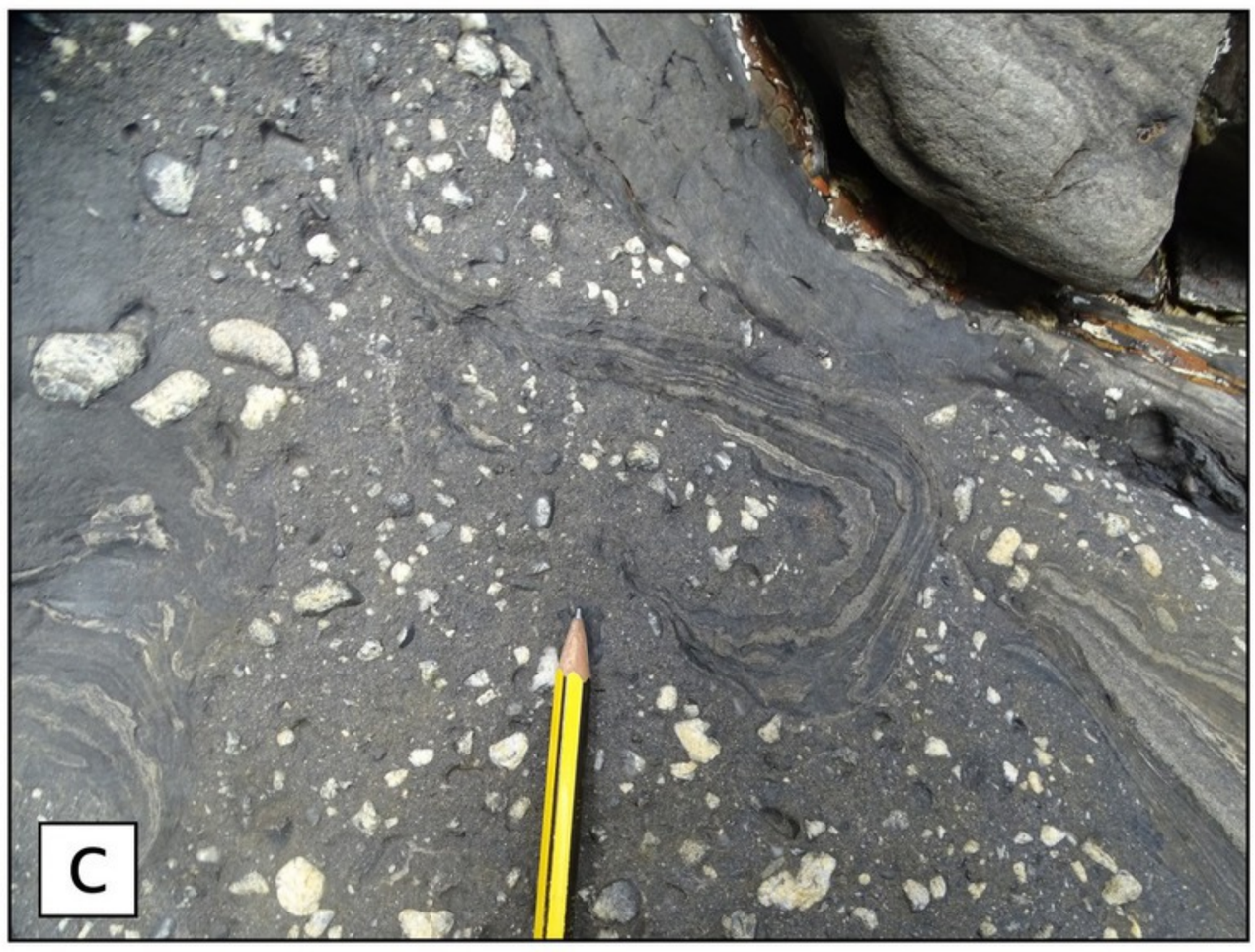
c

d

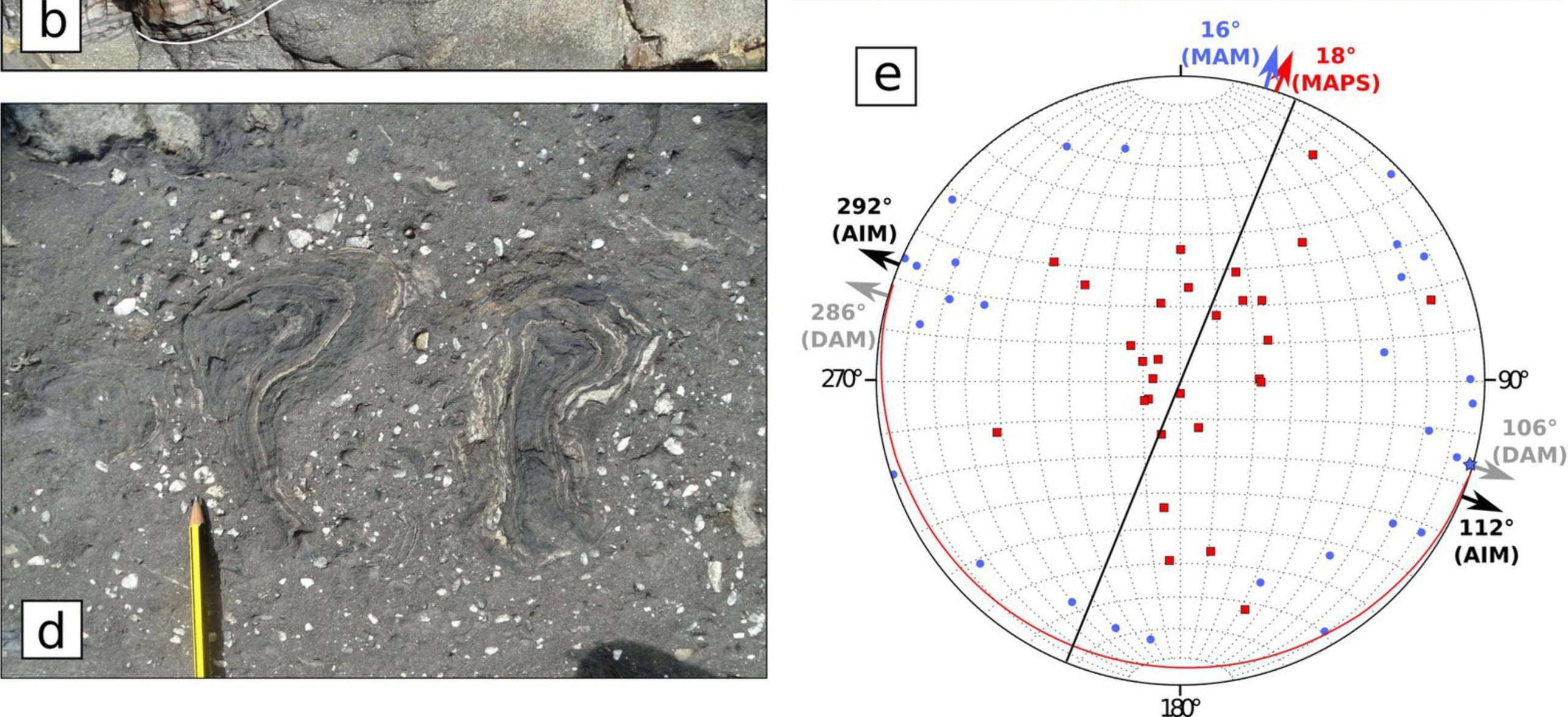
e
16°
(MAM)
18°
(MAPS)
292°
(AIM)
286°
(DAM)
270°
90°
106°
(DAM)
112°
(AIM)
180°

E

W

MTD top

muddy debrite/slump

hinge rotation

MTD base

slump

a

b

E

W

hinge rotation

334°,20°

319°,10°

1m

b

c

d

0°

16° (MAPS)

62° (MAM°

270°

90°

180°

168° (AIM)

152° (DAM)

E

W

MTD top

MTD base

Lava flow

pillow

Eroded layers

2m

a

E

W

MTD top

MTD base

2m

b

E

W

C

d

0°

37°
(MAPS)

81°
(MAM)

270°

90°

176°
(AIM)

171°
(DAM)

E

W

thrusts

downslope area

a

E

upslope area

W

synsedimentary
normal faults

b

c

0°

270°

90°

180°

265°
(MFOM)

E

W

MTD top

Slump

2 m

Debrite

MTD base

d

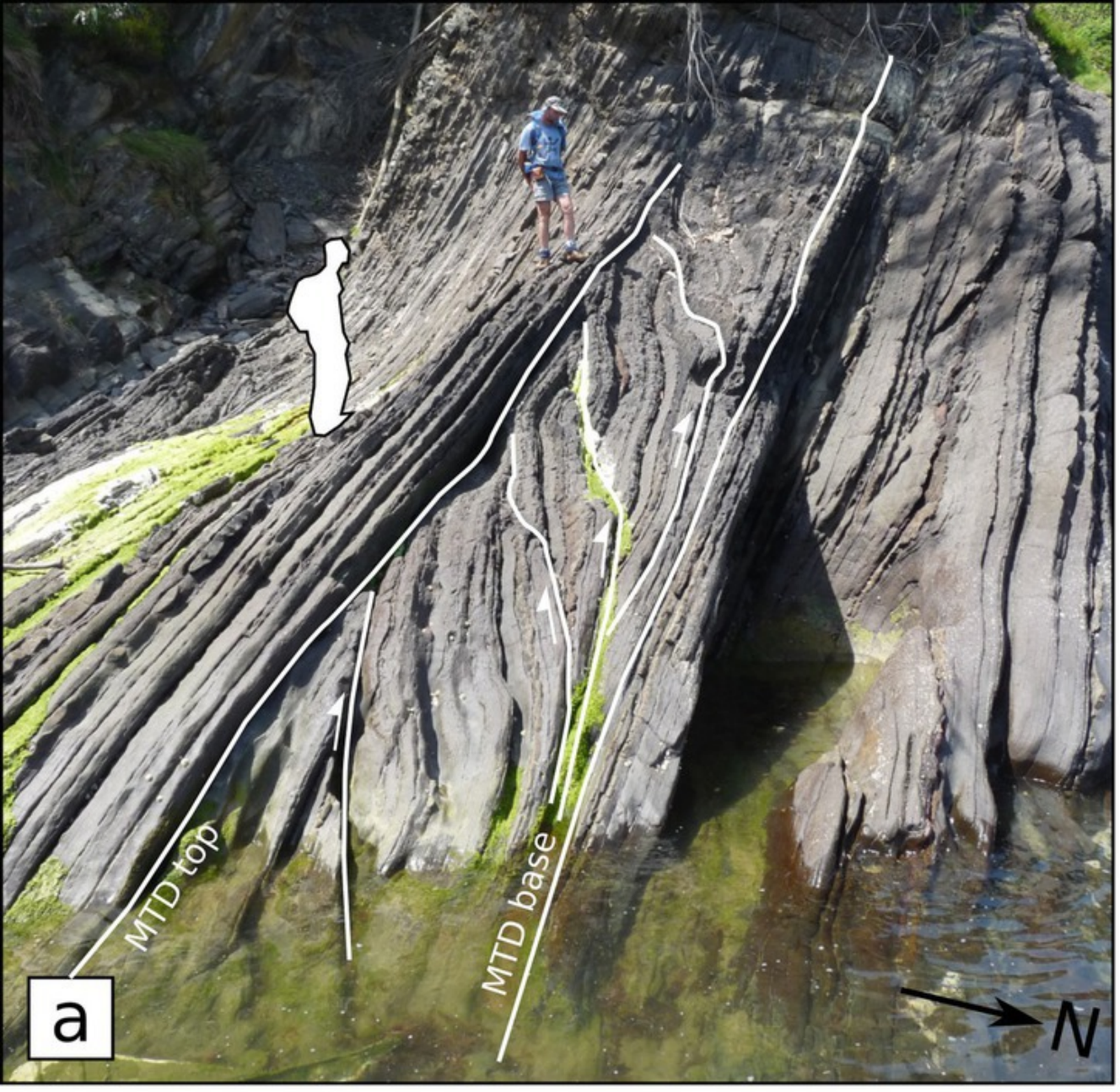
MTD top
MTD base
N
a

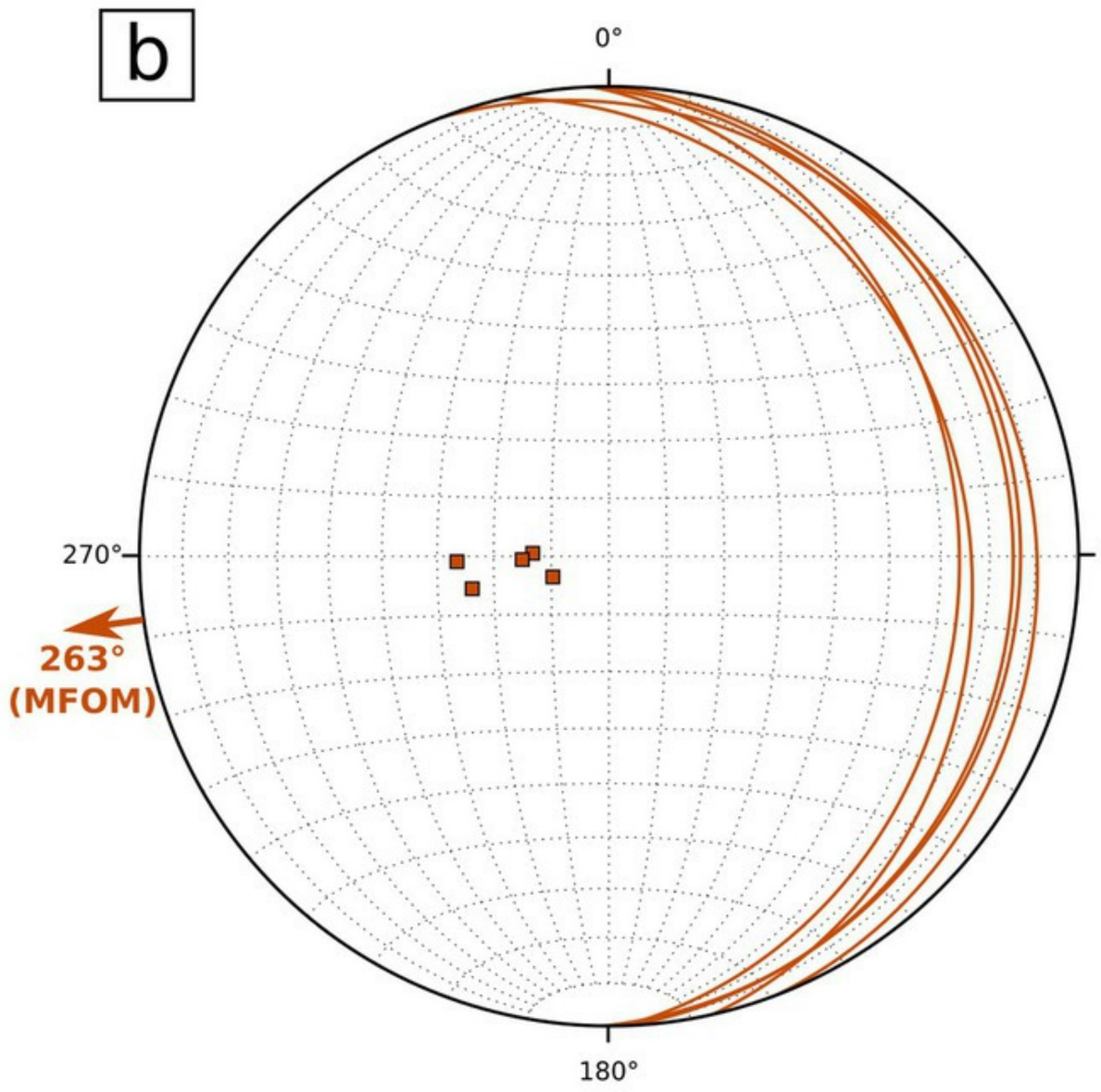
b
0°
270°
90°
263°
(MFOM)
180°


W
E
Detached
slump fold
MTD top
MTD base
c


W
E
Detached
slump fold
MTD top
2 m
d

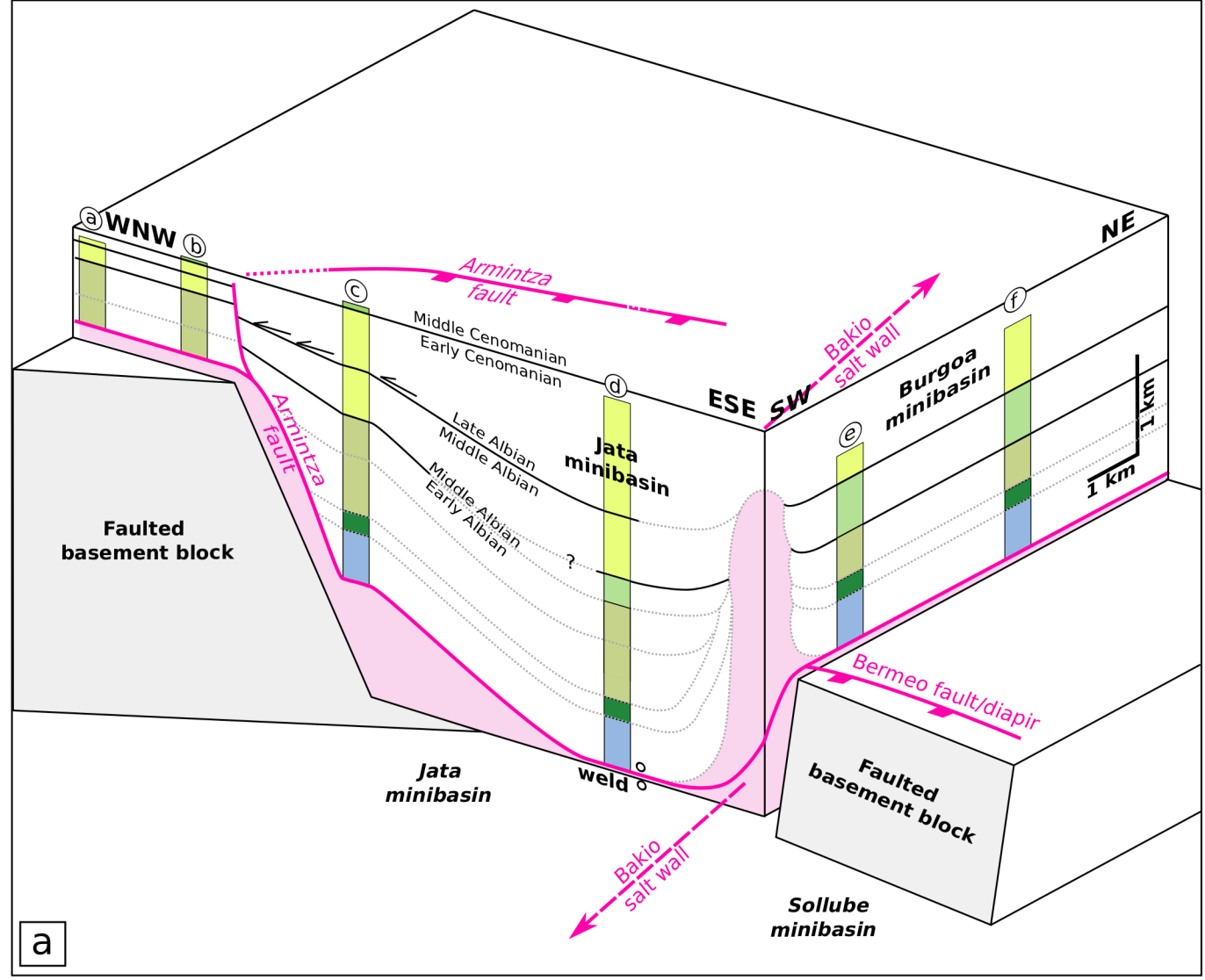

Calcareous Flysch
Black Flysch Group
Bakio breccias Fm. (lower calciclastic part of the Black Flsych Group)
Aptian-Early Albian undifferenciated units
Neocomian
Jurassic
Keuper salt-bearing red clay

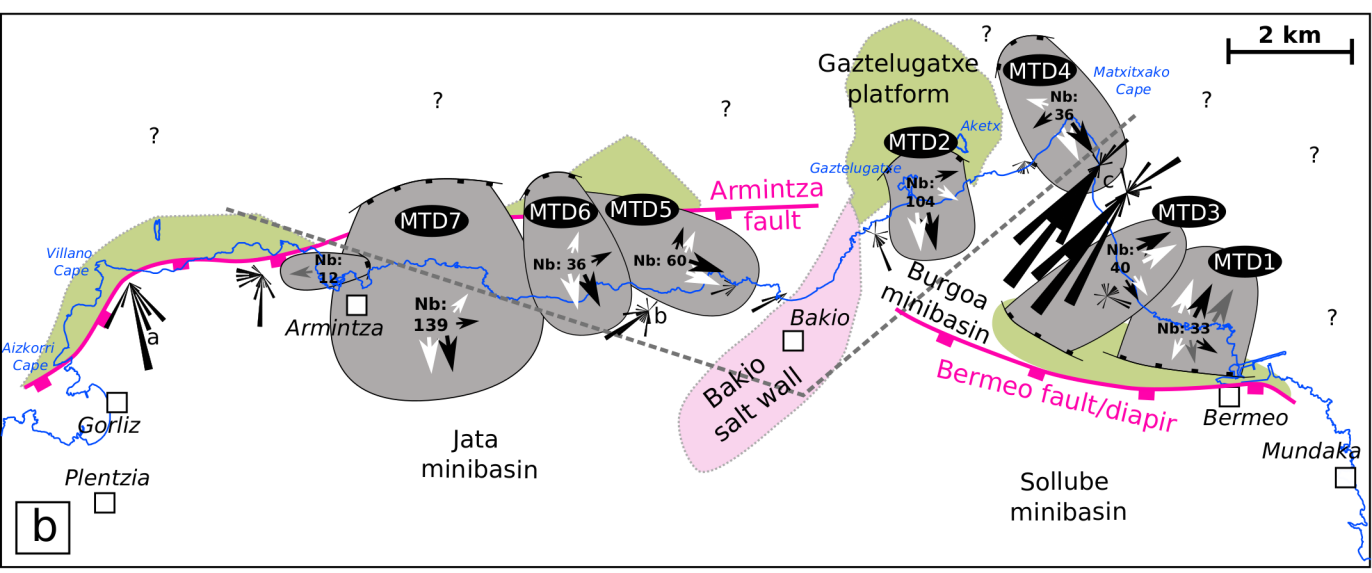

MTD1 — MTD and their possible extension

Nb: 139 — number of structural data used for the transport sense reconstruction (including folds axes, axial planes and faults when present).

transport sense inferred using the AIM

transport sense inferred using the DAM

transport sense inferred using the MAPS

transport sense inferred using the MAM

transport sense inferred using the GFPM

transport sense inferred using the MFOM

Possible Early to Middle Albian carbonate platforms extension

Salt located near the sea floor during the deposition of the Albian

Major subsalt extensional fault inferred by Roca et al., 2020)

Rose diagrams of turbidite palaeoflows

Approximative section used for the figure 14a.

Present-day coastline

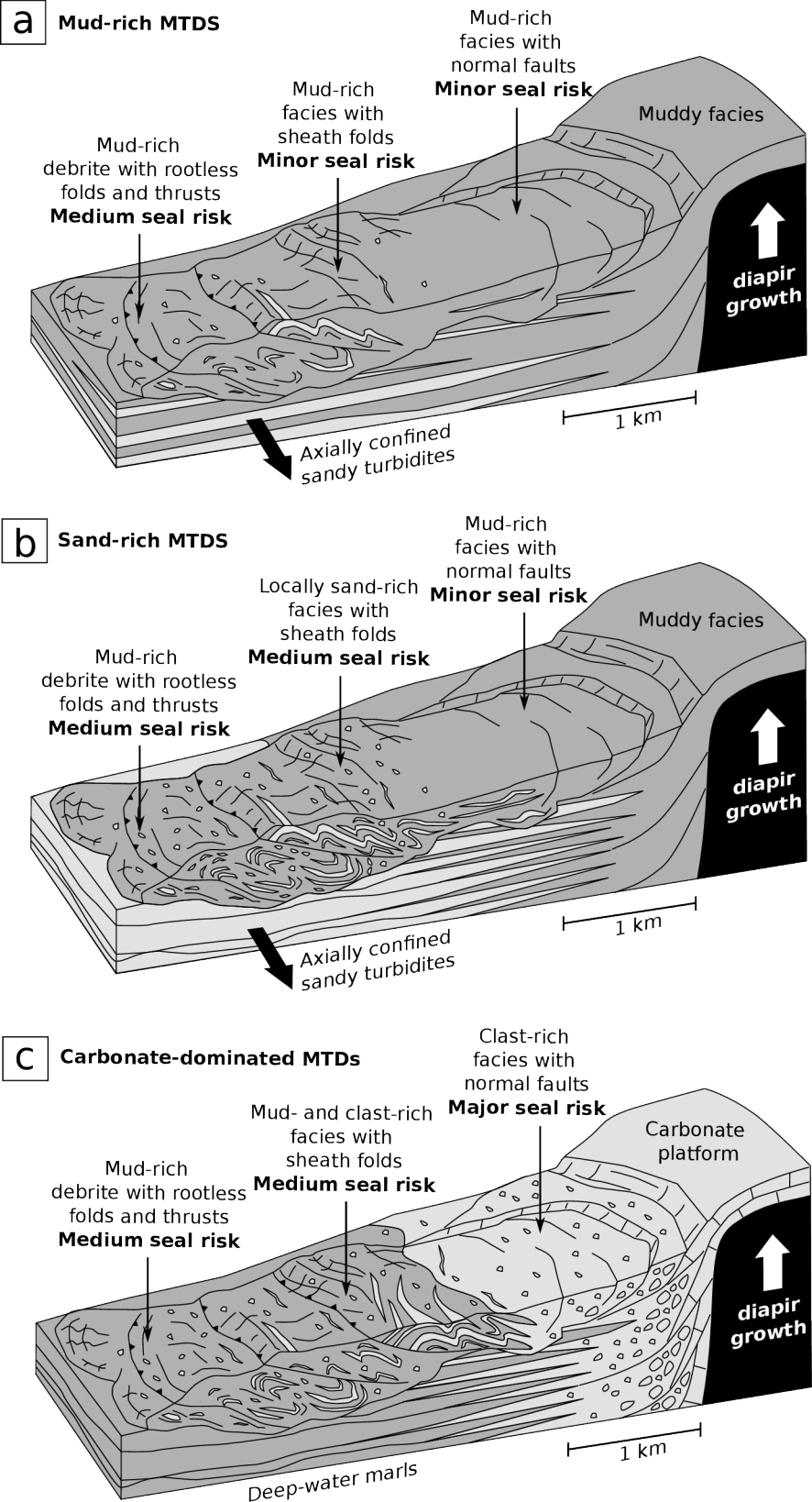
a
Mud-rich MTDS
Mud-rich facies with normal faults
Minor seal risk
Mud-rich facies with sheath folds
Minor seal risk
Muddy facies
Mud-rich debrite with rootless folds and thrusts
Medium seal risk
diapir growth
1 km
Axially confined sandy turbidites
b
Sand-rich MTDS
Mud-rich facies with normal faults
Minor seal risk
Locally sand-rich facies with sheath folds
Medium seal risk
Muddy facies
Mud-rich debrite with rootless folds and thrusts
Medium seal risk
diapir growth
1 km
Axially confined sandy turbidites
c
Carbonate-dominated MTDs
Clast-rich facies with normal faults
Major seal risk
Mud- and clast-rich facies with sheath folds
Medium seal risk
Carbonate platform
Mud-rich debrite with rootless folds and thrusts
Medium seal risk
diapir growth
1 km
Deep-water marls

N° in fig. 4	Unit	Fossils names	Approximate location of the samples	Inferred age of the unit	Authors
1	Castillo limestone Fm.	-Simplorbitolina conulus -Orbitolina (Mesorbitolina) minuta -Hensonina lenticularis	Punta del Castilo / Aizkorri Punta	Early Albian	Robles et al. (1988)
2	Monte Grande Fm.	-Mesorbitolina minuta -Hensonina lenticularis -Orbitolina (Mesorbitolina) texana -Orbitolina (Mesorbitolina) aperta	Punta Motz	Early Albian	Robles et al. (1988)
3	Base of unit 1 of the Black Flsych Group / Punta de Bakio unit	-Mesorbitolina texana -Mesorbitolina aperta -Neorbitolinopsis conulus	Outcrops in the coastline in the western flank of Bakio diapir	Middle Albian	Robles et al. (1988)
4	Bakio breccias Fm.	-Hensonina lenticularis	Outcrops in the coastline in the eatern flank of the Bakio diapir	Middle Albian	Robles et al. (1988)
5	Equivalent of the Bakio breccias Fm.	-Mesorbitolina aperta	Outcrops in the coastline, North of Bermeo	Middle Albian	Robles et al. (1988)
6	Unit 2 of the Black Flysch Group	-Actinoceramus concentricus gryphaeoides, -Desmoceras latidorsatum, -Ticinella -Hedbergella	Outcrops between Punta Motz and the Villano Cape	Late Albian	Agirrezabala (2015)
7	Top of unit 1 of the Black Flysch Group	-Oxytropidoceras cf. Roissyanum	30 m below the lava flow and the MTD7 in the Armintza harbor	Middle Albian	López-Horgue et al. (2009)

	Base of unit 2 of the Black Flysch Group	-Labeceras sp. -Bhimaites sp. -Hamites sp. juv. -Hysteroceras sp. juv. -Protetragonites sp. juv. -Kossmatella oosteri -Puzosia (Anapuzosia) tucuyensis -Puzosia (Anapuzosia) sp. juv. -Kossmatella romana -Tetragonites sp. juv. -Jauberticeras jaubertianum -Desmoceras latidorsatum -Desmoceras sp. juv. -Hypophylloceras moreti -Hypophylloceras subalpinum -Hypohylloceras seresitense -Kossmatella schindewolfi -Kossmatella muhlenbecki -Parasilesites kilianiformis -Hysteroceras varicosum -Hysteroceras binum -Craginites sp. -Mortoniceras (Deiradoceras) exilis -Arestoceras cf. Splendidum -Mortoniceras (Deiradoceras) bispinosum -Puzosia mayoriana -Mortoniceras (M.) crassinodatum -Anisoceras armatum -Mortoniceras (M.) sp. indet. cf. gr. Rostratum	Interval including the deposits 15 m below and 120m above the lava flow and the MTD7 in the Armintza harbor	Late Albian	López-Horgue et al. (2009)

		-Actinoceramus concentricus			
8	Base of unit 2 of the Black Flysch Group	-Mesorbitolina minuta -Mesorbitolina aperta -Neorbitolinopsis conulus	In a calciclastic turbidite, NE of Bermeo	Late Albian	Robles et al. (1988)
9	Calcareous Flysch	-Rotalipora appenninica -Rotalipora cushmani	Not mentioned	Middle Cenomanian to Santonian	Feuillé (1967)

Table 1: summary of the biostratigraphic data used in this paper including the the approximate location of the samples, the inferred age and the references where the data are described. The numbers refer to those used in figure 4.